OBSERVATIONS OF CHAIN AGGREGATES IN FLORIDA CIRRUS CLOUD ANVILS ON 3 AUGUST 2019 DURING CAPEEX19

by

Christian Michael Nairy
Bachelor of Science, State University of New York at Oswego, 2019

A Thesis

Submitted to the Graduate Facility

of the

University of North Dakota

in partial fulfillment of the requirements

for the degree of
Master of Science

Grand Forks, North Dakota

May 2022

This thesis, submitted by Christian Nairy in partial fulfillment of the requirements for the Degree of Master of Science from the University of North Dakota, has been read by the Faculty Advisory Committee under whom the work has been done and is hereby approved.

David Delene, Committee Chair

Michael Poellot, Committee Member

Jerome Schmidt, Committee Member

Paul Harasti, Committee Member

This thesis is being submitted by the appointed advisory committee as having met all of the requirements of the School of Graduate Studies at the University of North Dakota and is hereby approved.

Dr. Chris Nelson, Dean
School of Graduate Studies

DATE

PERMISSION

Title	Observations of Chain Aggregates in Florida Cirrus Cloud Anvils on 3 August 2019 during CapeEx19
Department	Atmospheric Sciences
Degree	Master of Science

In presenting this thesis in partial fulfillment of the requirements for a graduate degree from the University of North Dakota, I agree that the library of this University shall make it freely available for inspection. I further agree that permission for extensive copying for scholarly purposes may be granted by the professor who supervised my thesis work or, in her absence, by the Chairperson of the department or the dean of the School of Graduate Studies. It is understood that any copying or publication or other use of this thesis or part thereof for financial gain shall not be allowed without my written permission. It is also understood that due recognition shall be given to me and to the University of North Dakota in any scholarly use which may be made of any material in my thesis.

Christian M. Nairy
July 26, 2022

TABLE OF CONTENTS

LIST OF FIGURES

LIST OF TABLES

ACKNOWLEDGEMENTS

The Author would like to thank David Delene, Michael Poellot, Jerome Schmidt, and Paul Harasti, who reviewed the content and provided supplementing information and guidance. The Author would also like to thank Andrew Detwiler, Emma Järvinen, Martin Schnaiter, Jeffrey Stith, Hugh Christian, and Nicholas Gapp for their contributed wisdom in this work.

ABSTRACT

Elongated chain-like aggregates have been observed in cirrus cloud anvils produced by electrified thunderstorms. Cloud chamber experiments have also been able to generate chain aggregates while applying strong electric fields (> 60 kV m^{-1}) to environments with ice crystal concentrations between 3.0 x 10^6 – 4.0 x 10^6 m^{-3} and over a range of temperatures. While it is believed that electric fields are important for chain aggregate formation, exactly where and how the chain aggregation process occurs with thunderstorm is not well understood, which inhibits inclusion in cloud models. Not having chain aggregates in models causes inaccuracies to cloud radiative transfer properties. Furthermore, chain aggregates are important to consider for supersonic flight.

To better understand the chain aggregation process, the North Dakota Citation II Research Aircraft sampled convection-induced, cirrus cloud anvils during the 3 August 2019 CapeEx19 field project flight. The aircraft flight's in-situ observations are analyzed to determine the degree that chain aggregation is occurring within cirrus cloud anvils. While chain aggregation is likely occurring in multiple locations; the in-situ, cirrus anvil observations indicate that the highest concentrations of chain aggregates are close to the storm core and the chain aggregate concentrations decrease away from the storm core. The observed chain aggregates contain individual crystal elements that grow under different temperature regimes and approximately 90 percent of the chain aggregates lack the presence of any rimed ice. Electric field observations indicate stronger electric fields closer to the storm core (on the order of 10^1 kV m^{-1}), which suggests that the chain aggregates observed near the storm core may have formed within the storm core, likely above regions of high concentrations of supercooled liquid water. However, the relative chain aggregate concentration with respect to non-chain aggregates ($RCAC_{N\text{-}C}$) increases away

from the storm core (up to a certain distance), which supports the hypothesis that the chain aggregation process is occurring in the cirrus anvil region. However, further away from the storm core the electric fields are low which inhibits the idea that chain aggregation is continuing in the cirrus anvil region.

Analysis of additional flights that transect through the convective core would be useful to see if higher concentrations of chain aggregates (rimed and un-rimed) are observed. Analysis of all the CapeEx19 research flights would be useful to determine the variability of chain aggregates away from the convective cores. Moreover, to help understand the chain aggregation process in the cirrus anvil region, additional cloud chamber experiments would be beneficial to test if chain aggregation can occur using electric fields < 60 kV m^{-1} at temperatures colder than -30 °C.

CHAPTER I

INTRODUCTION

Elongated chain-like aggregates (Figure 1) have been observed in cirrus anvils produced by electrified thunderstorms. These types of chain-like crystals have also been observed in laboratory experiments where aggregation occurred with high electric fields in cloud chambers (see Figure 4 – 5 in Saunders and Wahab, 1975). While electric fields enhance chain-like aggregation, details of the process occurring in storms, and even the location, are not well understood. Hence, atmospheric models do not incorporate the chain aggregation process. Since these chain aggregates contain many individual ice particles, they have more mass and different optical properties than individual ice crystals. Not accounting for this difference causes inaccuracies of the radiative transfer properties of cirrus anvils (Liou 1973). Furthermore, the absence of these relatively large particles in atmospheric cloud models have important implications when determining supersonic projectile trajectories that intersect cirrus cloud anvils. This is due to hypersonic collisions with the relatively large, chain-like crystals, which can cause cratering on the vehicle's nose cone, altering the vehicle's aerodynamics (Lin and Thyson 1977; Barnes Jr. 1982; Meng and Ludema 1995; and information provided in Appendix A).

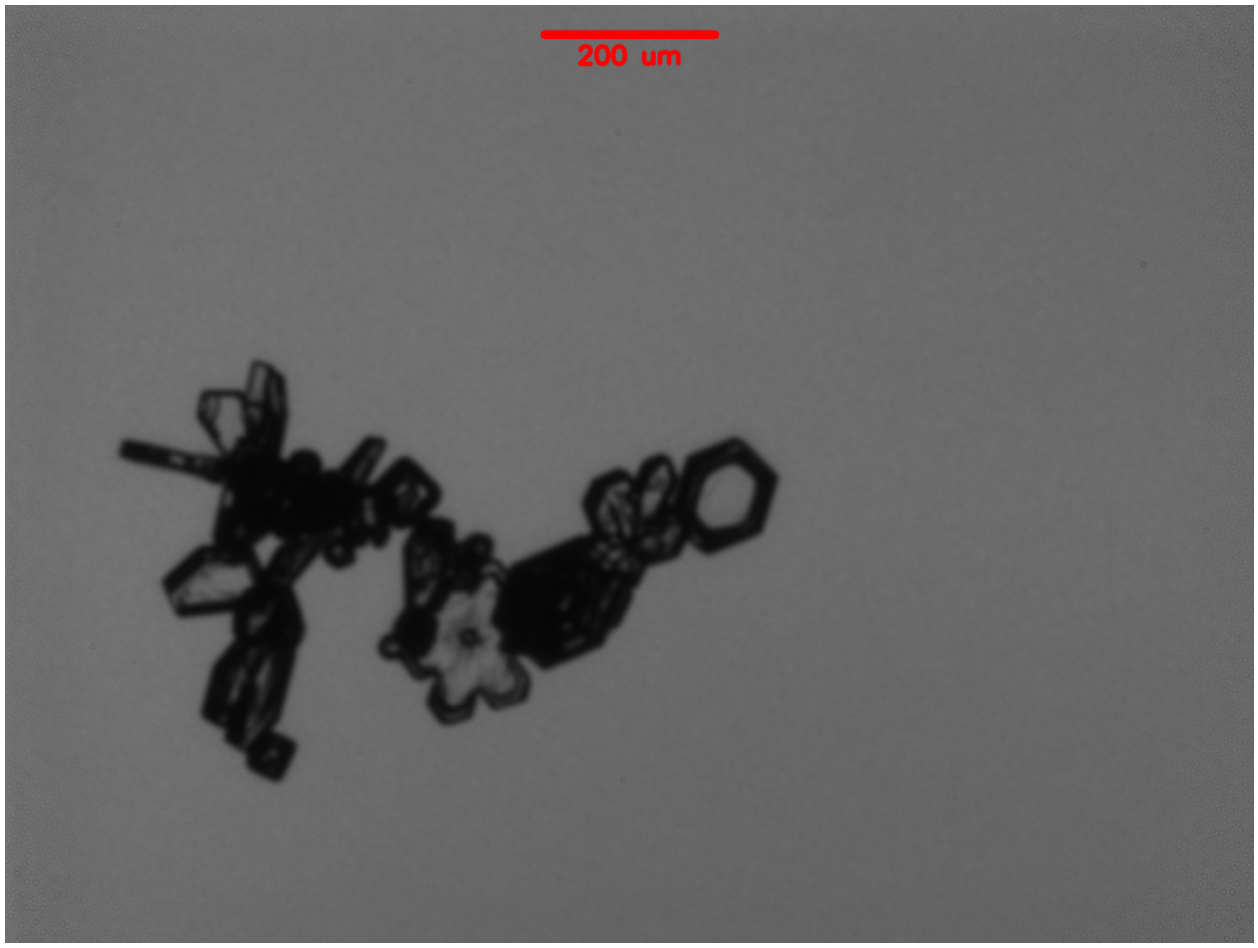

Figure 1. Image of a chain aggregate taken by the Particle Habit Imaging and Polar Scattering (PHIPS) probe on 3 August 2019 at 16:05:34 UTC.

The objective is to utilize newly acquired, state-of-the-art, in-situ observations made in the convection-induced, cirrus anvil regions of Florida thunderstorms to determine the degree that chain aggregation is occurring. The objective is performed by characterizing and analyzing observed chain aggregates with respect to distance from Florida thunderstorm cores from in-situ microphysical probes via aircraft and comparing to in-situ electric field observations and radar data from the CapeEx19 data set. With the results, comparisons are made to the thresholds depicted in previous cloud chamber experiments to conclude if chain aggregation is occurring in convection-induced, cirrus anvil regions of Florida thunderstorms. The end results will provide

insight into the overall cloud processes responsible for creating chain-like crystals, which enable improvement of cloud models.

Cloud Chamber Experiments

Scientists have conducted several experiments using cloud chambers to test how electric fields influence aggregation. Latham and Saunders (1964) performed experiments that tested the collection efficiencies and interactions of ice crystals on an ice sphere with different applied electric fields. The collection efficiencies increased with increasing electric field strengths up to several hundred volts per centimeter. It is important to note that the term collection efficiency is essentially the product of the adhesion and collision efficiencies which is similar to the aggregation efficiency. The term collection efficiency was based upon the experimental design, though, the term aggregation efficiency is used herein for clarity.

Utilizing a similar experimental design, Latham and Saunders (1970) investigated the aggregation efficiency for approximately 5 μm size ice crystals on a 0.2 cm ice sphere over a temperature range of -7 °C to -27 °C. There was an increase in the aggregation efficiencies with increasing electric fields (500, 1000, and 1500 V cm^{-1}) that was independent of temperature. On the other hand, while using electric field strengths greater than 1500 V cm^{-1}, ice crystal growth rates decreased due to the ejection of clusters of ice crystals from the aggregate. This was most likely due to the influence of intense electric forces. In subsidiary experiments, an appreciable amount of aggregation was observed in temperatures down to -37 °C with and without electric fields.

Crowther and Saunders (1973) cloud chamber experiments found that freely falling ice crystals, in realistic atmospheric electric fields, could result in a 100% aggregation after just a few seconds. However, aggregate fragmentation could occur due to mechanical stresses from the high

electric field strengths acting on the induced charges (similar to results in Latham and Saunders, 1970). For example, with an applied electric field of 75 kV m^{-1} at -19 °C, 60% of the crystals and fragments were involved in aggregation with an average of three crystals per observed aggregate after 40 seconds of growth. During the same growth period and same temperature but with an applied electric field strength of 150 kV m^{-1}, 95% were involved in aggregation and had an average of 10 crystals per observed aggregate. These aggregates were not observed in clumps or clusters, but as elongated chain-like aggregates typically oriented in a straight line with resulting sizes around 300 μm. It was concluded that when ice crystals fall in an electric field the aggregation and fragmentation processes are caused by the interaction of both the induced and total charges on the ice crystals when separated by short distances. Despite the observations, the experiments only accounted for a horizontal electric field. For electrified clouds in the real atmosphere this may not be the case, which is reflected in the various different theories and uncertainties revolving around the cloud electrification process. Moreover, the experiments used higher ice crystal concentrations than what occur in the natural environment.

Saunders and Wahab (1975) performed a cloud chamber study using an improved replication technique to test aggregation using various horizontal electric field strengths, more realistic ice crystal sizes (between 30 – 50 μm), and concentrations (between 1.0 x 10^6 – 5 x 10^6 m^{-3}). It was recognized that aggregation occurred in the absent of an electric field; therefore, a "relative aggregation efficiency" was defined. While using a constant applied electric field of 200 kV m^{-1}, ice crystal concentrations between 3.0 x 10^6 – 4.0 x 10^6 m^{-3}, and approximate ice crystal sizes around 50 μm, the apex (maximum) of the relative aggregation efficiency was 33% at around -8 °C and decreased to approximately 10% at around -15 °C. Furthermore, it was observed that the minimum threshold for the electric field strength to have an impact on aggregation was 60 kV m^{-1},

which increased the number of collisions and optimized the adhesion efficiencies in order for ice crystals to remain in contact with one another. Chain aggregates generated in both the -8 °C (prisms) and -12 °C (hexagonal plates) temperature regimes comprised between 2 and 10 crystals in a quasi-linear formation. Due to the ability of the electric field to modify the aggregation ability of crystals as a function of temperature, it was suggested that the sensitivity of crystal types (based on temperature) may play an important role. It is important to note that ice crystal concentrations used in the experiments were much higher than what is typically observed in the atmosphere. Moreover, ice crystals have a longer residence time inside a cloud (in the atmosphere) than inside the cloud chamber. While in a cloud, ice particles have more time to interact with other particles as well as with the electric fields. Also, the electric fields are not always horizontal in thunderstorms and the electric field strengths are not always constant. The inability to accurately represent the electric field in cloud chamber experiments hinder the precise representation of how the electric fields effect the aggregation process.

Previous Aircraft Observations

Chain aggregates similar to those observed in the various cloud chamber experiments have been observed during experiments in both maritime and continental convection-induced cirrus anvils by in-situ airborne observations via aircraft (Table 1 [Stith *et al.* 2002; Lawson *et al.* 2003; Stith *et al.* 2004; Whiteaway *et al.* 2004; Connolly *et al.* 2005; Garret *et al.* 2005; Dye and Willett (2007); Gayet *et al.* (2012) Stith *et al.* 2014; Dye and Bansemer (2017); Um *et al.* 2018; Schmidt *et al.* 2019]. Connolly *et al.* (2005) analyzed microphysical data from previous aircraft experiments (where chain aggregates were observed) from continental, continental-tropical, and tropical-maritime convection and compared the results to previous cloud chamber experimental results. Most of the chain aggregates were observed in cirrus anvils produced from intense thunderstorms

that climatologically tended to contain continental aerosol concentrations and sometimes with influences from maritime airmasses. The chain aggregates observed were comprised of small plate-like polycrystals and only accounted for a small percentage of the total particle population in the cirrus anvils. Many of these chains were found in cold temperature regions between -43 and -50 °C and the highest concentrations of the chain aggregates were found near the cirrus anvil bases. Conversely, chain aggregates of capped columns and plate-like ice crystals were observed in much warmer regions of continental convection over Florida at around -8° C (Stith *et al.* 2004). Aside from continental convection, very few chain aggregates were observed in tropical convection-induced cirrus anvils.

Table 1. List of previously performed field campaigns that observed chain aggregates via aircraft. Described are the regions, airmass type, altitude, temperature, and crystal types (elements) of where the chain aggregates are found (characterized). Citations: (a) - Stith *et al.* (2002), Stith *et al.* (2004), Connolly *et al.* (2005); (b) - Lawson *et al.* (2003), Whiteaway *et al.* (2004), Connolly *et al.* (2005); (c) - Gayet *et al.* (2012); (d) - Lawson *et al.* (2003), Connolly *et al.* (2005); (e) - Stith *et al*. (2014); (f) - Um *et al*. (2018); (g) - Lawson *et al*. (2003) & Stith *et al.* (2004), Garret *et al.* (2005); (h) - Dye & Willett (2007), Dye *et al*. (2007), Dye & Bansemer (2019); (i) - Schmidt *et al*. (2019).

	Region	**Airmass**	**Altitude**	**Temperature**	**Crystal Type(s)**
a.	Amazon Rain Forest (LBA) - Near Updraft Region and Cirrus Anvil	Tropical	N/A	-8°C to -43°C	Capped columns and plate-like crystals with some riming present.
b.	Darwin, Australia - Cirrus Anvil	Continental	~ 12 to 14 km	-40°C to -50°C	Plate-like ice crystals
c.	Western Europe - Cirrus Anvil	Continental	~ 8.2 to 11.1 km	-58°C	Plate-like ice crystals, irregular ice crystals, and frozen droplets
d.	Eastern Colorado, USA - Cirrus Anvil	Continental	~7.5 to 12.5 km	-47°C	N/A
e.	Eastern Colorado, USA - Cirrus Anvil	Continental	~ 6.8 to 13 km	-13°C to -60°C	Frozen droplets and plate-like ice crystals
f.	Eastern Colorado, USA - Cirrus Anvil	Continental	~ 12 km	-56.5°C to -60°C	Frozen Droplets

g.	Florida, USA - Cirrus Anvil	Continental	~ 8.6 to 11.2 km	-25°C and -65°C	Capped columns and plate-like crystals
h.	Florida, USA - Cirrus Anvil	Continental	9.3 km	-32°C	Plate-like ice crystals protruding from more compact aggregates.
i.	Florida, USA - Cirrus Anvil	Continental	~ 11.2 - 11.3 km	-43°C to -44°C	Plate-like ice crystals

The lack of observed chain aggregates and other aggregates in maritime-tropical, convection-induced, cirrus anvils was most likely due to the insufficient electrical activity within the storms (Christian *et al.* 2003). Although no electric field measurements were made during any of the experiments examined by Connolly *et al.* (2005), it was concluded that electric fields may play a significant role in ice crystal aggregation. In addition, it is possible that chain aggregates originated in the upper mixed-phased updraft region. However, the lack of riming on most chain aggregates provides evidence that these aggregates may originate in colder regions of the thunderstorms (colder than -37 °C).

During July 2002, the Cirrus Regional Study of Tropical Anvils and Cirrus Layers – Florida Area Cirrus Experiment (CRYSTAL–FACE) utilized The North Dakota Citation Research Aircraft and the NASA WB-57F to sample continental (with a maritime influence), convection – induced, cirrus anvils at altitudes between 8.6 and 14.3 km and temperatures of -25 and -70°C respectively (Garret *et al.* 2005). Images from the Cloud Particle Imager (CPI) probe on the North Dakota Citation II Research Aircraft showed chain aggregates comprised of plate-like ice crystals as well as other irregular ice crystals at altitudes between 8.6 and 11.2 km and temperatures of -25 and -45 °C respectively (images from CRYSTAL-FACE also shown in Connolly et al. 2005). These chain aggregates are similar to what was observed while sampling continental, convection-induced, cirrus anvils via aircraft in western Europe, though, many of the chains observed there appeared to be comprised of frozen droplets (Gayet *et al.* 2012). It was suggested that chain

aggregates comprised of frozen droplets are formed when strong updrafts lift supercooled liquid water particles where they then freeze by homogenous freezing and then aggregate under the influence of strong electric fields. Similarly, chain aggregates of frozen droplets were observed during aircraft sampling of continental, convection-induced, cirrus anvils in eastern Colorado (Lawson *et al.* 2003; Connolly *et al.* 2005; Stith *et al.* 2014; Um *et al.* 2018) where only a small percentage of the chain aggregates contained plate-like ice crystal elements.

Airborne measurements were also made in June 2000 and May/June 2001 within cirrus anvil and stratiform cloud regions during the Airborne Field Mill II experiment (ABFM II) near Kennedy Space Center (Dye *et al.* 2007). Airborne measurements were made by utilizing the North Dakota Citation Research Aircraft which was fitted with 6 rotating-vane electric field mills and various microphysical probes. At altitudes ranging from 7-10 km, temperatures from -40 to -30 °C, and reflectivity values between 10-20 dBZ, electric fields mostly between 20 to 40 kV m^{-1} (sometimes > 50 kV m^{-1}) were observed during several passes through cirrus anvil cloud regions. Within these high electric field regions, they observed elongated chain-like aggregates and compact aggregates both containing protruding branches containing plate-like ice crystals with and without rimed ice (Dye and Willett, 2007). However, no noticeable differences in the concentration of chain aggregates between flight passes in high and low electric field strengths were observed. It was concluded that aggregation could be enhanced in electric fields < 50 kV m^{-1}. Further analysis of the images taken by the CPI probe showed that the shapes/orientations of the chain aggregates suggest that electric fields had acted to enhance aggregation (Dye and Bansemer, 2019). It was concluded that aggregation may be enhanced in weaker electric fields than otherwise suggested/demonstrated in previously performed laboratory cloud chamber experiments.

During the 2015 Cape Experiment (CAPE2015) the North Dakota Citation II Research Aircraft sampled continental (with a maritime influence), convection-induced, cirrus anvils near Cape Canaveral, Florida (Schmidt *et al.* 2019). Utilizing the 2D-S stereo probe, chain-like aggregates comprised of different habits in general seemed to be apparent at altitudes between 11.2 and 11.3 km and temperatures of -43 and -44 °C respectively. Some of the chains appear to have plate-like elements, although due to the poor resolution and image quality of the 2D-S, there was difficulty visualizing each chain aggregate element and discerning the exact crystal habits.

There are clear discrepancies between the cloud chamber experiments and the aircraft observations regarding the chain aggregation process. In the aircraft observations, chain aggregates were observed in colder, upper-level regions of thunderstorms and their induced cirrus anvil cloud(s). In the cloud chamber experiments, the temperatures for which the chain aggregation is occurring suggests that the aggregation process is occurring near the vicinity of the mixed-phased region where there is a mixture of ice, liquid water, and supercooled liquid water present. If this is the case, rimed ice should be present on many of the chain aggregates; however, there was a lack of rimed ice on the chain aggregates in the aircraft observations. Moreover, the cloud chamber experiments determined that the electric field threshold strength conducive for chain aggregation to occur is 60 kV m^{-1}. Conversely, aircraft observations in the cirrus anvil regions where chain aggregates were observed measured electric fields less than 60 kV m^{-1}. It is possible that chain aggregation does not need to meet this electric field threshold in the cirrus anvil regions (as depicted by Dye and Willet, 2007; Dye and Bansemer, 2019) if the relative aggregation efficiency is a function of electric field strength and temperature (Saunders and Wahab, 1975). Thus, more in-situ data are required to confirm this hypothesis.

The contradictions and uncertainties regarding where and how chain aggregates may form remain unsolved, which inhibits the inclusion of this aggregation process in atmospheric cloud models. To aid in furthering our understanding of the chain aggregation process and to investigate if chain aggregation is occurring in continental (with a maritime influence), convection-induced cirrus anvil regions, more field experiments with improved sampling methods and instrumentation must be performed.

CHAPTER II

DATA SETS AND INSTRUMENTATION

In succession of the CAPE2015 field campaign, the Cape Experiment in 2019 (CapeEx19) utilizes The North Dakota Citation II Research Aircraft with newly implemented, state-of-the-art instruments, and obtained in-situ observations in Florida, convection-induced, cirrus anvils. The CapeEx19 field campaign is conducted from late July to early August near Cape Canaveral, Florida. For the first research flight on 3 August 2019 the North Dakota Citation II Research Aircraft took off from the Space Coast Regional Airport in Titusville, Florida at 14:24 UTC. The aircraft landed back at the Space Coast Regional Airport at 17:25 UTC for a total flight duration of about three hours. The aircraft samples convection-induced, cirrus cloud anvils from 15:51:15 to 16:46:00 UTC for a sampling duration of approximately one hour. The objective is to investigate the presence of chain aggregates/chain aggregation to improve cirrus cloud modeling as well as improving radar interpretation using an array of observations both remote-sensed and in-situ.

During the 3 August 2019 flight during the CapeEx19 field campaign, in-situ measurements of convection-induced, cirrus anvil clouds, are obtained by The North Dakota Citation II Research Aircraft (Figure 2). The North Dakota Citation II Research Aircraft is equipped with instruments that measure environmental conditions such as temperature, dewpoint temperature, pressure, and wind velocity (Delene *et al.* 2019a). Additionally, The North Dakota Citation II Research Aircraft is equipped with an onboard camera and instruments that measure altitude and GPS location. The North Dakota Citation II Research Aircraft has been utilized in many field projects using different instrumentation configurations in order to collect cloud microphysical observations (see Jenson *et al.* 2004 and Skofronick-Jackson *et al.* 2015 for other aircraft configuration examples). The North

Dakota Citation II Research Aircraft instrument configuration is adjusted for the CapeEx19 field campaign by implementing new state-of-the-art instruments in order to overcome some of the shortcomings from previous field projects and gain a better understanding of the chain aggregation process. New instruments implemented on the North Dakota Citation II Research Aircraft includes the PHIPS probe and 6 rotating-vane electric field mills. The in-situ instruments utilized in this study are referenced in this section.

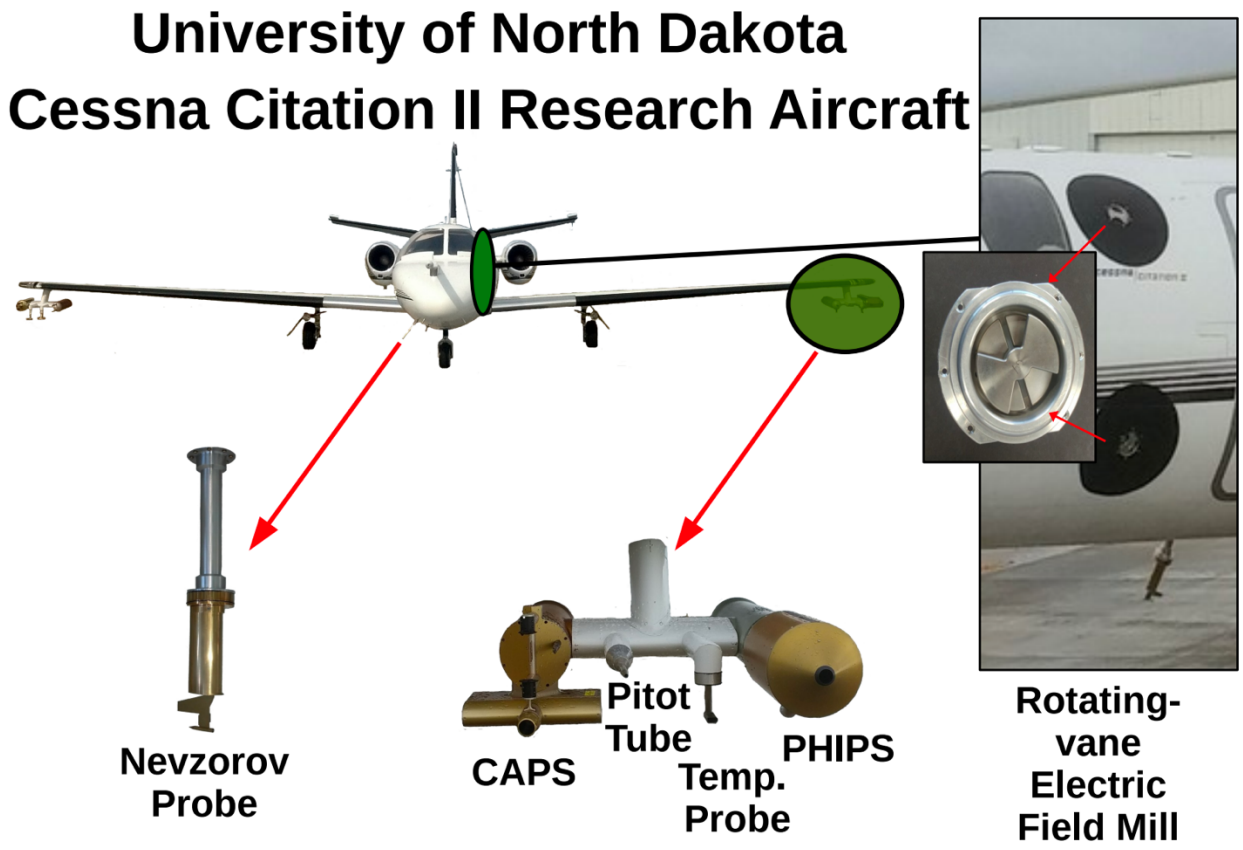

Figure 2. Image showing the North Dakota Citation Research Aircraft with an enlarged view of the port-side wing-tip pylon. The pylon contains the Particle Habit Imaging and Polar Scattering (PHIPS) probe for particle images and their microphysical properties, a temperature probe ("Temp. Probe") for measuring the ambient temperature, a Pitot Tube for measuring air speed, and the Cloud, Aerosol, and Precipitation (CAPS) probe. The CAPS probe measures cloud particle, cloud droplet, and aerosol concentrations. A side view of the aircraft is provided showing two of the six total rotating-vane electric field mills which measures the ambient electric field. Overlaid is a zoomed in image showing one of the rotating-vane electric field mills in further detail. The Nevzorov Water Content Probe ("Nevzorov Probe") measures total water content (TWC) and is located on the belly of the aircraft; an enlarged image of the probe is provided. New instruments implemented on the Citation Research Aircraft for the CapeEx19 field campaign are the PHIPS and the 6 rotating-vane electric field mills.

The PHIPS probe is a recently developed airborne optical sensor to provide clarity into the link between the microphysical characteristics of individual ice particles and their respected angular light scattering function (Schnaiter *et al.* 2018). Characterized as a hybrid between the airborne polar nephelometer (PN) and the Cloud Particle Imager (CPI) probe, the PHIPS probe is able to combine and correlate optical and microphysical measurements of individual cloud particles (Abdelmonem *et al.* 2016). In the optical head of the PHIPS probe, there are two optical components that allow for the combined measurements. The first optical component is the polar nephelometer which measures the angular scattered light from the individual cloud particles as they pass through a polarized collimated continuous wave laser. The second is a stereo-microscopic imaging system comprised of two camera-telescope assemblies (CTAs) and a pulsing illumination laser. The CTAs allow for stereographic images of the same cloud particle from two viewing angles separated by an angular distance of 120 °. The stereo-microscopic imaging system also has magnification capabilities with optical magnifications from low (1.4 ×) to high (9.0 ×) with an optical resolution range from 7.2 to 2.35 μm, respectively. At 4 × magnification, particle sizes can range from 3 μm to 4.7 mm. The individual cloud particle is then projected on two charge-coupled devices (CCDs). The maximum sampling rate of the PHIPS is 25 Hz.

The ability to obtain high-resolution particle images from two different angles while also obtaining microphysical measurements of those particles eliminate some of the uncertainties brought by other probes like the CPI. The CPI is able obtain high-definition particle images, though, due to the probe only having one camera, particle classification can be difficult because of particles not always being in an optimal orientation for a clear image. Since previously observed chain aggregates are typically elongated and have multiple particle elements joined together, the odds of a particle being in an optimal orientation to observe every single individual particle element and being able to discern all the particle habits in one image is slim. Moreover, the CPI does not obtain microphysical measurements of the sampled particles. While the PHIPS probe does obtain measurements of the size (using a fast-circle method) and scattering properties of the imaged particles, the PHIPS probe has some trouble measuring the size of the particles that are not completely in the frame from either camera. Nevertheless, because of the improved particle imaging and measuring capabilities of the PHIPS deems this instrument vital for improved interpretations and visualizations of chain aggregates and is a significant upgrade to the CPI.

The North Dakota Citation II Research Aircraft also implements 6 rotating-vane electric field mills to measure the ambient electric field while sampling convection-induced, cirrus anvils on the 3 August 2019 flight during the CapeEx19 field campaign. The rotating-vane electric field mills implemented on the aircraft are provided by the University of Alabama in Huntsville (UAH). The aircraft mounted electric field mills are used to measure the electric field strength and orientation within the cirrus cloud anvils.

All six of the electric field mills are positioned on fuselage ports around the perimeter of the aircraft. Four of the electric field mills are positioned around the body of the aircraft adjacent to the doors/entrances and cockpit windows, while the remaining two electric field mills are

positioned on the tail of the aircraft. Each rotating-vane electric field mill contains an electric field modulator consisting of stationary sensing electrodes and a rotating shield electrode (Bateman *et al.* 2007). While in operation, the open gaps of the rotating shield electrode periodically expose the sensing plates to the electric field outside of the aircraft. The electric field values are then calculated as a result of the time-varying charge induced on the sensing plates by the ambient electric field. Several previously performed airborne experiments have tested the rotating-vane electric field mills and has proven, due to careful engineering, that the electric field mills are rugged enough to perform beyond spec in dynamic weather conditions (Bateman *et al.* 2007).

Calibration of the electric field mills for the flights during the CapeEx19 field campaign are performed using methods described in Mach and Koshak (2007) where The North Dakota Citation II Research Aircraft flew in fair weather (cloudless sky); which provides a uniform, fair weather electric field. Once calibrated, the rotating-vane electric field mills are able to deduce the ambient electric field into vector components (E_x, E_y, E_z) on sampling flights using techniques described in Bateman *et al.* (2007). The reference coordinate system used on the North Dakota Citation II Research Aircraft is the x-axis (E_x) along the fuselage of the aircraft (roll axis), where E_x is positive in the direction of flight; the y-axis (E_y) being along the wings of the aircraft (pitch axis), where E_y is positive out the left wing (port); and the z-axis (E_z) being perpendicular to the fuselage and the wings of the aircraft, where during level flight, E_z is positive up. Determining the individual electric field components from matrix coefficients is based on the approach used in Mach and Koshak (2007).

Knowing from previous experiments that electric fields play a significant role in the chain aggregation process, in-situ electric field data from the regions where chain aggregates are observed is critical in order for further insight into where chain aggregation is occurring. From

previously performed airborne experiments where chain aggregates were observed, the lack of electric field measurements hindered opportunities for further understanding regarding the chain aggregation process. Due to only one field experiment that obtained electric field data and particle images of chain aggregates (Dye *et al.* 2007), more datasets are needed in order for improving our understanding of the chain aggregation process. Increasing the population of in-situ electric field datasets in cloud regions where chain aggregates are observed opens up the opportunity for more in-depth comparisons to cloud chamber experiments; where in the cloud chamber experiments, electric field strength thresholds in order for chain aggregation to occur were defined.

The Sky Phys Tech Inc. hot-wire Nevzorov Water Content Probe (hereafter referred to as the Nevzorov) is deployed on the North Dakota Citation II Research Aircraft and measures both total and liquid water content. The Nevzorov is able to obtain the cloud water content using two separate wires and calculates the direct relationship between the rate of evaporative cooling on the heated surfaces and the total power necessary to maintain a constant temperature (Korolev *et al.* 1998). The total water content (TWC) is obtained by using a 60 ° concave cone ("TWC collector") that is heated to a constant temperature of 125 °C. Another heated wire measures the liquid water content (LWC). The sensitivity threshold of the Nevzorov is 0.003 g m^{-3} and the instrument's measurement range of TWC and LWC is between 0.003 – 3.0 g m^{-3}. The Nevzorov's TWC sensor has a sampling area of approximately 8 mm.

The Droplet Measurement Technologies, LLC (DMT) Cloud Aerosol and Precipitation Spectrometer with Depolarization (CAPS) is deployed on the North Dakota Citation II Research Aircraft. The CAPS is a "multi-probe" that measures cloud and aerosol concentrations and records cloud particle images by utilizing a suite of three instruments. The CAPS instruments include a Cloud Imaging Probe (CIP), the Cloud and Aerosol Spectrometer (CAS), and the Hotwire Liquid

Water Content Sensor (Baumgardner, 2001). The CIP is an optical array probe that provides shadow images of cloud particles with a particle size range of 12.5 μm – 1.55 mm (resolution of 25 μm) with a sample area of 10 cm x 1.55 mm. The maximum sampling rate of the CIP is 0.05 Hz. Processing of particle data obtained by the CIP to obtain a size distribution is performed using the System for Optical Array Probe Data Analysis Version 2 (SODA2) software package (Bansemer 2013).

Data from the Nevzorov and the CIP is recorded by the Science Engineering Associates (SEA) data acquisition system (Model M300) in a single binary file. To extract the data, the Airborne Data Processing and Analysis software (ADPAA) is used (Delene 2011). All software that is used for the data analysis in this research is openly available upon request and is referenced herein to allow for reproducibility of the presented work.

Along with the airborne observations from the North Dakota Citation II Research Aircraft, the Melbourne, Florida National Weather Service (NWS) Next-Generation Radar (NEXRAD) WSR-88D (KMLB) S-band radar obtains reflectivity (dBZ) measurements. In addition, the Cloud and Precipitation Radar with Discrete Hydrometeor Detection (CPR-HD) is utilized during the CapeEx19 field campaign and is located north of the Kennedy Space Center/Cape Canaveral Air Force Station. The CPR-HD is a C-band, dual-polarization, Doppler radar and is owned and operated by the United States Navy. The CPR-HD is able to track The North Dakota Citation II Research Aircraft while scanning above and below the aircraft within the range windows. The scanning capabilities of the CPR-HD allows for concurrent radar and aircraft in-situ observations. For more information regarding the CPR-HD see Gapp 2019; Schmidt *et al*. 2019.

To display the radar data from the KMLB radar, the Lidar Radar Open Software Environment software package (LROSE) developed by the Earth Observing Laboratory at the National Center

for Atmospheric Research (NCAR/EOL) and Colorado State University is utilized (LROSE 2021). This software allows for ingesting WSR-88D radar data files which are converted to Meteorological Data Volume (MDV) format. MDV file format allows for storing two- and three-dimensional gridded data for a single time which allows access to Constant Altitude Plan Position Indictor (CAPPI) radar displays (NCAR 2021a). The Rview graphical user interface (GUI) displays the MDV files and also ingests American Standard Code for Information Interchange (ASCII). This allows for combining CAPPI radar displays with aircraft flight-tracks which is useful in seeing the path of the aircraft and what the typical reflectivity values were during sampling.

Within the LROSE package, the TITAN application (LROSE-TITAN) allows for thunderstorm identification, tracking, analysis, and nowcasting (NCAR 2021b). The TITAN processes can then be displayed in the Rview GUI concurrently with the radar and aircraft flight-track data. For the purposes of this research the TITAN thunderstorm identification and tracking is used. A 35 dBZ threshold is used to identify and track individual thunderstorms. The reflectivity centroid is computed by TITAN for the thunderstorm in which the aircraft samples from for each individual radar timestep. From this, at each radar timestep, calculations are made for exactly how far away the aircraft is from the center part of the thunderstorm (core). An investigation into the microphysical characteristics of the chain aggregates with respect from the storm core (reflectivity centroid) is performed. However, since the TITAN storm tracking information only provides one coordinate dataset of the storm's reflectivity centroid per radar volume scan, where each KMLB radar volume scan takes approximately 5 minutes, some uncertainties arise when it comes to concluding how far the aircraft was from the storm core reflectivity centroid due to the course temporal resolution of the KMLB radar. Despite the uncertainty, the calculation of the distance

from the aircraft to the storm core reflectivity centroid is useful when analyzing and characterizing the PHIPS images as well as other in-situ microphysical datasets.

Lightning data of the sampled storms is available from the U.S. National Lightning Detection Network (NLDN, owned and operated by the Vaisala Thunderstorm Unit, Tucson, Arizona; Cummins *et al.* 1998). The NLDN consists of 106 stations covering CONUS with each station separated by a typical range of 300 and 350 km. The sensors that make up the network use a combination of time-of-arrival (TOA) and magnetic direction finding (MDF) techniques to report both cloud-to-cloud/intracloud (CC/IC) and cloud-to-ground (CG) lightning strokes and their respected peak currents. (more about TOA and MDF techniques and calculations of peak current see Cummins *et al.* 1998). The range in which these sensors are separated by are strategic for triangulation of the lightning stroke(s) location(s). Several studies have tested the accuracies of the NLDN. CG stroke and flash detection efficiencies of the NLDN were tested using video cameras in Southern Arizona, Oklahoma, and Texas (Biagi *et al.* 2007). In Arizona, the NLDN stroke detection efficiency was approximately 76 percent, and in Oklahoma/Texas the stroke detection efficiency was 85 percent. The corresponding flash efficiencies in Arizona was 93 percent and in Oklahoma/Texas was 92 percent. Detailed descriptions of other past experiments done that tested the efficiencies and accuracies of the NLDN can be found in Rakov (2016). Presently, the NLDN is one of the most tested and peer reviewed lightning detection networks. Data provided by the NLDN of the storms sampled during the CapeEx19 field campaign allow for interpretation of how electrically active and the level of maturity the storms are before, during, and after aircraft sampling.

In addition to the NLDN, data from The Kennedy Space Center's Lightning Mapping Array (LMA) data is utilized for further interpretation of the lightning associated with the storms sampled

during CapeEx19. As of 2015, the LMA consists of nine stations strategically spread out around Cape Canaveral, Florida. The LMA uses the TOA method and is able to geolocate (by triangulation) lightning discharge points in three-dimensions using sensors that pick up on very high frequency (VHF) sources associated with lightning discharges (Mailyan *et. al.* 2018).

In contrast to the NLDN, the LMA is a more localized detection network. It has been found that the accuracy of the LMA is limited to approximately 100 km away from the nearest sensor (Boccippio *et al.* 2001; Thomas *et al.* 2004). Nevertheless, the LMA is similar to the usefulness as the NLDN, though, the LMA provides additional information into storm morphology and electrical charge structure. The LMA data is visualized via GUI using the ANGEL software package developed by New Mexico Tech and is available upon request.

All relevant code related to this work is open-sourced and can be accessed at: https://sourceforge.net/p/nairy-grad-thesis/code/ci/master/tree/.

CHAPTER III

METHODOLOGY

This analysis uses the LROSE-TITAN derived distance from storm core to determine the changes that occur in the microphysical characteristics during the 3 August 2019 first flight of the CapeEx19 field campaign. The PHIPS is used to investigate the microphysical characteristics of the observed chain aggregates. An analysis of the particle sizes (maximum diameter) of the imaged chain aggregates is performed. The maximum diameter is measured individually by both cameras (C1 and C2). Since the PHIPS cameras are separated by an angular distance of 120 °, the particle sizes will differ between the two cameras depending on the orientation of the particle within the FOV. Therefore, the camera that obtains the largest particle size for the observed particle is used. The resolution of the PHIPS also allows for identification of the habits of each crystal element within a chain aggregate. Moreover, riming on the aggregates can be discerned.

The PHIPS obtains a large number of particle images during several hours of cloud sampling. There is currently no available artificial intelligence particle classification software; therefore, manual particle classification is performed. Classification software designed specifically for the PHIPS (Figure 3) by researchers at Karlsruhe Institute of Technology (KIT) is used for particle classification. The software has many classification options with a confidence rating. The confidence rating attribute is vital when classifying the chain aggregates due to the nonhomogeneous nature of these particles. The software displays both particle viewing angles, which can result in a different classification than having only one view (see Appendix B for details on classification software).

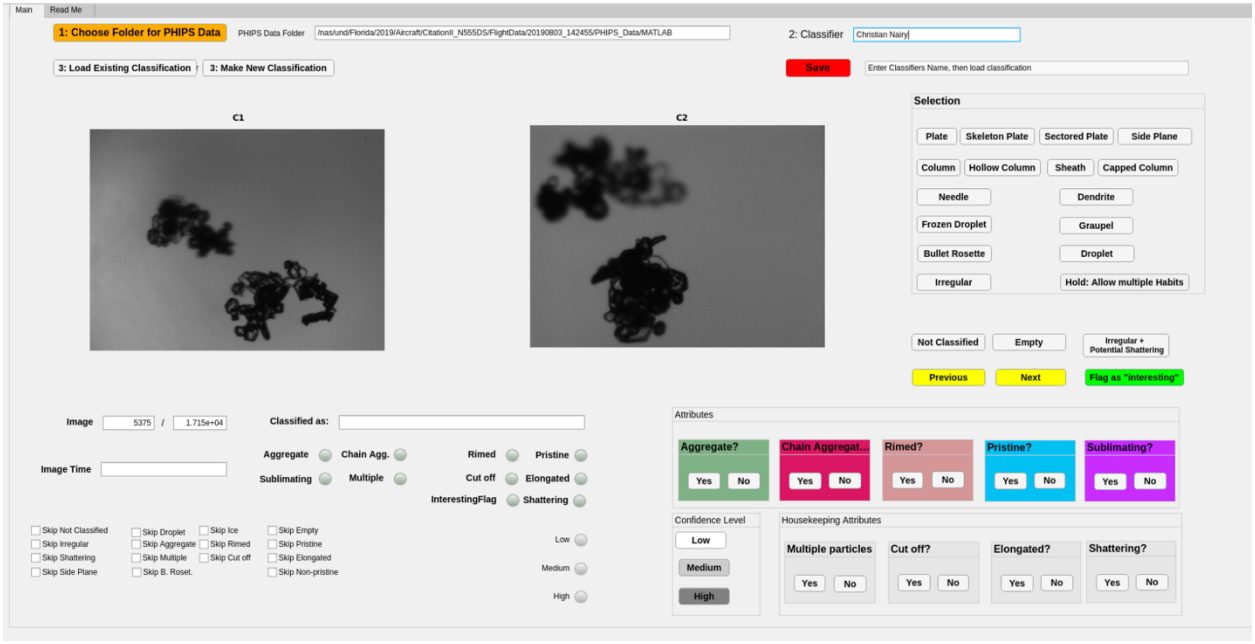

Figure 3. Image showing the Particle Habit Imaging and Polar Scattering (PHIPS) classification software's (developed by Emma Järvinen and Fritz Waitz from KIT) main window display. The individual cameras are labelled as C1 and C2 which provide particle images separated by 120 °. The user selects the crystal habits in the top right section and adds attributes using the bottom right section. A window is available to indicate confidence level.

Several airborne and laboratory papers have discussed chain aggregates; however, no widely accepted definition is available in the literature besides a general description that chain aggregates are elongated and comprise multiple crystals. The more than 17,000 PHIPS images from the 3 August 2019 flight show that chain aggregates have many different sizes, shapes, and habits. Some commonalities of the observed chain aggregates include multiple particles oriented in a linear fashion; very small joints that act to bridge multiple particles together; and unusually elongated aggregates. To separate chain aggregates from regular aggregates, a concrete definition is needed. The definition must be flexible to account for the nonhomogeneous nature of the chain aggregates. The non-homogeneity cause is unknown, however, it is likely related to the aggregation efficiency dependence on temperature and electric field strengths (Saunders and Wahab 1975). Crystals have long cloud residence times over which the temperature and electric field strength can have large variations since chain aggregation likely occurs in multiple cloud regions of a thunderstorm

(Connolly *et al.* 2005). Thus, the confidence rating is used to account for the observed inhomogeneity of the chain aggregates and provides a non-Boolean characteristic to the classification.

A chain aggregate is required to have at least one of three characteristics: (1) three or more discernable particles oriented in a quasi-linear fashion; (2) particles joined together by small joints; and (3) links of particles that are unusually elongated. The term particle refers to both individual crystals and also groups of individual crystals. If one, two, or all three definitions are observed, the confidence value of one, two, or three is applied, respectively (Figure 4). Confidence level 1 is considered low confidence, confidence level 2 is moderate confidence, and confidence level 3 is high confidence. Manual classification is subjective and has subjective confidence levels; however, high confidence levels should provide less subjective differences.

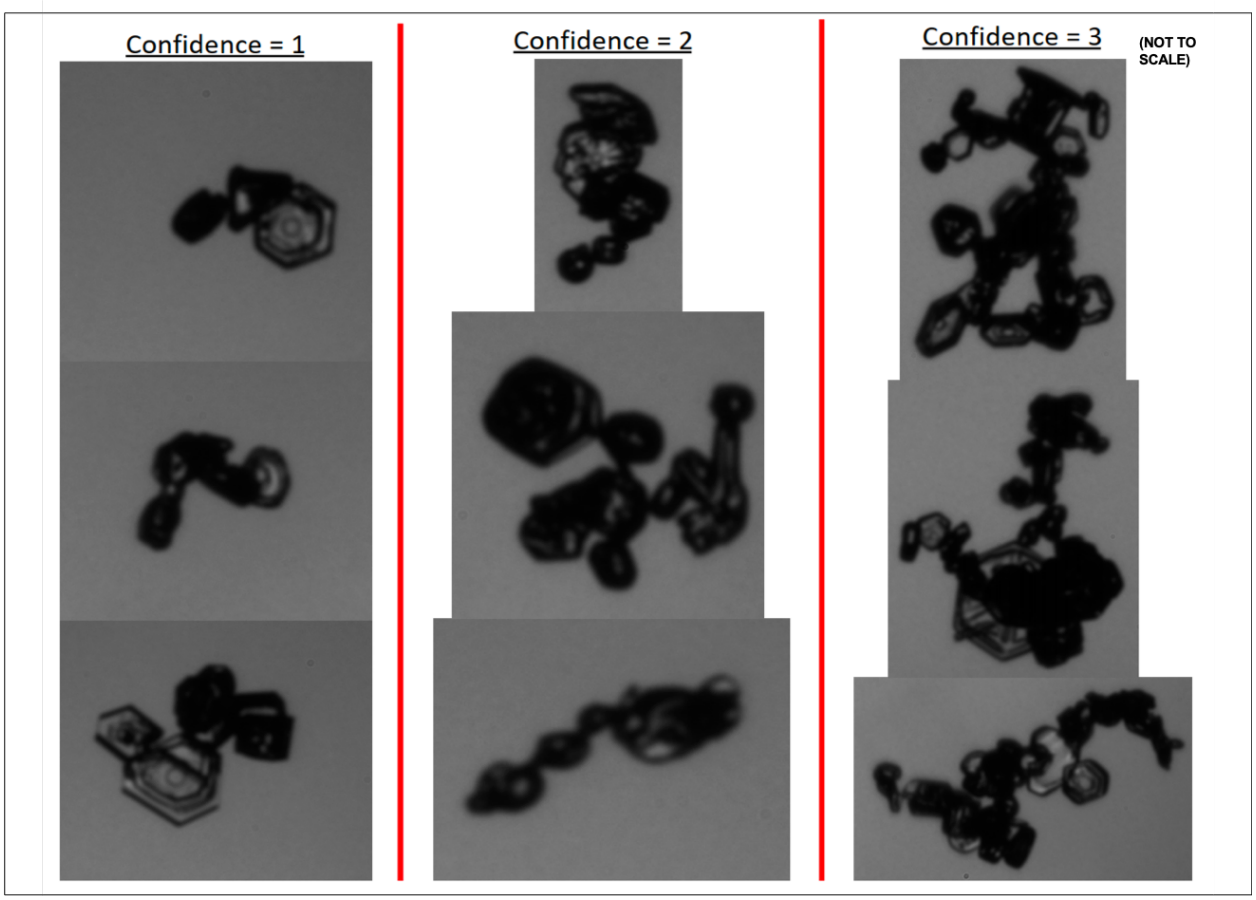

Figure 4. Image showing chain aggregates of different confidence levels. Confidence level 1 crystals have three particles oriented in a quasi-linear fashion; however, no small joints are observed and the crystals are not unusually elongated. Confidence level 2 crystals have more than three particles oriented in a quasi-linear fashion and contain small joints; however these crystals are no unusually elongated. Confidence level 3 crystals contain three or more particles oriented in a quasi-linear fashion, contain small joints, and are unusually elongated.

While the PHIPS obtains high-resolution images, the necessary off-loading of the charge couple device (CCD) array limits the number of particles sampled. The low particle sampling rate (25 Hz) results in a low sampling volume. Compared to the PHIPS, the CIP has a larger sample volume and can provide accurate particle concentrations. The CIP particle concentrations is used to determine the concentration of chain aggregates. First, the PHIPS data is used to determine the size of the majority of chain aggregates (with moderate-to-high confidence). Next, that size is applied to obtain a number concentration of chain aggregates from the CIP data. The CIP particles less than 105 μm in diameter are disregarded from this work due to the problematic nature of fragmentation due to shattering from the probe tips and the particles near the probe's depth of field (O'Shea et al. 2019).

All remote sensed (electric field, radar, satellite, and lightning) measurements are utilized to put the observed in-situ microphysical changes (with respect to distance from the storm core) into context. The first step is to examine the storm environment and the evolution of the storm that produces the anvil where the chain aggregates are observed.

CHAPTER IV

3 AUGUST 2019 CASE STUDY

Storm Environment and Evolution

The storm system sampled on 3 August 2019 first initiated off the southwestern coast of Florida (northwest of Naples, Florida) around 07:30 UTC (3:30 AM EST) by an apparent land-breeze circulation. Between 07:30 and 12:30 UTC, the storm system moves northeastward over Florida where the storm system proceeds to merge into a convective line of thunderstorms (Figure 5a). The convective line reaches central Florida at approximately 13:30 UTC where the line weakens and becomes less organized (Figure 5c). Weakening of the storm is apparent from Geostationary Operational Environmental Satellite (GOES-16) visible imagery where cloud tops appear more diffuse (Figure 6a-c) and the cirrus clouds produced by the convection is spreading outwards, mainly to the north, east, and south. The line's northern half is able to maintain a weakened convective structure as the line moves east northeastward into a surface boundary region with high surface relative humidity, moderate instability, and a lack convective inhibition. At approximately 14:00 UTC, the surface boundary is situated west-southwest to the east northeast from Lakeland, Florida to Titusville, Florida. At this boundary, moist south westerly flow converges with dryer continental north westerly flow that originates from Georgia and Alabama. This surface convergence aids in the storm enhancement of previously formed convection (Figure 6d). The initiation of new convection after 14:00 UTC along this boundary is seen in the radar reflectivity (Figure 5d) and the increase frequency of lightning (Figure 7).

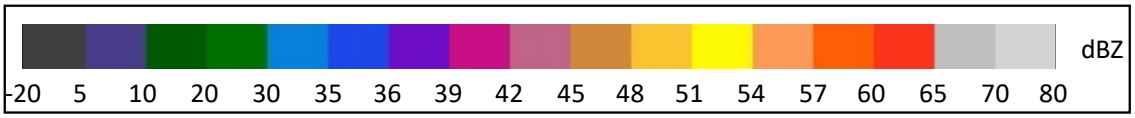

(a) 12:29:24 UTC (b) 13:02:14 UTC (c) 13:29:48 UTC

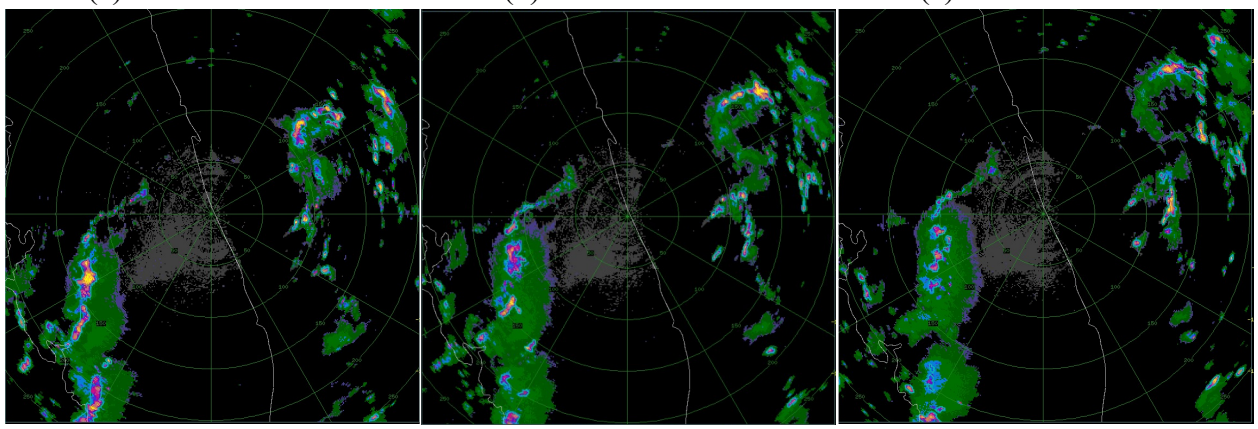

(d) 13:59:49 UTC (e) 14:29:12 UTC (f) 15:03:43 UTC

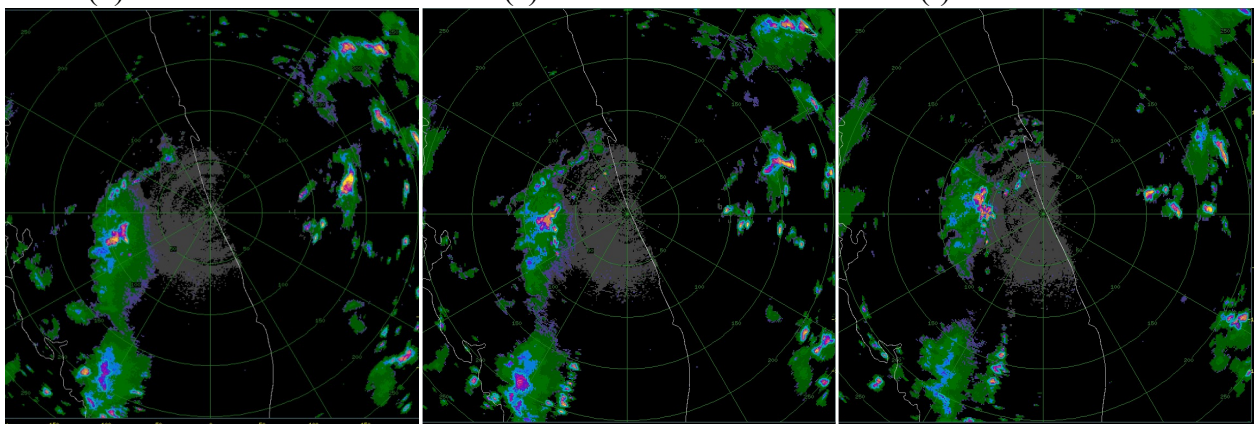

(g) 15:33:11 UTC (h) 16:02:01 UTC (i) 16:32:38 UTC

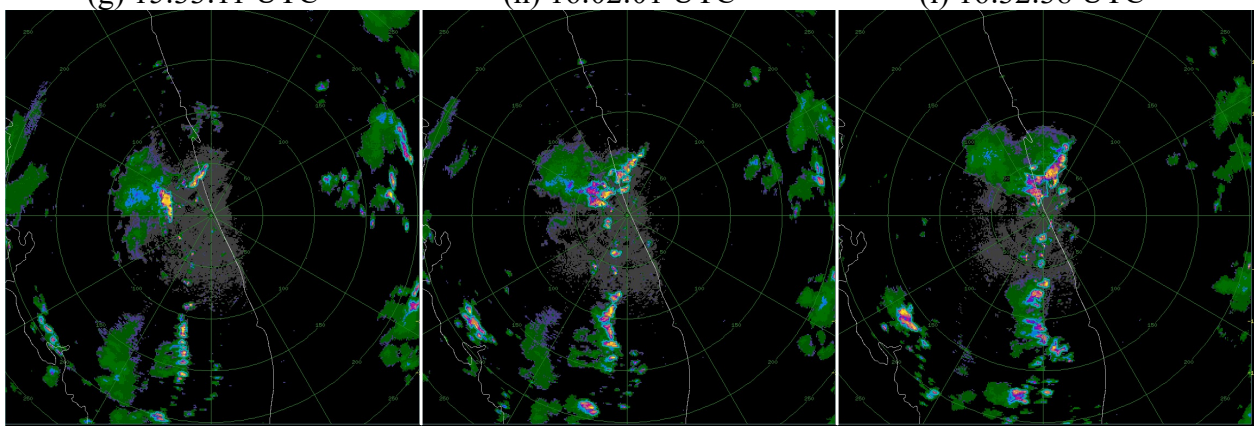

Figure 5. Composite radar reflectivity image from the Melbourne, Florida National Weather Service (NWS) Next-Generation Radar (NEXRAD) WSR-88D (KMLB) in 30-minute intervals showing the convection over Florida on 3 August 2019. The various convective storm cores are outlined in blue (utilizing a threshold of 35 dBZ) using TITAN cell tracking software. Range rings are displayed in thin green lines and expand outward radially in intervals of 50 km.

(a) 12:31:48 UTC (b) 13:01:48 UTC (c) 13:31:48 UTC

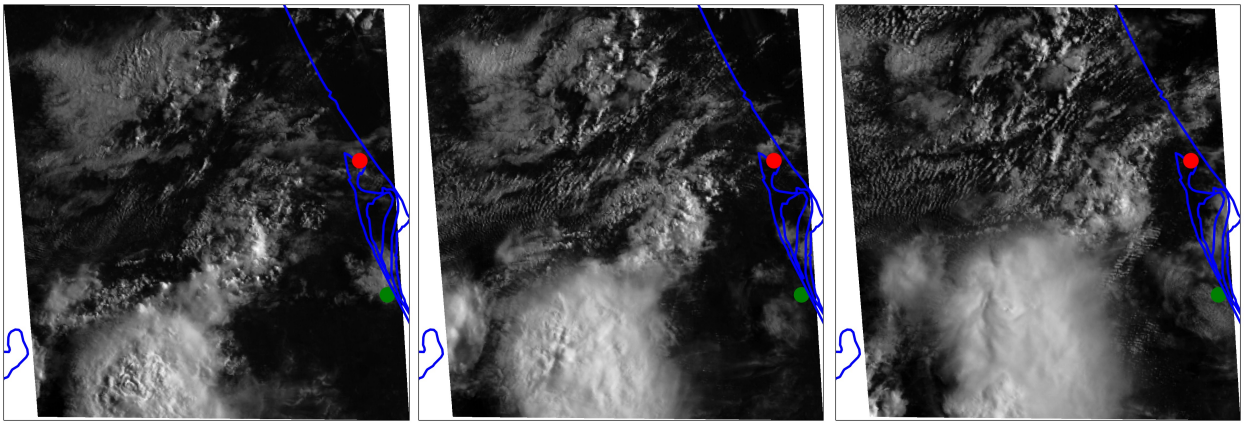

(d) 14:01:48 UTC (e) 14:31:48 UTC (f) 15:01:48 UTC

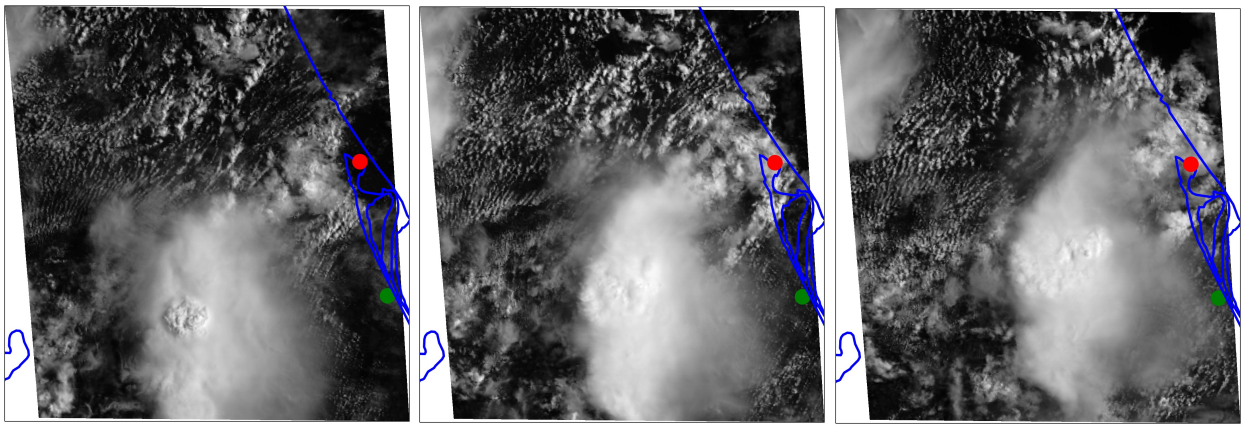

(g) 15:31:48 UTC (h) 16:01:48 UTC (i) 16:31:48 UTC

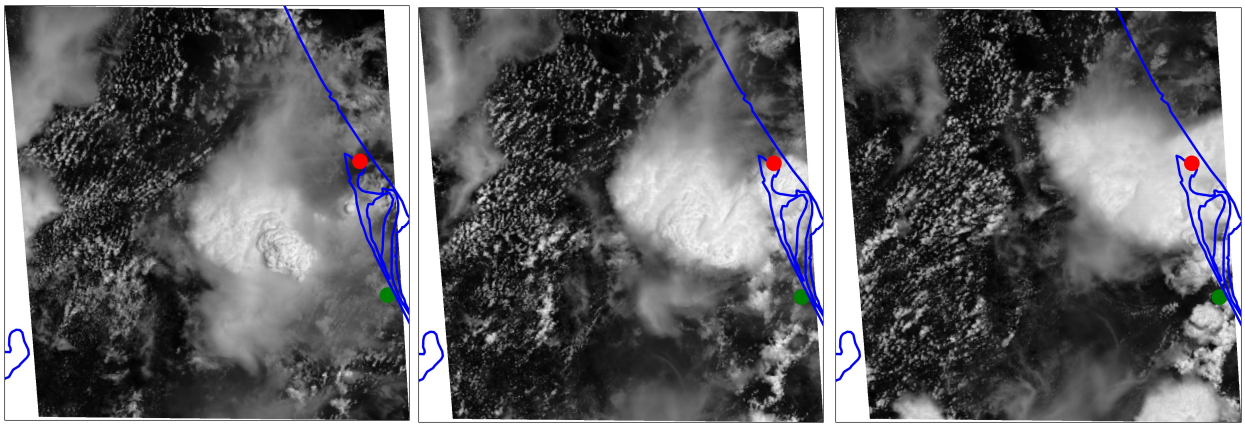

Figure 6. Visible (0.64 μm wavelength) satellite imagery from the Geostationary Operational Environmental Satellite (GOES-16) in 30-minute intervals showing the cloud tops west of Cape Canaveral, Florida on 3 August 2019. Images are at the closest time period and show a similar area as the radar observations (Figure 5). Depicted satellite coordinate have latitude limits between 27.5 °N and 29.5 °N and longitude limits of 83 °W and 80 °W. The red circle indicates the location of the CPR-HD. The green circle indicates the location of the Melbourne, Florida, National Weather Service radar (KMLB). The blue outline displays the Florida coastline.

At 14:00 UTC, the cell's main convective region is approximately 80 km west from the KMLB radar site (Figure 5d) and the cell's overshooting-top can be seen in the visible satellite imagery (Figure 6d). Between 14:15 and 15:10 UTC, the convective region begins to weaken while moving to the east northeast (Figure 5e, f; Figure 6e, f) likely due to the weak mid-to-upper level vertical wind shear (Figure 8). While the cell is moving to the east northeast, the cirrus anvil associated with the cell spreads in all directions but mainly to the north (Figure 6d-f). At approximately 15:10 UTC, the convective cell is re-enhanced while moving along the surface boundary (Figure 5g; Figure 6g). For clarity purposes, the re-enhanced convective cell discussed herein corresponds to the TITAN cell defined by the 35 dBZ composite reflectivity (blue outline in Figure 5). The TITAN cell is able to maintain its convective strength for approximately 45 minutes (between approximately 15:10 and 15:55 UTC). Between 15:10 and 15:55 UTC, the TITAN cell contained several updraft cores and was able to maintain its convective strength. During this time, the TITAN cell peaks in reflectivity (between 55 and 57 dBZ) and the storm peaks in electrical activity (Figure 7) The overshooting cloud top associated with the TITAN cell becomes apparent by approximately 15:30 UTC (Figure 6g). The radar observations and satellite brightness temperatures indicate the overshooting cloud top reaches above the 15 km AGL tropopause height shown in the 15:00 UTC Cape Canaveral sounding. The cirrus anvil from the TITAN cell moves to the north northeast (Figure 6g, h) which is dissimilar to the direction of motion of the cirrus anvil from previously formed convection (Figure 5d; Figure 6g, h). The sounding shows little vertical speed and

directional wind shear. However, the lack of wind directional shear and the steady wind speed of approximately 5 m s^{-1} results in a cell vertical tilt to the north northeast.

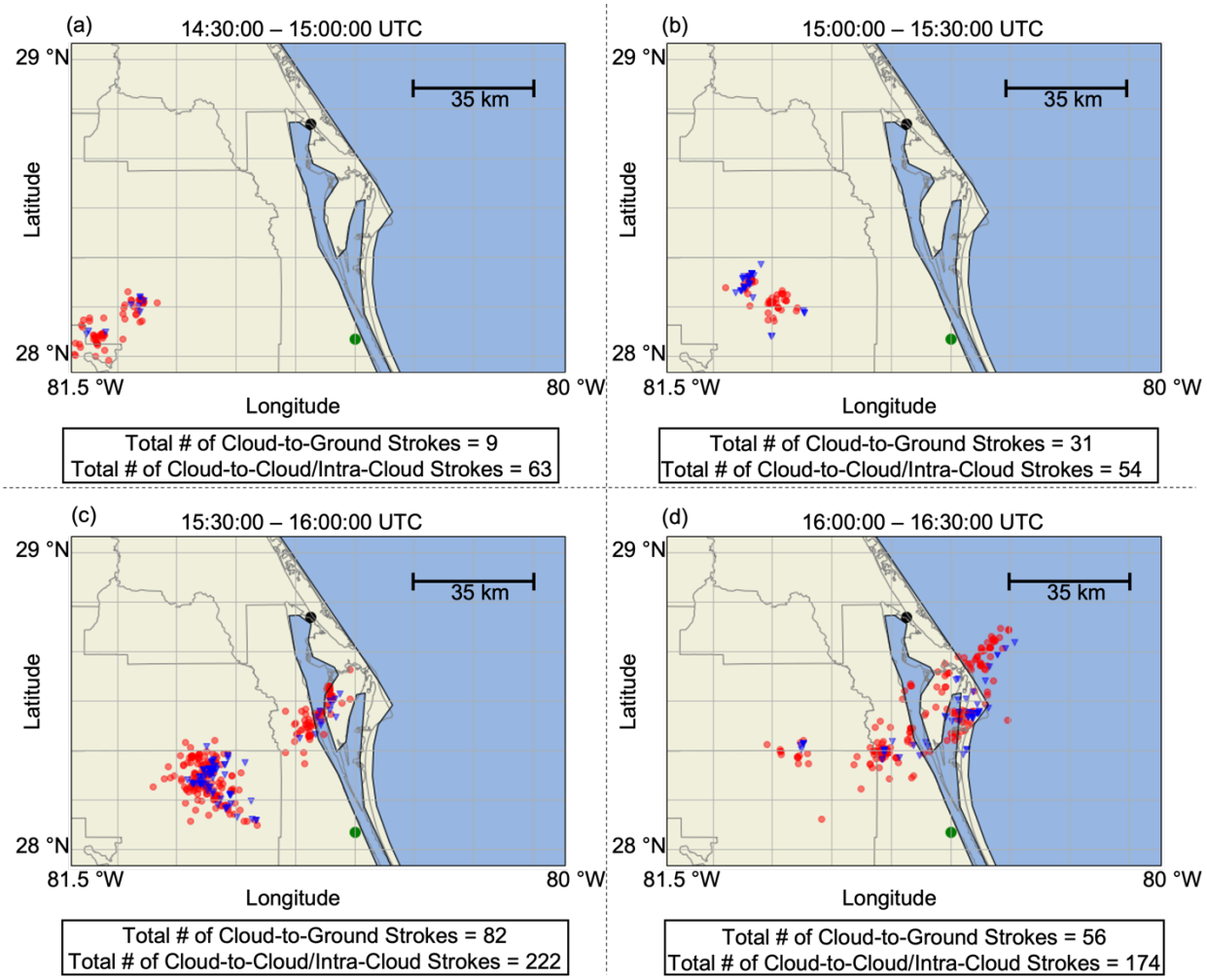

Figure 7. National Lightning Detection Network stroke data for 30-minute intervals on 3 August 2019. The blue inverted triangles indicate cloud-to-ground (CG) lightning strokes and the red circles indicate cloud-to-cloud/intra-cloud (CC/IC) lightning strokes. The green circle denotes the Melbourne, Florida, National Weather Service WSR-88D radar (KMLB) location, and the black circle denotes the CPR-HD radar location. The lightning stroke data displayed is bounded between 28.0 °N to 29.0 °N latitude and 81.5 °W to 80 °W longitude.

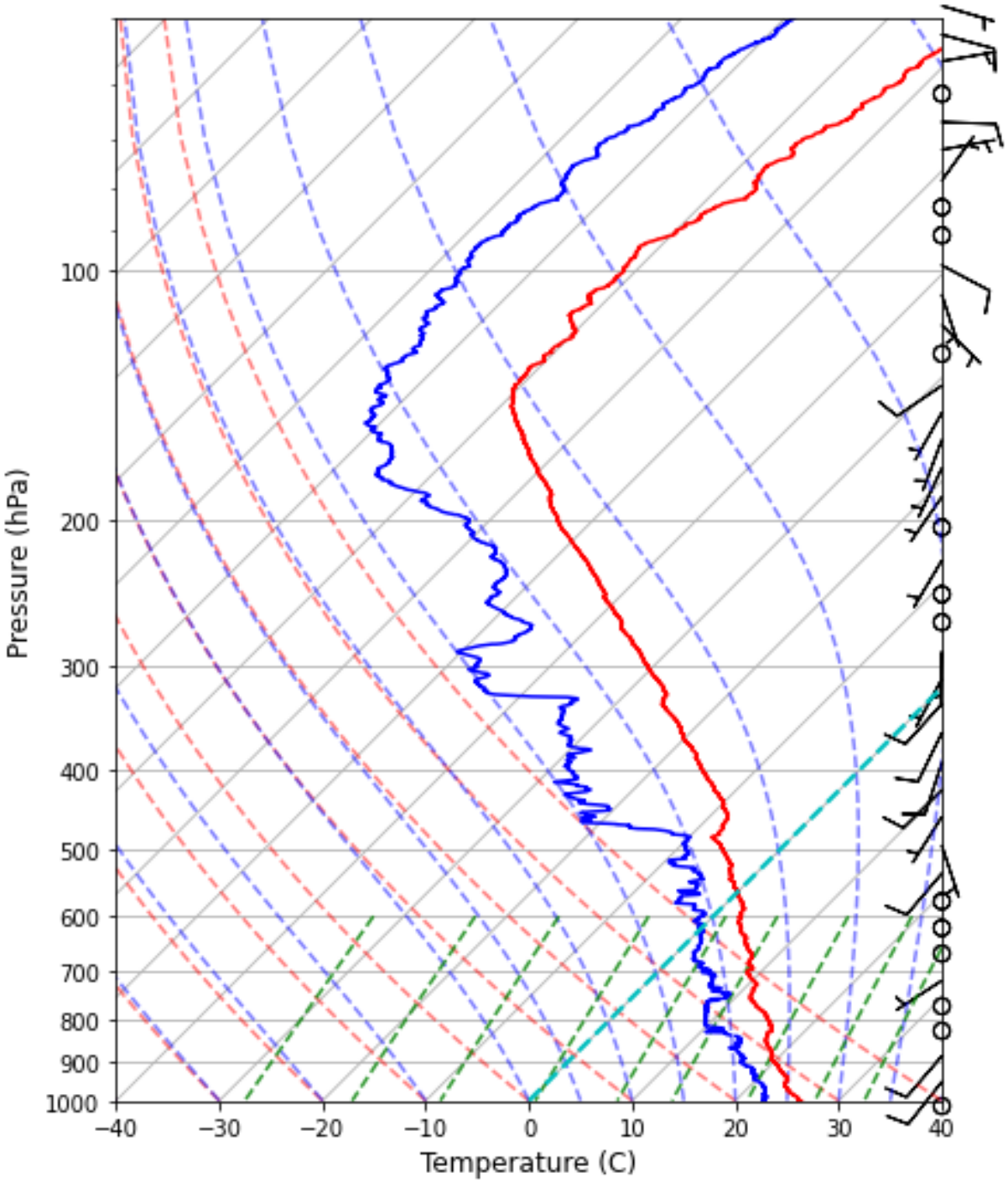
Pressure (hPa)
100
200
300
400
500
600
700
800
900
1000
−40
−30
−20
−10
0
10
20
30
40
Temperature (C)

Figure 8. Atmospheric profile from the radiosonde launch that occurred at 15:00:00 UTC on 3 August 2019 from the field station in Cape Canaveral, Florida. Data from the radiosonde is plotted in skew-T log-P format. The red (solid line) represents temperature and the blue (solid) line represents the dew-point temperature. Wind barbs in knots are displayed on the right-hand side of the plot.

After approximately 16:00 UTC, the TITAN cell begins to decay, become less organized, and become more multi-cellular. At 16:01:43 UTC, the last lightning strike associated with the TITAN cell occurs. After approximately 16:30 UTC, the remanences of the TITAN cell begins to merge with other convective cells which initiated further to the east northeast (on the coastline of Florida) by the same convergence boundary (Figure 5h; Figure 6h). In addition, the cirrus anvil associated with the TITAN cell begins to merge with other cirrus anvils associated with the other storms (Figure 5i; Figure 6i). The merged cells continue to move east northeastward where finally, at approximately 18:30 UTC, they deteriorate over the Atlantic Ocean.

Flight Legs

The first research flight on 3 August 2019 has five individual flight legs where the aircraft altitude is constant and there are no sharp turns (turnarounds) and/or maneuvers (Figure 9; Table 2). During flight leg one (FL1), the North Dakota Citation II Research Aircraft samples the outer regions of cirrus anvil clouds produced from the convection prior to 15:10 UTC. Aircraft sampling during FL1 (between 15:51:15 and 16:01:00 UTC) occurs while the TITAN cell is in its mature stage and contains several updrafts. During the last part of FL1 (between 15:57:00 and 16:01:00 UTC), the aircraft samples the cirrus anvil associated with the TITAN cell below its overshooting top, which is offset from the low-level (5 km AGL), high radar reflectivity region (Figure 9a) by approximately 15 and 20 km. Flight leg 2 (FL2) follows a similar, but shorter ground track as FL1 after a turn-around to the northbound direction. The TITAN cell's low-level reflectivity starts to weaken toward the ending of FL2. Flight leg 3 (FL3) closely re-traces the ground track of FL1.

Toward the end of FL3, the TITAN cell begins to merge with other convective cells to the east. As Flight leg 4 (FL4) commences, the TITAN cell's induced cirrus anvil expands further to the north northwest. FL4 does not approach as close to the core as FL1-3. FL4 is also slightly warmer (by approximately 2 °C) than the other flight legs. This slight warming is most likely due to dynamical heating in the anvil via deposition.

FL5 is different than FL1-4 by sampling at a higher altitude (approximately 11.3 km AGL) and being from the east northeast to the west southwest, which is approximately parallel to the TITAN cell's direction of motion. Additionally, FL5 also samples cirrus anvil clouds induced from the newer convective cells that initiated on the eastern coast of Florida (east northeast of the TITAN cell) as well as from the TITAN cell. Due to the east to west flight orientation of FL5, only FL1-4 are compared with an in-depth focus on FL1 and FL4 since these flight legs sampled the TITAN cell's induced cirrus anvil during different storm phases; where the TITAN cell is in its mature phase during FL1, and in its dissipating phase during FL4.

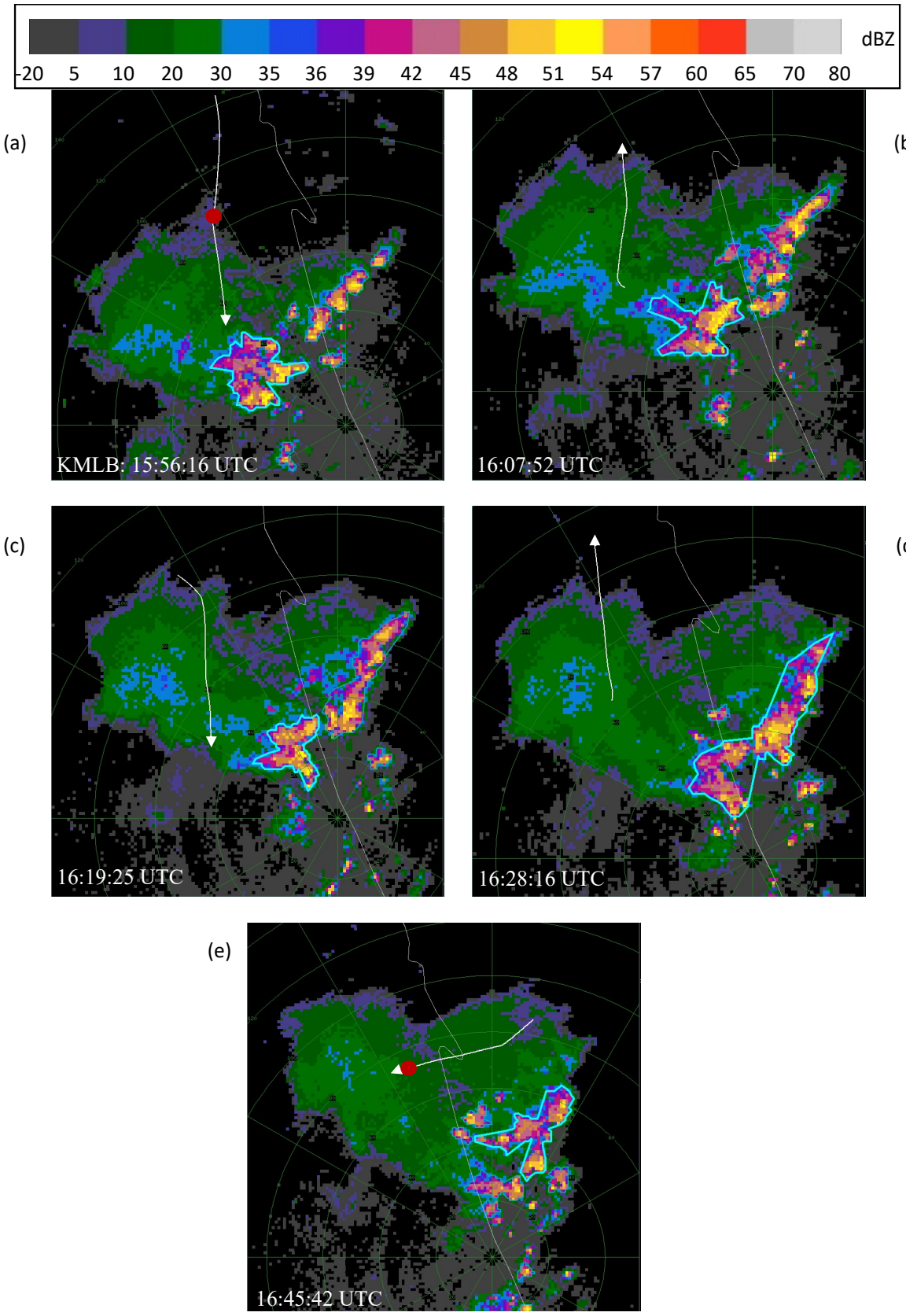
dBZ
-20 5 10 20 30 35 36 39 42 45 48 51 54 57 60 65 70 80
(a)
KMLB: 15:56:16 UTC
(b)
16:07:52 UTC
(c)
16:19:25 UTC
(d)
16:28:16 UTC
(e)
16:45:42 UTC

Figure 9. Collage of images showing the individual flight legs (white line with arrow) on the 3 August 2019 flight with the Melbourne, Florida National Weather Service (NWS) Next-Generation Radar (NEXRAD) WSR-88D (KMLB) composite radar reflectivity (dBZ) that completes (timestamp in white text at the bottom left hand corner of each window) closest to the flight leg. The length of each flight leg corresponds to the time span given above the image. The arrow attached to the end of the flight track line represents the end of the flight leg as well as direction of flight. The images with a red circle represent the aircraft position with the corresponding KMLB timestamp. The images without a red circle depicts that the volume scan finished after the ending of the flight leg. Thin blue lines outline the various convective storm cores (utilizing a threshold of 35 dBZ) using TITAN cell tracking. The thick blue lines that outline the convection depict the TITAN cells that are used in calculating the aircraft distance from the storm core reflectivity centroid (also using a 35 dBZ threshold). Panel (a) is flight leg one (FL1) which spanned from 15:51:15-16:01:00 UTC. Panel (b) is flight leg two (FL2) which spanned from 16:02:00-16:07:00 UTC. Panel (c) is flight leg three (FL1) which spanned from 16:09:00-16:17:00 UTC. Panel (d) is flight leg four (FL4) which spanned from 16:21:30-16:27:00 UTC. Panel (e) is flight leg five (FL5) which spanned from 16:40:00-16:46:00 UTC.

Table 2. Table depicting the time span, direction of flight heading, mean altitude (m), and mean temperature (°C) for each flight leg during the 3 August 2019 first flight. Values in parenthesis is the standard deviation from the mean.

Legs	Time Span (hh:mm:ss)	Heading	Altitude	Temperature
FL1	15:51:15-16:01:00 UTC	Southbound	10,029 (± 4) m	-33.7 (± 0.4) °C
FL2	16:02:00-16:07:00 UTC	Northbound	10,034 (± 5) m	-33.4 (± 0.3) °C
FL3	16:09:00-16:17:00 UTC	Southbound	10,035 (± 5) m	-32.6 (± 0.9) °C
FL4	16:21:30-16:26:55 UTC	Northbound	10,021 (± 7) m	-29.8 (± 0.3) °C
FL5	16:40:00-16:46:00 UTC	Westbound	11,321 (± 5) m	-43.6 (± 0.5) °C

Microphysical Observations

The North Dakota Citation II Research Aircraft does not sample in the convective core (highest reflectivity region between 2 and 7 km AGL) during the CapeEx19 field project but focused on sampling in the anvil out flow region. Sampling in the convective core can be problematic as aircraft lightning strikes can damage instruments.

Aircraft sampling legs occurred with little fluctuations in temperature between -29 °C and -35 °C (Table 2), which is slightly warmer than the homogenous freezing level. For each flight leg, the total water content (TWC) increases closer to the storm core (Figure 10). FL1 is slightly different from FL2-4 with a section of lower TWC values between 30 and 42 km from the TITAN cell's storm core, which is due to sampling a slightly more diffuse region of the cirrus anvil (Figure

9a). The Nevzorov, King, and RICE Probes indicate no liquid water is present during FL1 and FL2; therefore, the TWC measurement is of ice. FL3 and FL4 had small amounts of liquid water (<0.1 g m^{-3}) at 30 to 35 km (FL3) and 50 to 55 km (FL4) from the TITAN core.

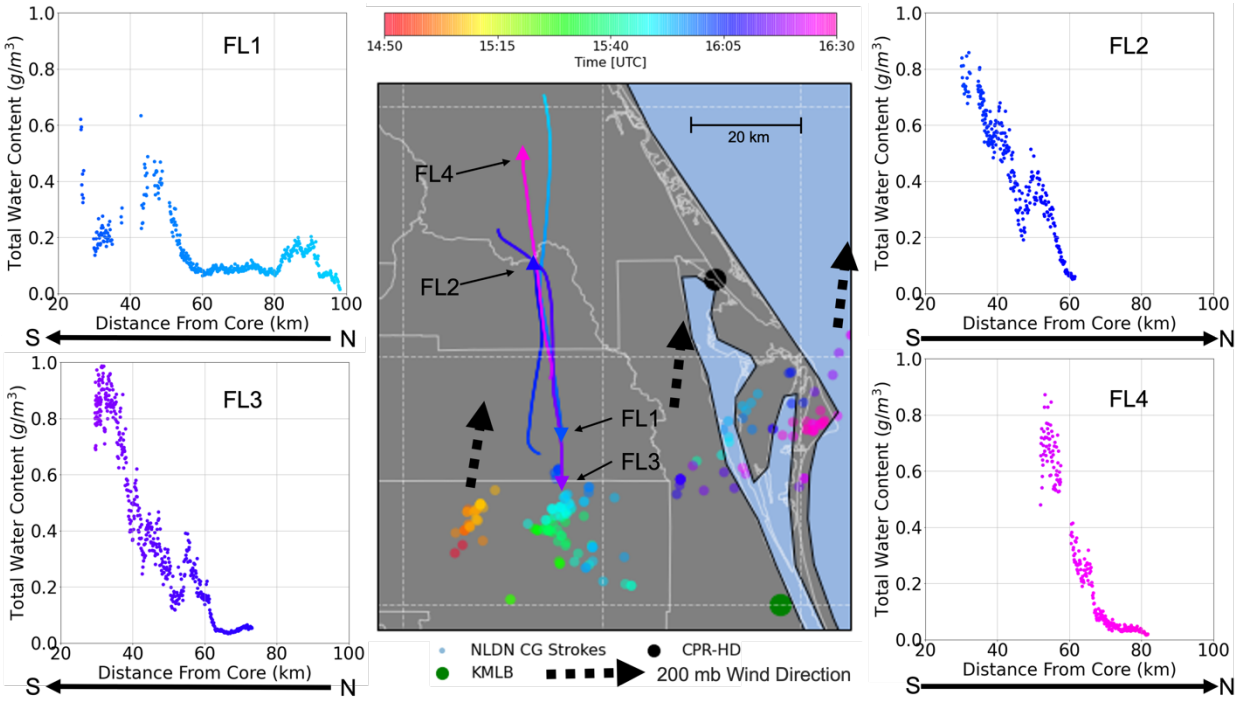

Figure 10. Total water content (1 Hz) for each flight leg (FL1-4) with respect to distance from the TITAN cell's core (reflectivity centroid). Underneath each corner plot, a black arrow depicts the direction the aircraft is flying going forward in time. The center plot shows the locations of each flight leg as well as the locations of the National Lightning Detection Network (NLDN) cloud-to-ground lightning strokes. The color scale represents time for the data shown in each plot. Larger circles on the center plot depict important locations relevant to this work. The black arrows (dashed) overlaid on the center plot represent the 200 mb wind direction as depicted by the radiosonde from Cape Canaveral, Florida, at 15:00 UTC (Figure 8).

The PHIPS probe is able to capture relatively large quantities of chain aggregates during the various flight legs. A total of 4,654 PHIPS images are taken during FL1-4 where 668 (14.4%) are classified as chain aggregates (Table 3). Examples of confidence level 3 chain aggregates from the various flight legs are given in Figure 11. See Appendix C for more chain aggregates with varying confidence levels. The chain aggregates mostly consist of hexagonal plates, although, other particle habits including sectored plates, columns, and capped columns are also apparent. The

chain aggregates do not appear to be perfectly linear, but quasi-linear and sometimes folded over themselves; similar to what was observed in previous cloud chamber experiments and airborne research projects. Small joints connecting the individual ice crystals is visualized in the PHIPS imagery. Majority of the chain aggregates also lack the presence of rimed ice (approximately 90%). Moreover, some of the chain aggregates observed farther away from the TITAN cell's storm core (between 70 and 100 km) show signs of sublimation, which is most likely due to dry air entrainment into the cirrus anvil.

Table 3. Summary of how the Particle Habit Imaging and Polar Scattering (PHIPS) probe images are manually classified as chain aggregates with confidence level of 1, 2, and 3 (see text for definition of increasing confidence level). Also shown is the overall total of all flight legs.

Legs	Number of Images	Confidence of 1	Confidence of 2	Confidence of 3	All Confidences
FL1	1,507	4.6 ± 0.4% (N=69)	5.3 ± 0.5% (N=80)	4.6 ± 0.4% (N=69)	14.5 ± 0.6% (N=218)
FL2	917	4.3 ± 0.5% (N=39)	5.2 ± 0.6% (N=48)	3.4 ± 0.5% (N=31)	12.9 ± 0.8% (N=118)
FL3	1,375	4.7 ± 0.5% (N=64)	6.5 ± 0.5% (N=89)	2.8 ± 0.4% (N=38)	13.9 ± 0.6% (N=191)
FL4	855	4.0 ± 0.5% (N=33)	7.7 ± 0.7% (N=67)	4.8 ± 0.6% (N=41)	16.5 ± 0.8% (N=141)
TOTAL	**4,654**	**4.4 ± 0.2% (N=205)**	**6.1 ± 0.3% (N=284)**	**3.8 ± 0.2% (N=179)**	**14.4 ± 0.3% (N=668)**

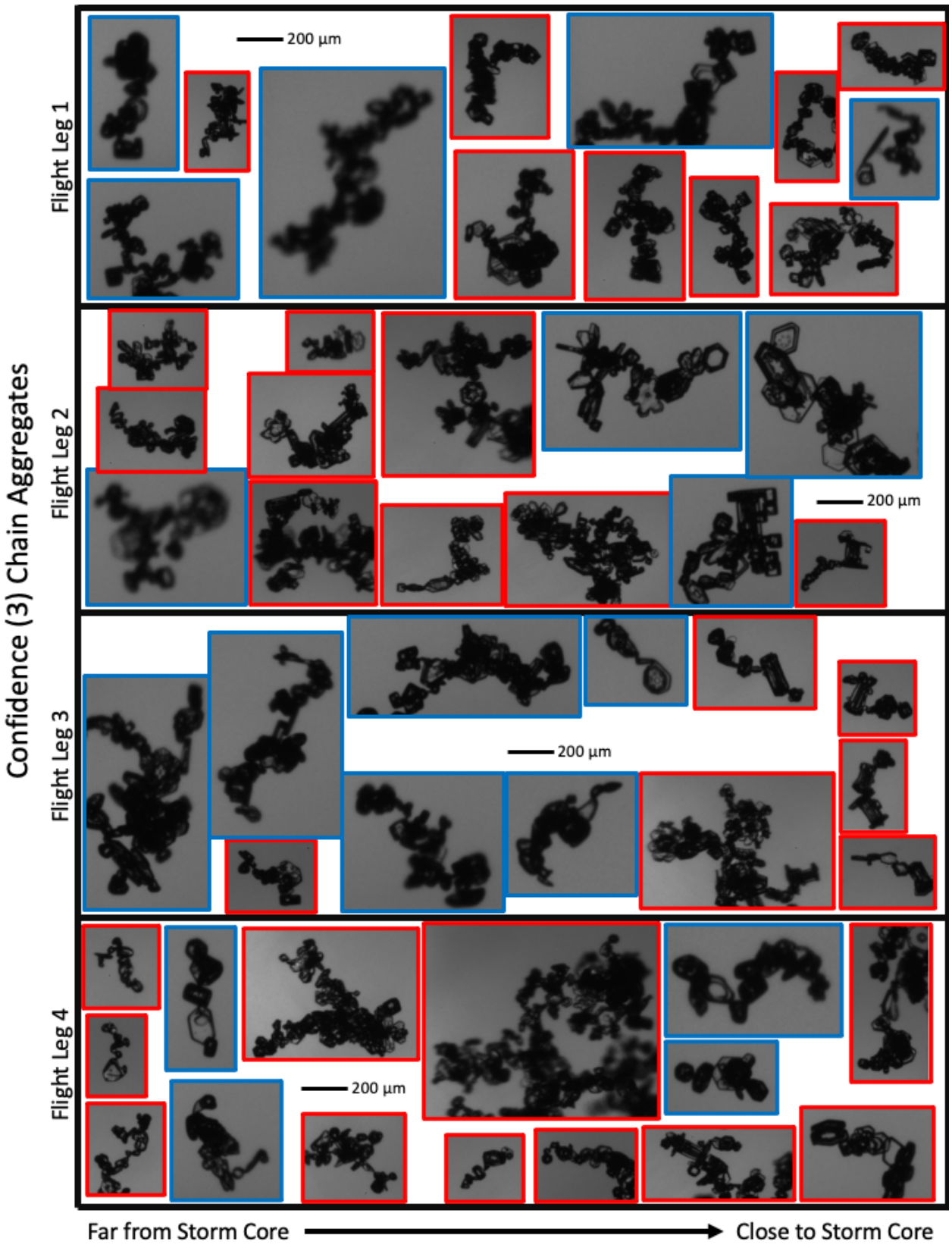
Confidence (3) Chain Aggregates
Flight Leg 1
Flight Leg 2
Flight Leg 3
Flight Leg 4
200 µm
200 µm
200 µm
200 µm
Far from Storm Core
Close to Storm Core

Figure 11. Particle Habit Imaging and Polar Scattering (PHIPS) probe images taken during the CapeEx19 field campaign on 3 August 2019. Chain aggregate collage showing chain aggregates with confidence level of 3 for flight leg 1 (a) [15:51:15-16:01:00 UTC], flight leg 2 (b) [16:02:00-16:07:00 UTC], flight leg 2 (c) [16:09:00-16:17:00 UTC], and flight leg 4 (d) [16:21:30-16:27:00 UTC] with respect to distance from store core reflectivity centroid. Red box images are for PHIPS camera number 1 (C1), while blue box images are for camera number 2 (C2).

The size distribution of the chain aggregates is similar between FL1-4 (Figure 12), indicating that storm evolution does not impact chain aggregate sizes. The average 25th percentile of chain aggregate sizes is 293 μm; the average 50th percentile of chain aggregate sizes is 367 μm; The average 75th percentile of chain aggregate sizes is 458 μm. It is important to note that the PHIPS only attributes sizing information for particles that are completely in-frame, it is possible that some chain aggregates are cut out-of-frame and/or out-of-focus and are much larger than 800 μm.

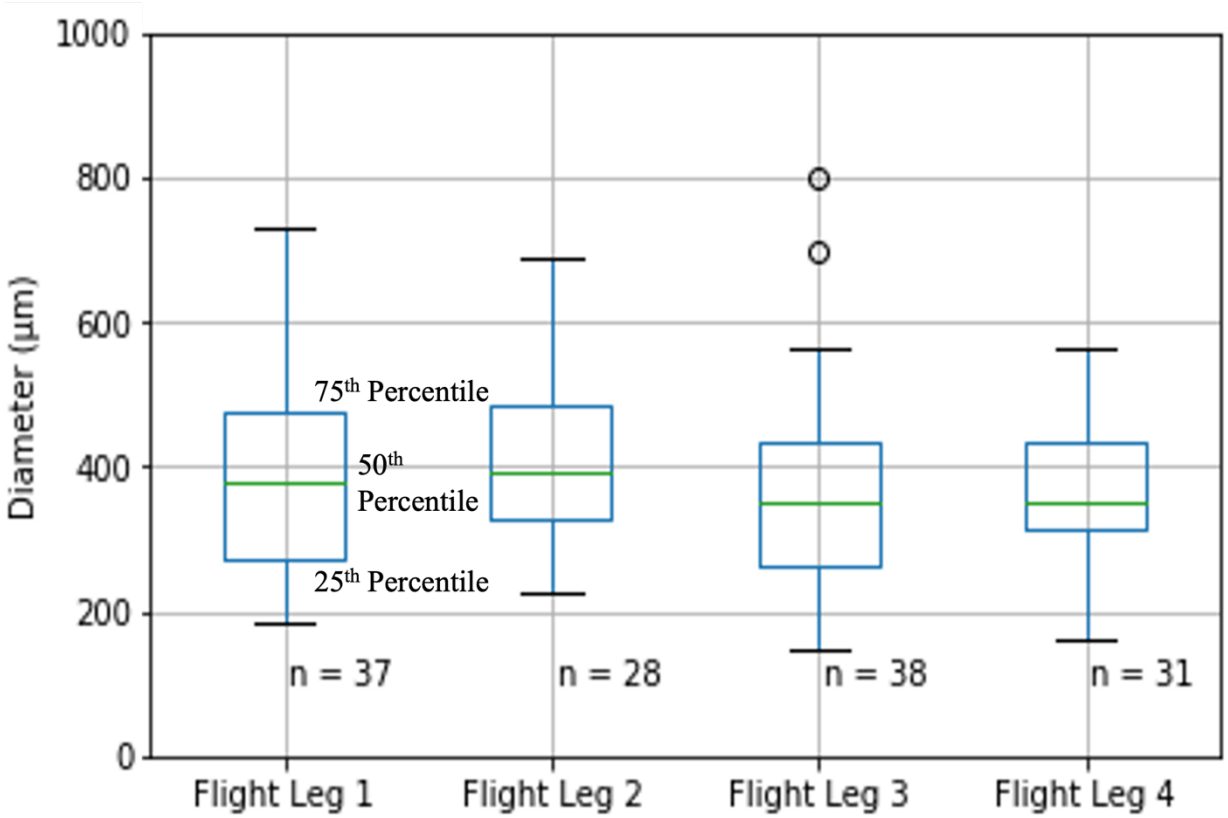

Figure 12. Box-and-whisker plots of the size of the classified chain aggregates (with confidence level of 2 or greater) during flight legs 1 to 4 on the 3 August 2018 first flight as determined using the "fast circle" method. The number of classified particles (n) in each flight leg is given below the box-and-whisker plots.

The smallest number concentrations of chain aggregates (Table 3) are observed during FL2 (12.9%) and the largest number concentrations of chain aggregates are observed during FL4 (16.5%). The highest amount of chain aggregates with a confidence level of 3 are observed during FL1 (69), though, FL4 observes the highest concentration of chain aggregates with a confidence level of 3 (4.8%). The highest concentrations of chain aggregates are found between 70 and 100 km from the TITAN cell's core reflectivity centroid (16.2%), albeit no observations during FL2 is available at the distance range over 70 km (Table 4). Within the 70 to 100 km distance range, the PHIPS has the lowest number of chain aggregates (120) and images (743). The smallest observed concentrations of chain aggregates are between 10 and 40 km from the TITAN cell's core reflectivity centroid (10%), albeit there is no observations during FL4 at this distance range. PHIPS

observations are provided from all flight legs between the 40 and 70 km distance range. The concentrations of chain aggregates between the 40 and 70 km distance range is 16%. The highest number of chain aggregates (420) and PHIPS images (2,628) are observed within the 40-70 km distance range, which is expected since all flight legs sample this range.

Table 4. Particle Habit Imaging and Polar Scattering (PHIPS) probe image and chain statistics for the 3 August 2019 flight. The table shows the percentage of classified chain aggregates (taken from the PHIPS probe) with a confidence of 1, 2 and 3 by the number of PHIPS images per flight leg with respect to distance from TITAN cell's core reflectivity centroid. Also displayed is the total between all flight legs.

	70 – 100 km from Storm Core		**40 – 70 km from Storm Core**		**10 – 40 km from Storm Core**	
Legs	# of Images	All Confidences	# of Images	All Confidences	# of Images	All Confidences
FL1	510	11.4 ± 1.0% (N=58)	631	19.7 ± 1.0% (N=124)	366	9.8 ± 1.1% (N=36)
FL2	N/A	N/A	520	15.0 ± 1.0% (N=78)	397	10.1 ± 1.1% (N=40)
FL3	55	32.7 ± 3.3% (N=18)	800	15.1 ± 0.8% (N=121)	520	10.0 ± 1.0% (N=52)
FL4	178	24.7 ± 1.9% (N=44)	677	14.3 ± 0.9% (N=97)	N/A	N/A
Total	**743**	**16.2 ± 0.9% (N=120)**	**2,628**	**16.0 ± 0.5% (N=420)**	**1,283**	**10.0 ± 0.6% (N=128)**

Compared to other microphysical probes such as the CIP, the PHIPS probe has a much smaller sampling volume and a lower particle count rate. Therefore, it is necessary to relate the PHIPS data to other in-situ particle sampling microphysical probes (like the CIP) to understand chain aggregate concentrations. The PHIPS observations show that the observed chain aggregates (with moderate-to-high confidence) are typically 367 μm (on average) in diameter and as low as 150 μm in diameter (Figure 12). However, 83% of particles with a diameter greater than 495 μm (Table 5) are classified as chain aggregates with moderate to high confidence. Despite the relatively small number of PHIPS particles greater than 495 μm in diameter, this high percentage gives confidence that most of the particles observed in the cirrus anvil region greater than 495 μm in diameter are chain aggregates. Thus, an assumption is made that particles greater than 495 μm in diameter are chain aggregates. This assumption enables using the CIP concentration of greater than 495 μm particles to be used as an accurate concentration measurement of chain aggregates.

Table 5. Table depicting the number of Particle Habit Imaging and Polar Scattering (PHIPS) probe particles, classified chain aggregates (with a diameter measurement attribute) greater than 495 μm, the ratio between the two (Chain Percentage), and the average confidence of the classified chain aggregates per flight leg.

Legs	**Particles > 495 μm**	**Chains > 495 μm**	**Chain Percentage**	**Confidence**
FL1	7	7	100%	2.71
FL2	11	8	73%	2.38
FL3	8	7	88%	2.00
FL4	10	8	80%	1.88
TOTAL	**36**	**30**	**83%**	**2.24**

The total particle concentration peaks when the aircraft is closest to the TITAN storm core (Figure 13); where the particle concentration then trends downward the further the aircraft is away from the TITAN storm core. The decrease in particles as the aircraft samples further from the main convection is expected due to entrainment, particle fallout, and sublimation. The CIP observes the highest concentration of particles (0.92 # cm^{-3}) at the end of FL3 when the aircraft is closest to the TITAN cell's core (~ 30 km). Interestingly, all flight legs have a primary or secondary peak in particle concentration between 40 and 60 km from the TITAN cell's core.

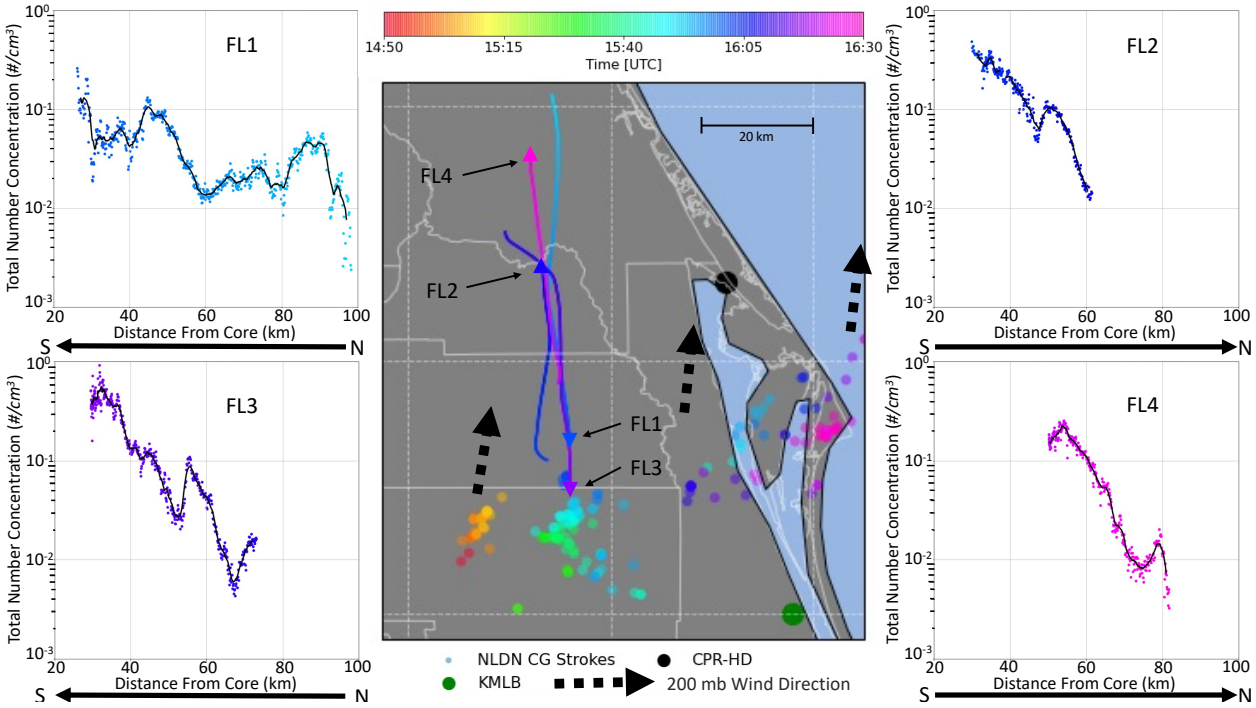

Figure 13. The four corner plots depict the 1 Hz CIP total particle number concentrations (particle concentration greater than 105 μm) for each flight leg versus the distance from the TITAN cell's core with an overlaid 20-point centered moving average (black). Underneath each corner plot, a black arrow depicts the direction the aircraft is flying going forward in time. The center plot shows the locations of each flight leg as well as the locations of the NLDN cloud-to-ground lightning strokes. The color scale represents time for the data shown in each plot. The black arrows (dashed) overlaid on the center plot represent the 200 mb wind direction as depicted by the radiosonde from Cape Canaveral, Florida, at 15:00 UTC (Figure 8).

The PHIPS analysis indicates there are particles between 105 and 315 μm that are chain aggregates. Though, on average, these chain aggregates tend to be lower in confidence mainly due to not being elongated. Therefore, particles less than 315 μm in diameter are non-chain aggregates, and particles from 315 to 495 μm in diameter are assumed to be a mixture of chain and non-chain aggregates and is considered the particle size buffer between the two particle types. Figure 14 shows a downward trend in the chain aggregate concentrations as the aircraft increases its distance from the TITAN cell's core; similar to what is observed in Figure 13. All flight legs have peaks in chain aggregate concentrations when the aircraft is closest to the TITAN cell's core except FL1. FL1 has a peak in the chain aggregate concentration (0.018 # cm^{-3}) between 45 and 50 km away

from the TITAN cell's core. While approaching the core (between 25 and 45 km) the chain aggregate concentrations decrease by an order of magnitude.

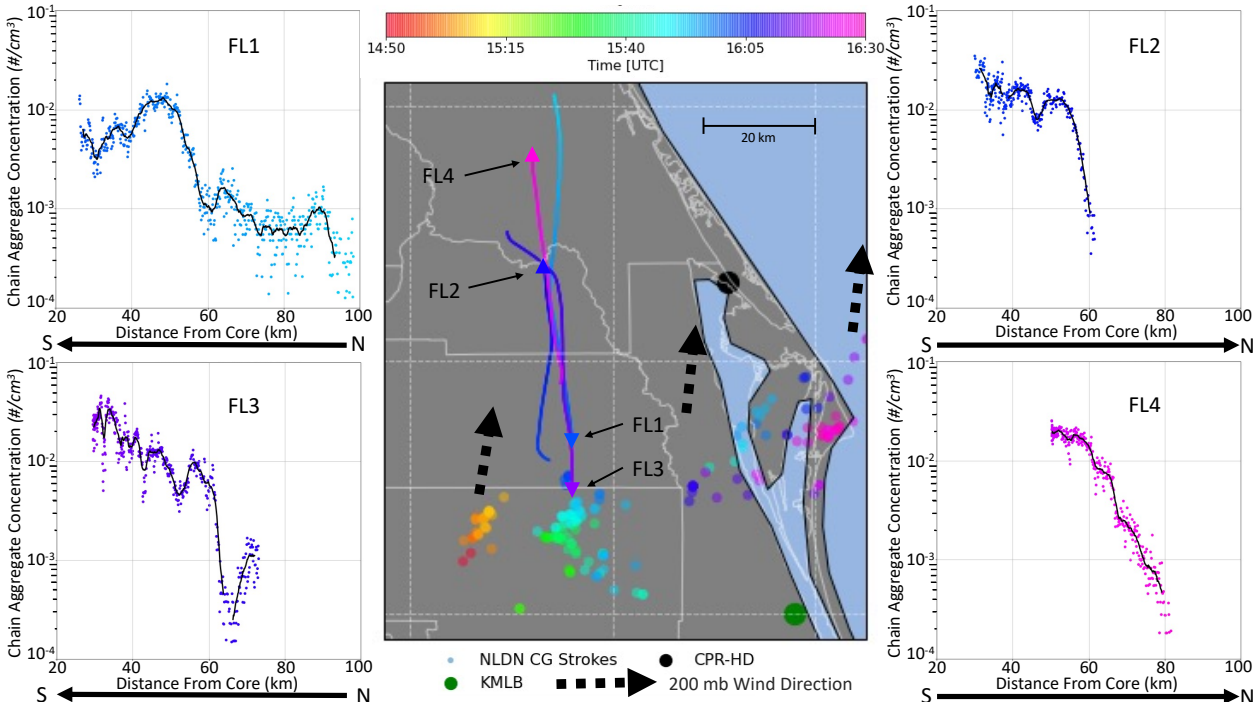

Figure 14. The four corner plots depict the 1 Hz CIP number concentrations greater than 495 µm (chain aggregate concentration) per flight leg with respect to distance from the TITAN cell's core with an overlaid 20-point centered moving average (black). Underneath each corner plot, a black arrow depicts the direction the aircraft is flying going forward in time. The center plot shows the locations of each flight leg as well as the locations of the National Lightning Detection Network (NLDN) cloud-to-ground lightning strokes. The color scale represents time for the data shown in each plot. Larger circles on the center plot depict important locations relevant to this work. The black arrows (dashed) overlaid on the center plot represent the 200 mb wind direction as depicted by the radiosonde from Cape Canaveral, Florida, at 15:00 UTC (Figure 8).

Comparing the moving averages between the chain aggregate concentrations verses the non-chain aggregate concentrations for all flight legs (Figure 15), it is observed that the aircraft is sampling in a region of more non-chain aggregates than chain aggregates. However, for all of the flight legs, the chain and non-chain aggregate concentrations converge at a certain distance from the TITAN cell's core. For FL1, the concentrations of chain aggregates and non-chain aggregates converge at approximately 53 km from the core. According to the CIP measurements, at 55 km from the core the concentrations of chain and non-chain aggregates are virtually the same. For

FL2, the concentrations of chain aggregates and non-chain aggregates converge at approximately 58 km from the core. Similar to FL1 and FL2, FL3 shows the concentrations of chain aggregates and non-chain aggregates converge at two distances from the core. The first being approximately 55 km from the core and the second being around 61 km from the core. For FL4, the concentrations of chain aggregates and non-chain aggregates converge at approximately 70 km from the core.

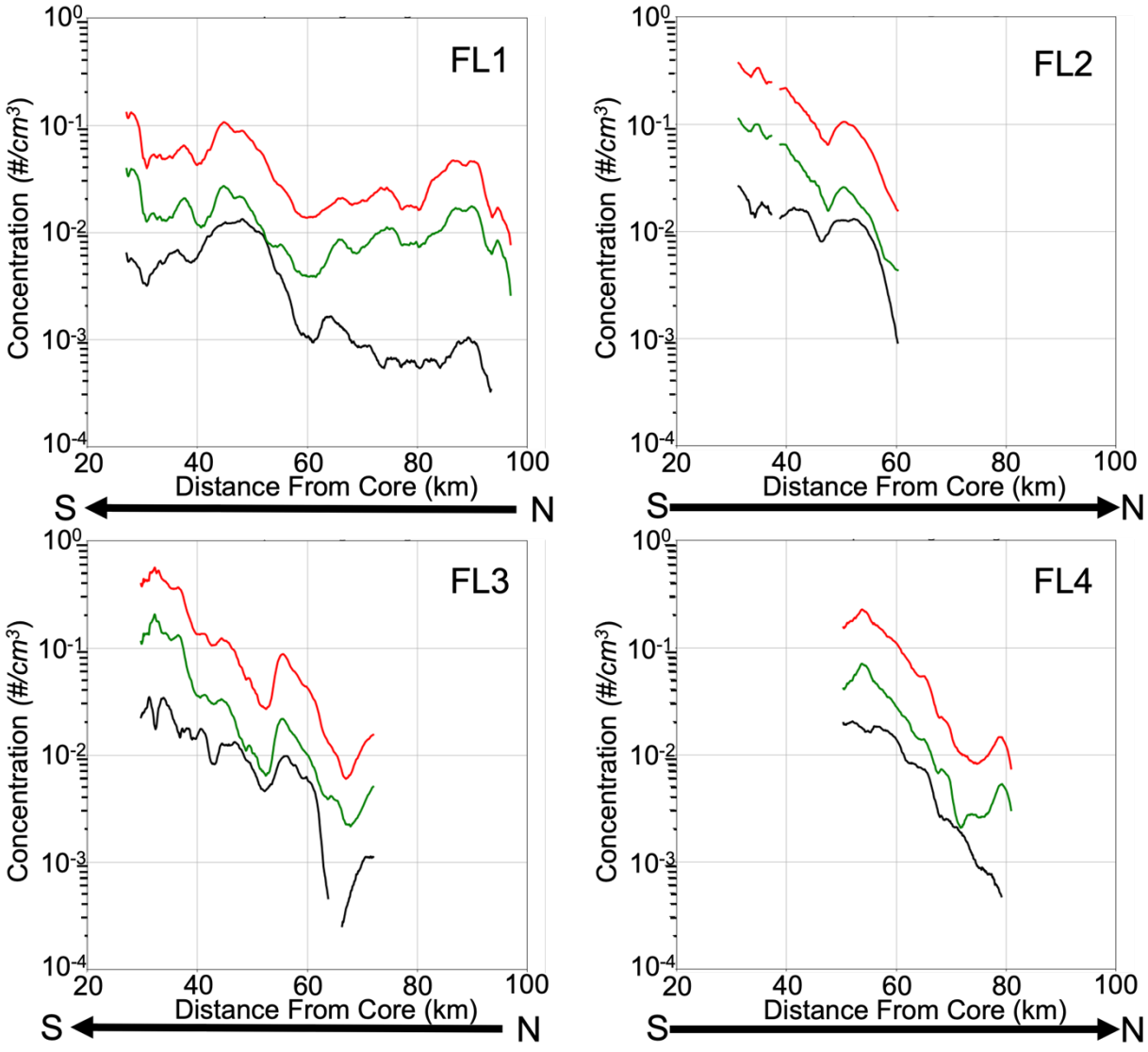

Figure 15. Four panel plot showing the 20-point moving averages for the chain aggregate (black), non–chain aggregate (green), and the total (red) particle number concentrations versus distance from the TITAN cell's core. Underneath each corner plot, a black arrow depicts the direction the aircraft was flying going forward in time.

FL2-4 are similar to each other where the concentrations of the chain aggregates decrease with increasing distance from the TITAN cell's core. Moreover, it is clear that the convergence between the chain and non-chain aggregate concentrations is due to the non-chain aggregate concentration decreasing at a faster rate than the chain aggregate concentration. FL1 is the most dissimilar than the other flight legs where from 28 to 53 km from the TITAN cell's core, the concentration of non-chain aggregates decreases slightly while the concentration of chain aggregates increases.

The areas of convergence (and divergence) are visualized in Figure 16, where the ratio between the concentration of chain aggregates and the concentration of non-chain aggregates are depicted. This ratio is defined as the relative chain aggregate concentration with respect to the non-chain aggregate concentration ($RCAC_{N-C}$) where above 0.5 (1:2 ratio) is deemed as high. The peaks in $RCAC_{N-C}$ indicates the points where the chain and non-chain aggregate concentrations converge (as seen in Figure 15). When the $RCAC_{N-C}$ is below 0.5, this indicates where the chain and non-chain aggregate concentrations are not similar; in this case, higher concentrations of non-chain aggregates relative to chain aggregates. For all of the flight legs, the $RCAC_{N-C}$ is lower while closer to the TITAN cell's core and increases up to a certain distance before quickly dropping off.

It is also important to note the periodicities observed in the $RCAC_{N-C}$. These periodicities are observed in all of the flight legs, though, the distances between the crests and troughs vary between flight legs. No other in-situ microphysical measurements appears to have similar periodicities. Due to the $RCAC_{N-C}$ being an intrinsic parameter, it would be reasonable to compare to other remotely observable intrinsic parameters.

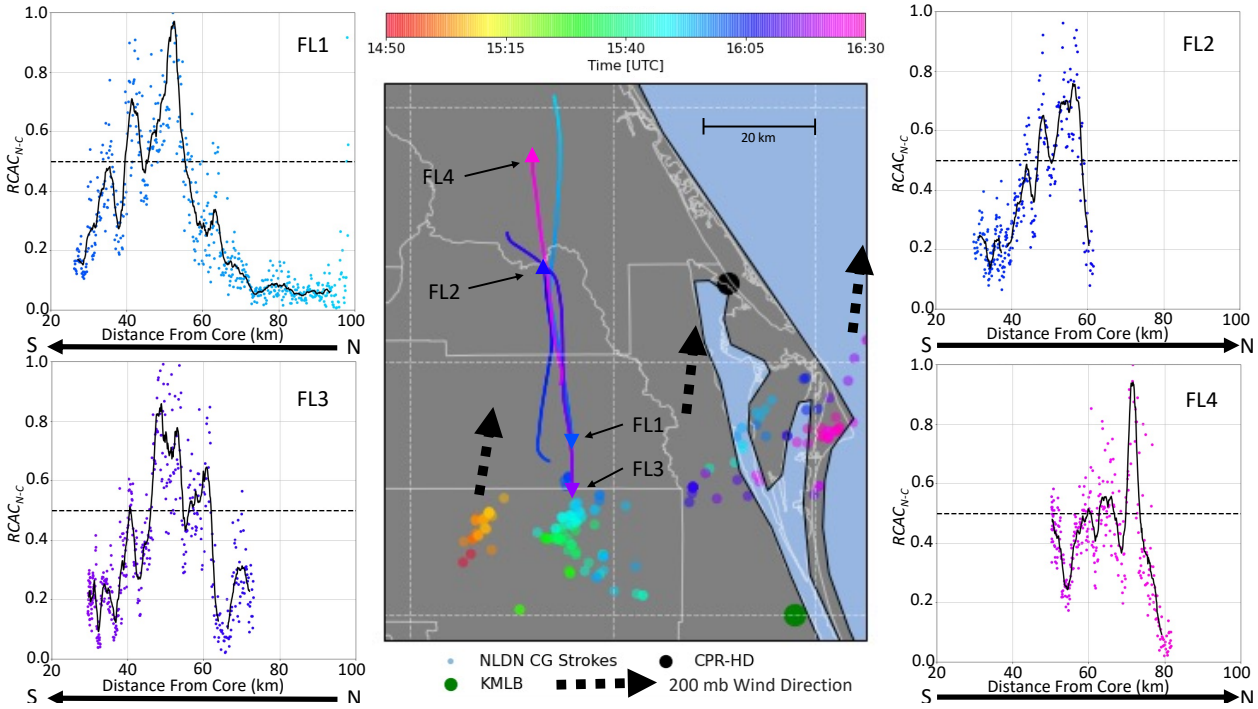

Figure 16. The four corner plots depict the 1 Hz Relative Chain Aggregate Concentration with respect to Non-Chains ($RCAC_{N-C}$) data per flight leg with respect to distance from the TITAN cell's core with an overlaid 20-point centered moving average (black). Underneath each corner plot, a black arrow depicts the direction the aircraft was flying going forward in time. The black dotted line indicates the 0.5 value in the $RCAC_{N-C}$ where anything above 0.5 is high. The center plot shows the locations of each flight leg as well as the locations of the National Lightning Detection Network (NLDN) cloud-to-ground lightning strokes. The color scale represents time for the data shown in each plot. Larger circles on the center plot depict important locations relevant to this work. The black arrows (dashed) overlaid on the center plot represent the 200 mb wind direction as obtained from the radiosonde profile from Cape Canaveral, Florida, at 15:00 UTC (Figure 8).

Electrical Observations (In-situ and Remote Sensed)

The six rotating-vane electric field mills on the North Dakota Citation II Research Aircraft measures the electric field during the flight legs on the 3 August 2019 first flight. All flight legs have electric field magnitude (E_{mag}) on the order of 10^1 kV m^{-1} (Table 6). The electric fields are largest when the aircraft is in relatively close proximity to the TITAN cell's core (Figure 17), which is reasonable due to the aircraft being closer to the more active lightning region of the storm. When near the reflectivity core, the vertical electric field (E_z) is mainly on the order of 10^0 kV m^{-1}. There is a strong E_z increase at the end of FL1 (E_z peaked at -22.37 kV m^{-1}) that is an order of

magnitude higher than the typical cirrus cloud E_z. This increase in E_z is likely due to the aircraft entering a relatively high electric field charge region and not caused by lightning. The temporal span of the peak is on the order of seconds, while electric discharges are on the order of micro-seconds (Rakov 2016). Additionally, the diverging electric field vectors indicate this peak is caused by the aircraft entering a high electric field region (Figure 18).

Assuming a typical bi-polar storm structure, the LMA recorded lightning strikes between 15:40:00 to 16:00:00 UTC which show the lower negative charge region is mainly situated around 5-6 km AGL and the upper positive charge regions fluctuates between approximately 8-12 km AGL (Figure 19). The closest lightning event to the FL1 electric field peak occurred at approximately 16:01:43 UTC (Figure 20), which has similar charge regions as Figure 19 and an extent of approximately 20 km. This lightning event occurred over a minute after the maximum in FL1 electric field detected, which indicates that it is not associated with the measured peak. Hence, the measurements (Figure 18-20) support the conclusion that the larger electric fields close to the TITAN cell's core is due to more bi-polar charge difference near the core than further way. The in-situ electric field magnitudes for the flight legs are similar in magnitude to what was used in cloud chamber experiments performed by Saunders and Wahab (1975). However, in the cloud chamber experiments, chain aggregates were only generated while using electric fields greater than or equal to 60 kV m^{-1}.

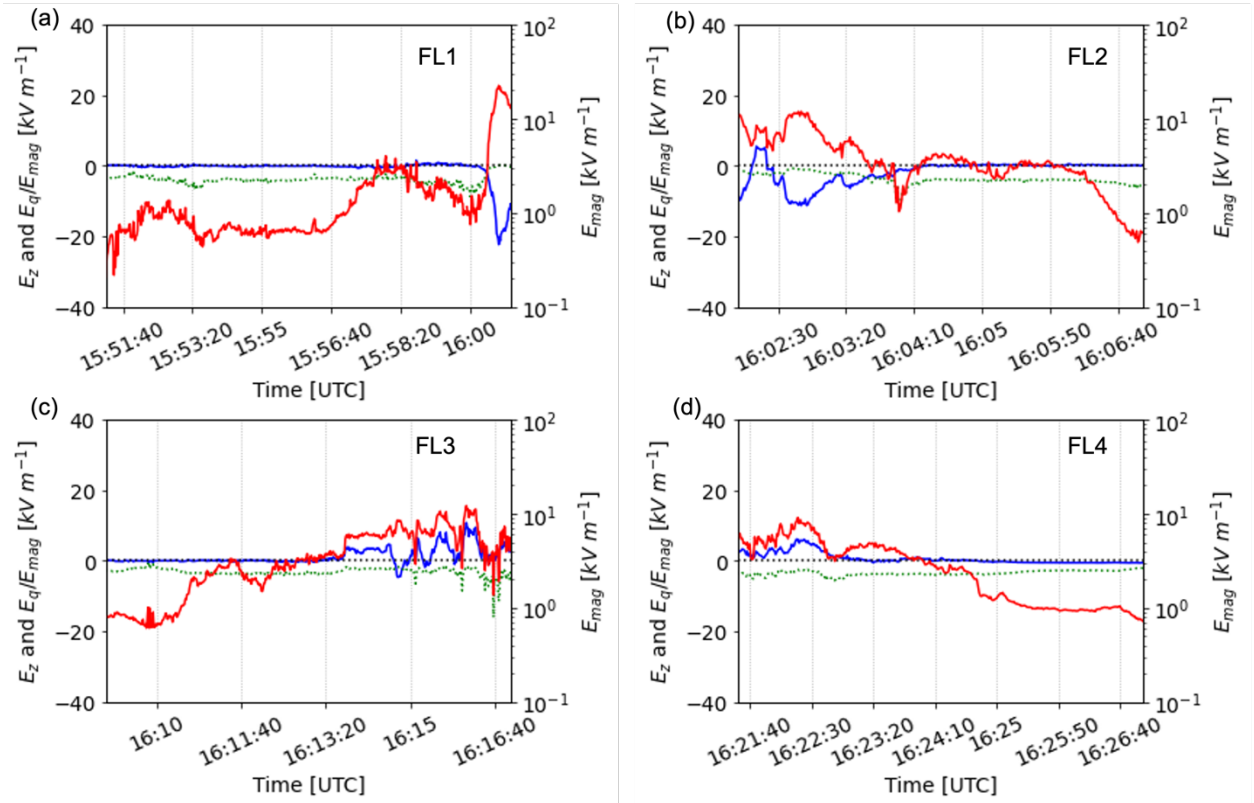

Figure 17. Four panel plot showing the electric field measured by 6-rotating vane electric field mills on the North Dakota Citation II Research Aircraft. The solid blue line indicates the vertical electric field (E_z), the dotted green line indicates the static charge on the aircraft (E_q) divided by the absolute value of the total electric field magnitude (E_{mag}), and the solid red line indicates the absolute value of the total electric field magnitude (E_{mag}). The dotted black line indicates 0 kV m^{-1} on the left y-axis.

Table 6. In-situ electric field mill data statistics for each flight leg during the 3 August 2019 first flight. The units for electric field data provided is in kV m^{-1}.

Legs	Time [UTC]	E_x – Mean [Min, Max]	E_y – Mean [Min, Max]	E_z – Mean [Min, Max]
FL1	15:51:15 – 16:01:00	-0.89 [-4.01, 017]	0.93 [-0.16, 8.04]	-0.87 [-22.37, 1.50]
FL2	16:02:00 – 16:07:00	-1.96 [-5.63, 1.52]	0.78 [-4.93, 6.42]	-1.76 [-11.22, 5.53]
FL3	16:09:00 – 16:17:00	-2.95 [-6.59, -0.21]	1.05 [-3.43, 6.67]	1.15 [-4.70, 10.80]
FL4	16:21:30 – 16:27:00	-2.36 [-4.86, -0.40]	-0.11 [-5.86, 4.28]	0.68 [-0.58, 6.15]

(a)

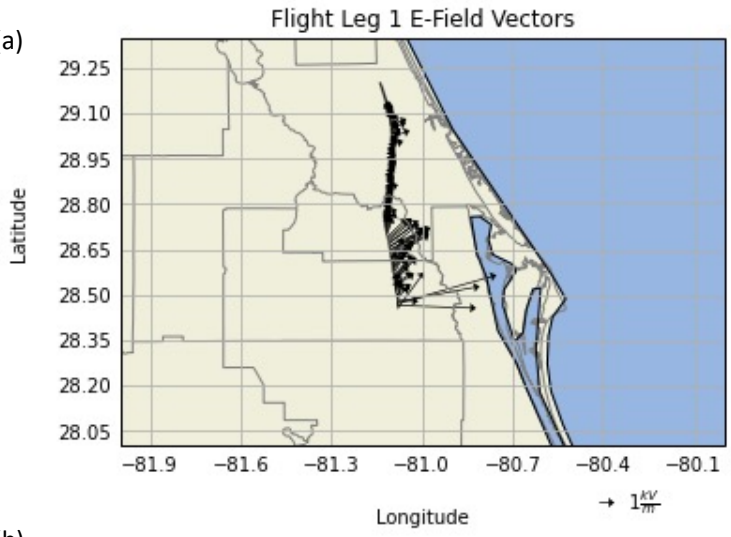
Flight Leg 1 E-Field Vectors
Latitude
29.25
29.10
28.95
28.80
28.65
28.50
28.35
28.20
28.05
−81.9
−81.6
−81.3
−81.0
−80.7
−80.4
−80.1
Longitude
→ 1 kV/m

(b)

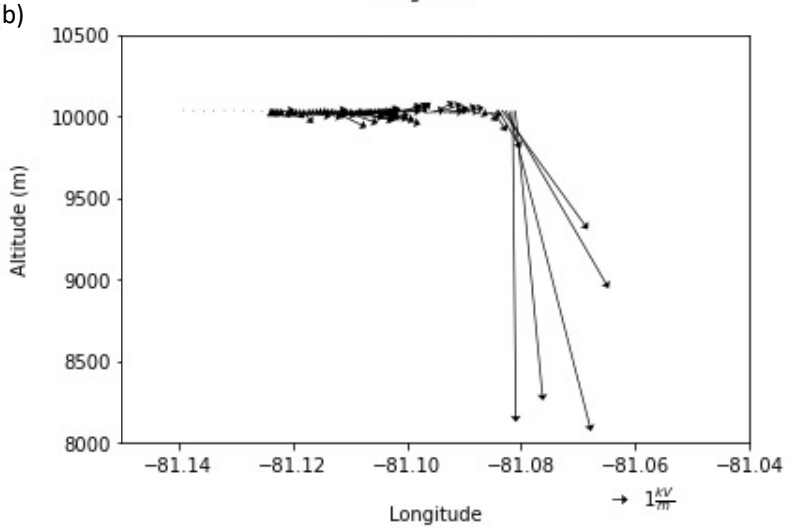
Altitude (m)
10500
10000
9500
9000
8500
8000
−81.14
−81.12
−81.10
−81.08
−81.06
−81.04
Longitude
→ 1 kV/m

(c)

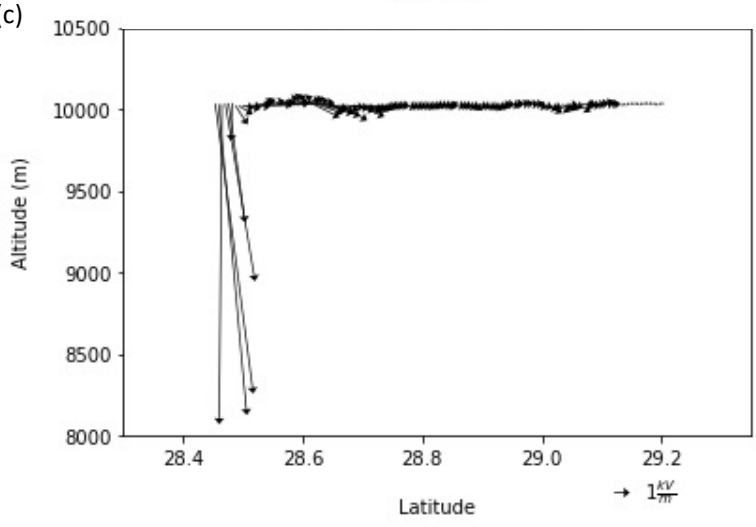
Altitude (m)
10500
10000
9500
9000
8500
8000
28.4
28.6
28.8
29.0
29.2
Latitude
→ 1 kV/m

Figure 18. Electric field vectors for flight leg 1 (FL1) during the 3 August 2019 research flight. Each panel depicts the vectors (E_{mag}) with a different orientation; panel (a) is a plan view (x, y); panel (b) is a vertical view (x, z); panel (c) is a vertical view (y, z).

(a)

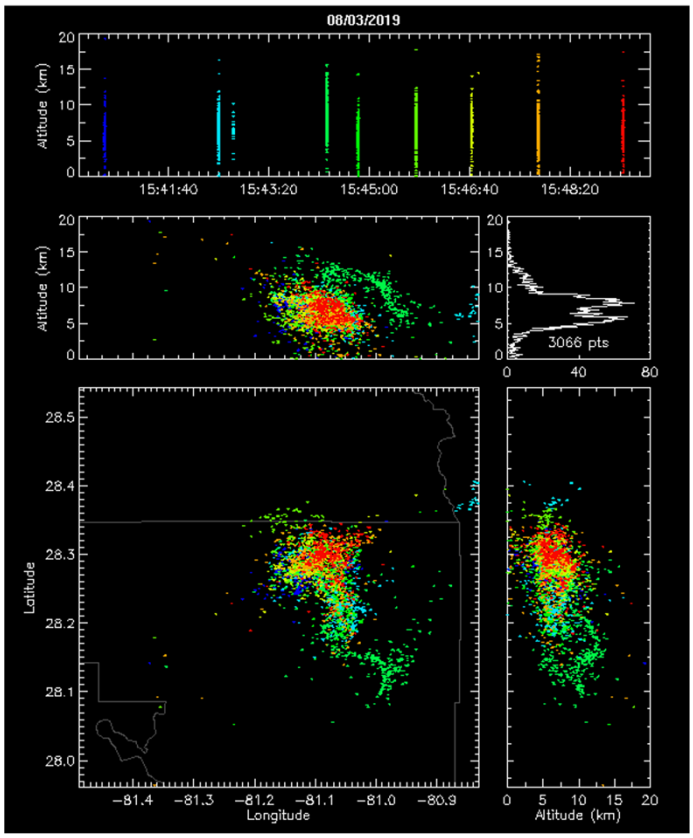
08/03/2019
Altitude (km)
15:41:40
15:43:20
15:45:00
15:46:40
15:48:20
3066 pts
Latitude
Longitude
Altitude (km)

(b)

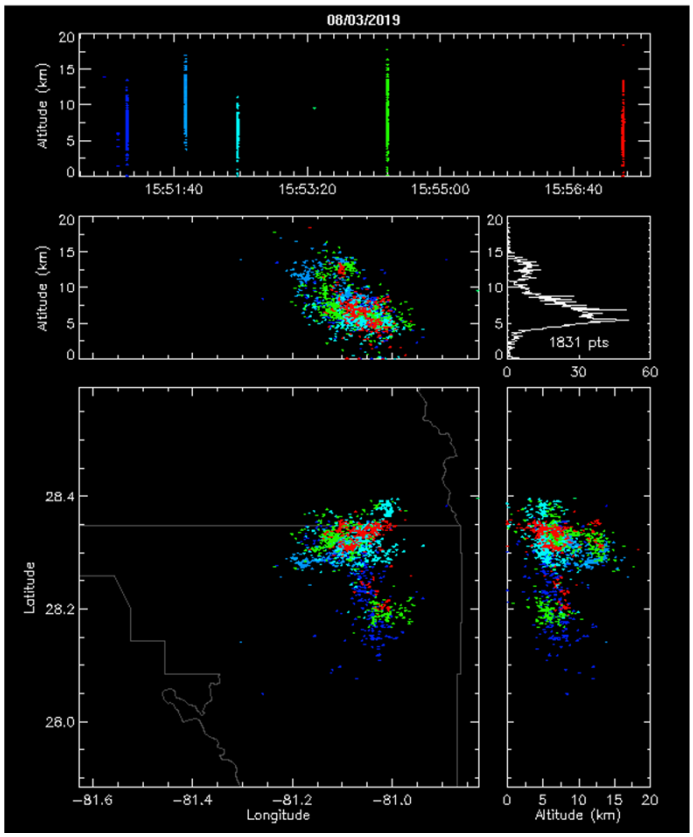
08/03/2019
Altitude (km)
15:51:40
15:53:20
15:55:00
15:56:40
1831 pts
Latitude
Longitude
Altitude (km)

Figure 19. The Kennedy Space Center Lightning Mapping Array data (KSCLMA) showing (a) the lightning activity from 15:40:00 to 15:50:00 UTC and (b) from 15:50:00 to 16:00:00 UTC. The lightning mapping data shown is only from the enhanced convective cell (which was initiated at 15:10:00 UTC). The color scale of the points are based on the time those points were measured by the lightning mapping array. Each lightning strike is displayed in a different color range.

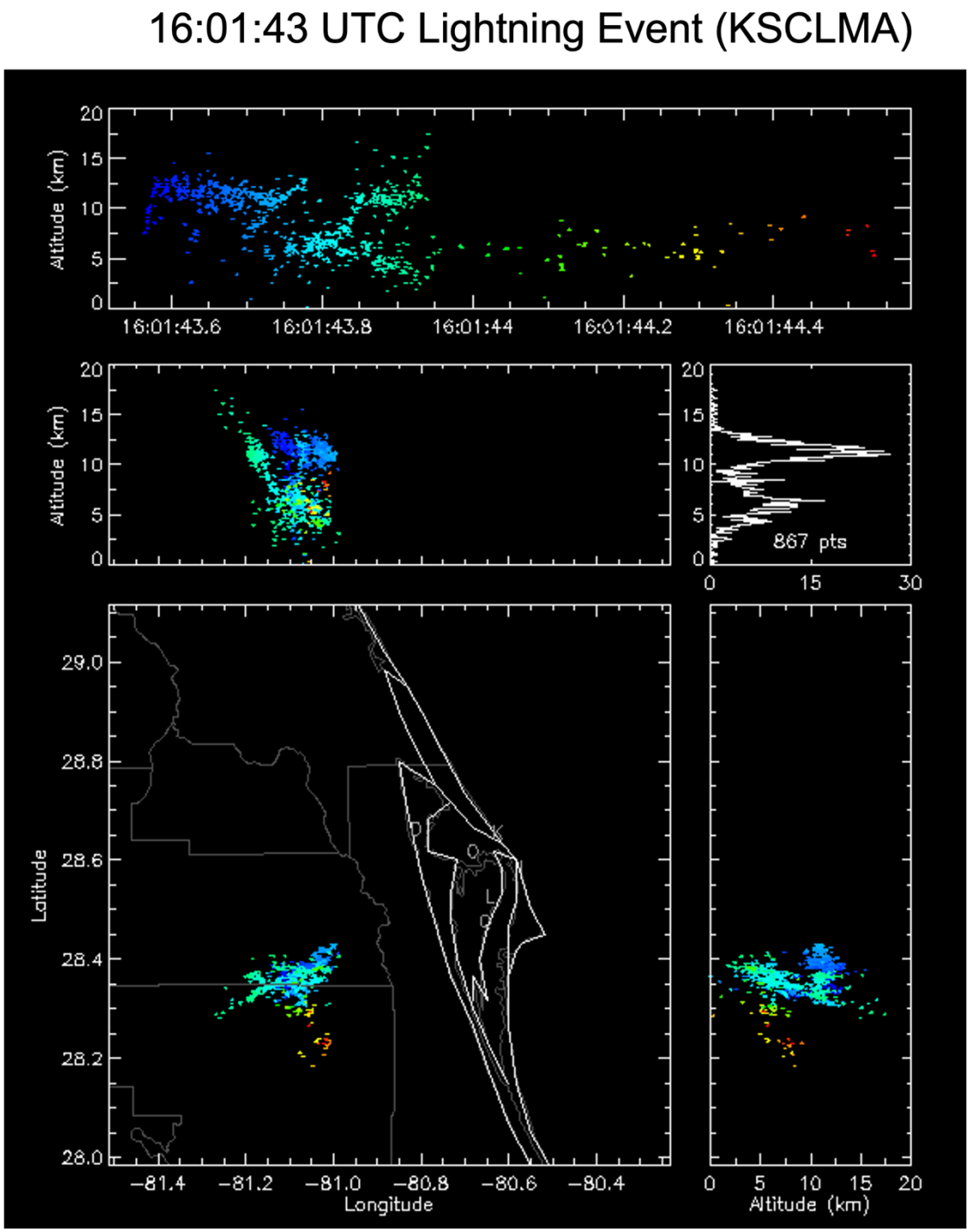

Figure 20. Lightning Mapping Array data from the Kennedy Space Center (KSCLMA) showing the lightning event that occurred just after FL1 and before FL2 within the TITAN cell at 16:01:43 UTC. The color scale of the points are based on the time those points were measured by the lightning mapping array.

Radar and Satellite

Radar data is utilized in order to put the in-situ microphysical observations into context. However, the various limitations of the KMLB radar hinders the ability to put the in-situ microphysical observations into context (see Appendix D). The KMLB radar is not sensitive enough to measure more dilute areas of the sampled cirrus cloud anvil. Also, the KMLB radar measurements are not concurrent with the aircraft in-situ observations. Thus, a more sensitive radar that has the ability to track the aircraft in real time is necessary to further interpret the in-situ microphysical data. The CPR-HD radar tracked the aircraft on 3 August 2019 and is utilized to put the in-situ microphysical observations into context for FL1 and FL4. Prior to approximately 15:57:05 UTC, it is clear that the North Dakota Citation II Research Aircraft was sampling cirrus anvil clouds produced from earlier convection based on the reflectivity gradient (Figure 21). Evidence from the satellite imagery (Figure 22) also indicates the aircraft sampled cirrus anvil clouds produced from earlier convection. After 15:57:05 UTC, the North Dakota Citation II Research Aircraft began sampling the cirrus anvil region associated with the TITAN cell. Not only is this transition between the old and new cirrus anvil observed in the radar data but is it also observed in the increase in TWC (Figure 10). The aircraft traversed two areas of reflectivity maximums while heading towards the TITAN cell's core at approximately 15:58:00 UTC and 15:58:30 UTC (~ 20 dBZ) before the end of the CPR-HD radar scan. Comparing Figure 9a and Figure 22, it is clear that the reflectivity higher above the aircraft towards the end of the CPR-HD scan is associated with the outer edge of the overshooting-top associated with the TITAN cell.

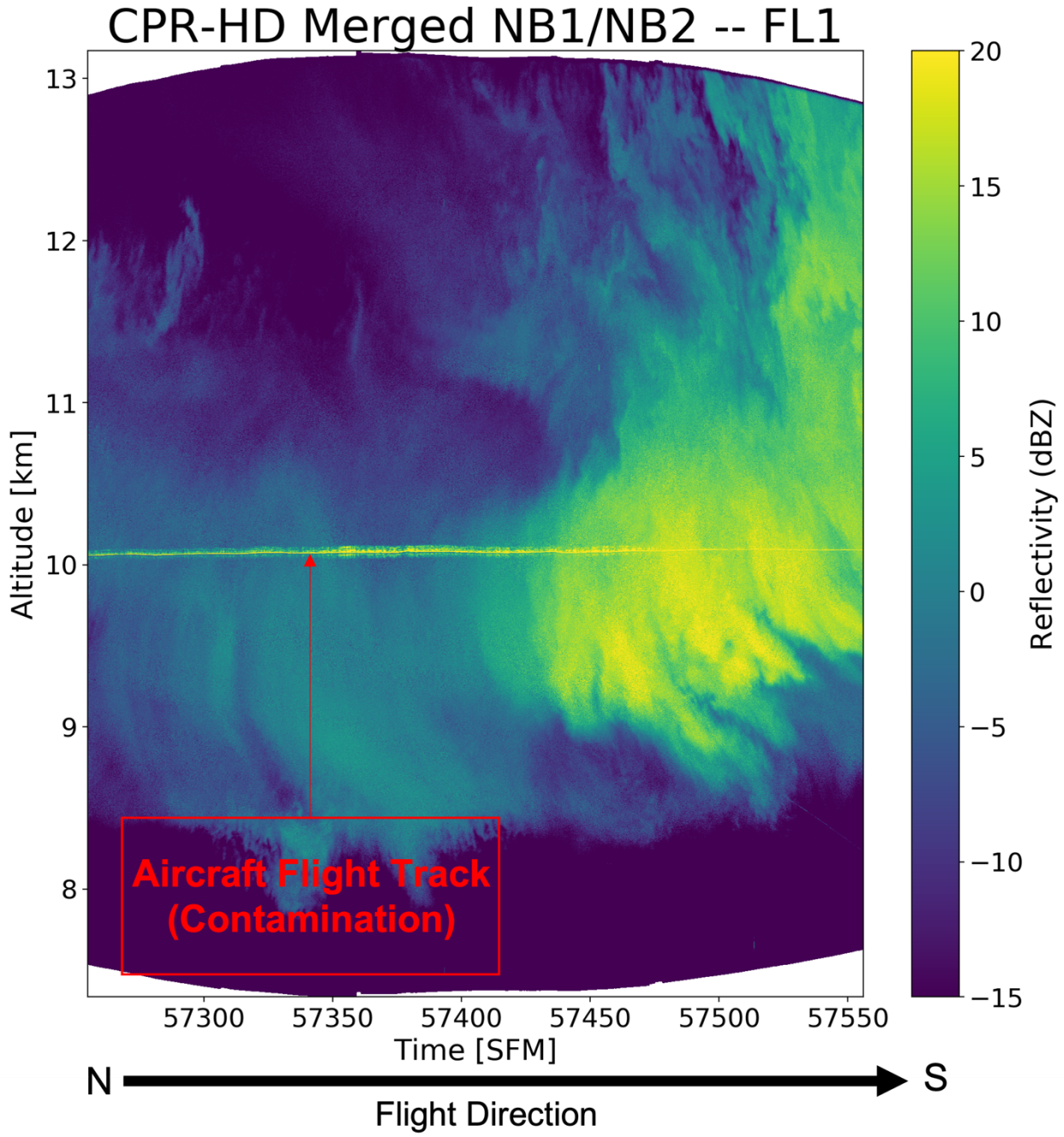
CPR-HD Merged NB1/NB2 -- FL1
Altitude [km]
13
12
11
10
9
8
57300
57350
57400
57450
57500
57550
Time [SFM]
Reflectivity (dBZ)
20
15
10
5
0
−5
−10
−15
Aircraft Flight Track
(Contamination)
N
S
Flight Direction

Figure 21. Graphic depicting the radar reflectivity factor (shading) from the two narrow band windows of the CPR-HD for a flight segment of FL1 (between 15:53:55 and 15:59:16 UTC). The 'stripe' of high reflectivity factor at approximately 10 km is the aircraft induced contamination. The black arrow indicated the aircraft direction of flight. Altitude of the beam at each range gate (y-axis) is derived using methods described in Gapp *et al.* 2019.

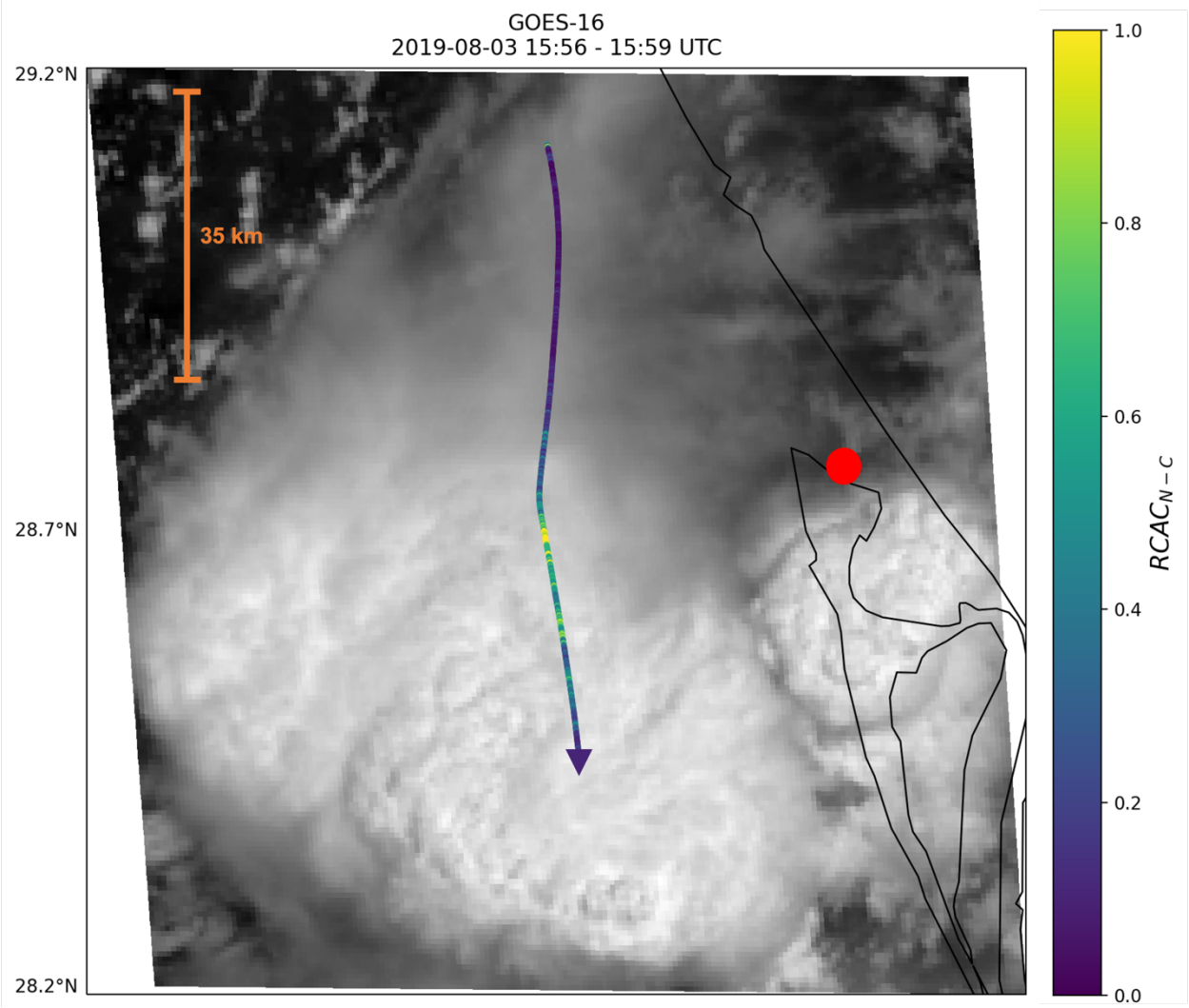

Figure 22. Visible (red – channel 2) satellite imagery from the Geostationary Operational Environmental Satellite (GOES-16) showing the cloud structures west of Cape Canaveral, Florida on 3 August 2019. Depicted satellite coordinate limits - Latitude: [28.2 °N; 29.2 °N]; Longitude: [-82.2 °W; -80 °W]. Overlaid is the aircraft track for FL1 that is colored based on values of $RCAC_{N-C}$. The red circle indicates the location of the CPR-HD radar.

There is an increase in both non-chain aggregate and the chain aggregate number concentrations when the aircraft enters into the higher reflectivity areas heading towards the TITAN cell's core (Figure 23). The maximum in the $RCAC_{N-C}$ (0.97) occurs at 15:57:19 UTC

when the aircraft enters the very outer edge of the cirrus anvil associated with the TITAN cell, which occurs approximately 53 km from the TITAN cell's core. Moreover, there is a secondary peak in the $RCAC_{N-C}$ (0.71) when the aircraft passed through the second reflectivity maximum approximately 41 km from the core. Interestingly, after the maximum in the $RCAC_{N-C}$, the $RCAC_{N-C}$ decreases without any increases that surpass the peak at 15:57:19 UTC for the rest of the flight leg; even while being closer in proximity to the core.

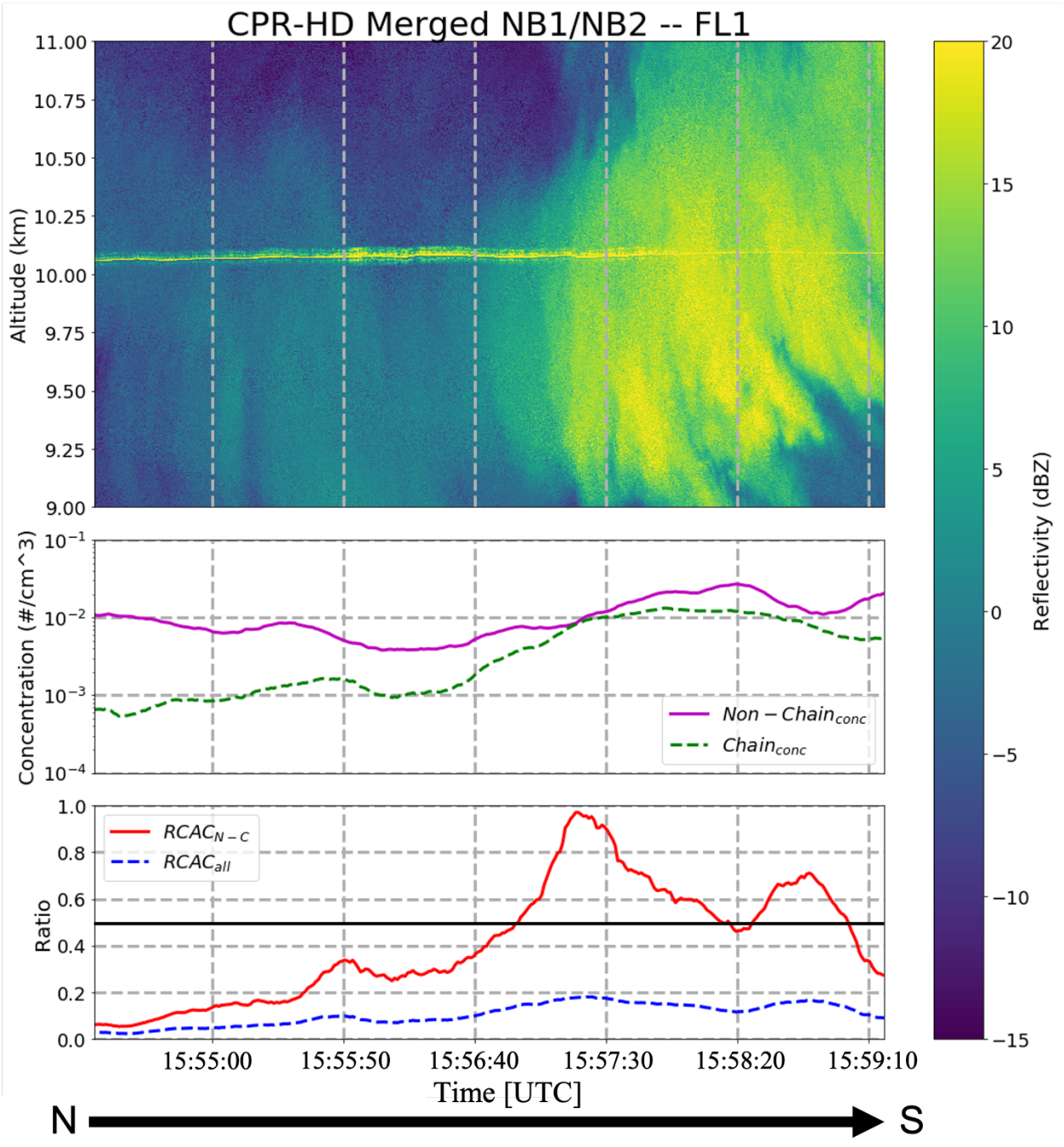
CPR-HD Merged NB1/NB2 -- FL1
Altitude (km)
11.00
10.75
10.50
10.25
10.00
9.75
9.50
9.25
9.00
Concentration (#/cm^3)
10^{-1}
10^{-2}
10^{-3}
10^{-4}
$Non-Chain_{conc}$
$Chain_{conc}$
Ratio
1.0
0.8
0.6
0.4
0.2
0.0
$RCAC_{N-C}$
$RCAC_{all}$
15:55:00
15:55:50
15:56:40
15:57:30
15:58:20
15:59:10
Time [UTC]
N
S
Reflectivity (dBZ)
20
15
10
5
0
−5
−10
−15

Figure 23. Plots showing the CPR-HD radar reflectivity (dBZ [top]), particle concentrations for both the non-chain (purple – solid) and chain aggregate (green – dashed) concentrations (middle), and the ratio of chains to non-chains ($RCAC_{N\text{-}C}$ [red – solid]) and the ratio of chains to the total particle concentration ($RCAC_{all}$ [blue – dotted; bottom]) for times between 15:53:55 and 15:59:16 UTC during FL1. The top radar plot is subset to between 9 and 11 km in the vertical. The black arrow is depicting the aircraft flight track and contamination as the CPR-HD was following the aircraft. The black solid line for the bottom plot indicates the 0.5 level where any value above 0.5 is considered high. The black arrow indicated the direction in which the aircraft was flying.

During FL4, the aircraft samples the cirrus anvil associated with the TITAN cell similar to FL1 (Figure 24), though as time progresses, the convection deteriorates (Figure 9d), and the cloud tops become more diffuse (Figure 25). At 16:21:30 UTC, the aircraft samples underneath the outer edge of the diffuse overshooting top. Similar to FL1, during FL4 the aircraft traverses through two reflectivity maximums; one between 16:21:30 and 16:22:20 UTC, and the second between 16:23:05 and 16:23:30 UTC. Between 16:23:30 and 16:25:25 UTC, the aircraft samples regions of lower reflectivity while heading father away from the deteriorating core. For the most part, the higher concentrations of chain aggregates correspond to higher reflectivity regions. It is important to note the small scale variability in reflectivity, as well as possible indications of gravity waves at the cloud tops.

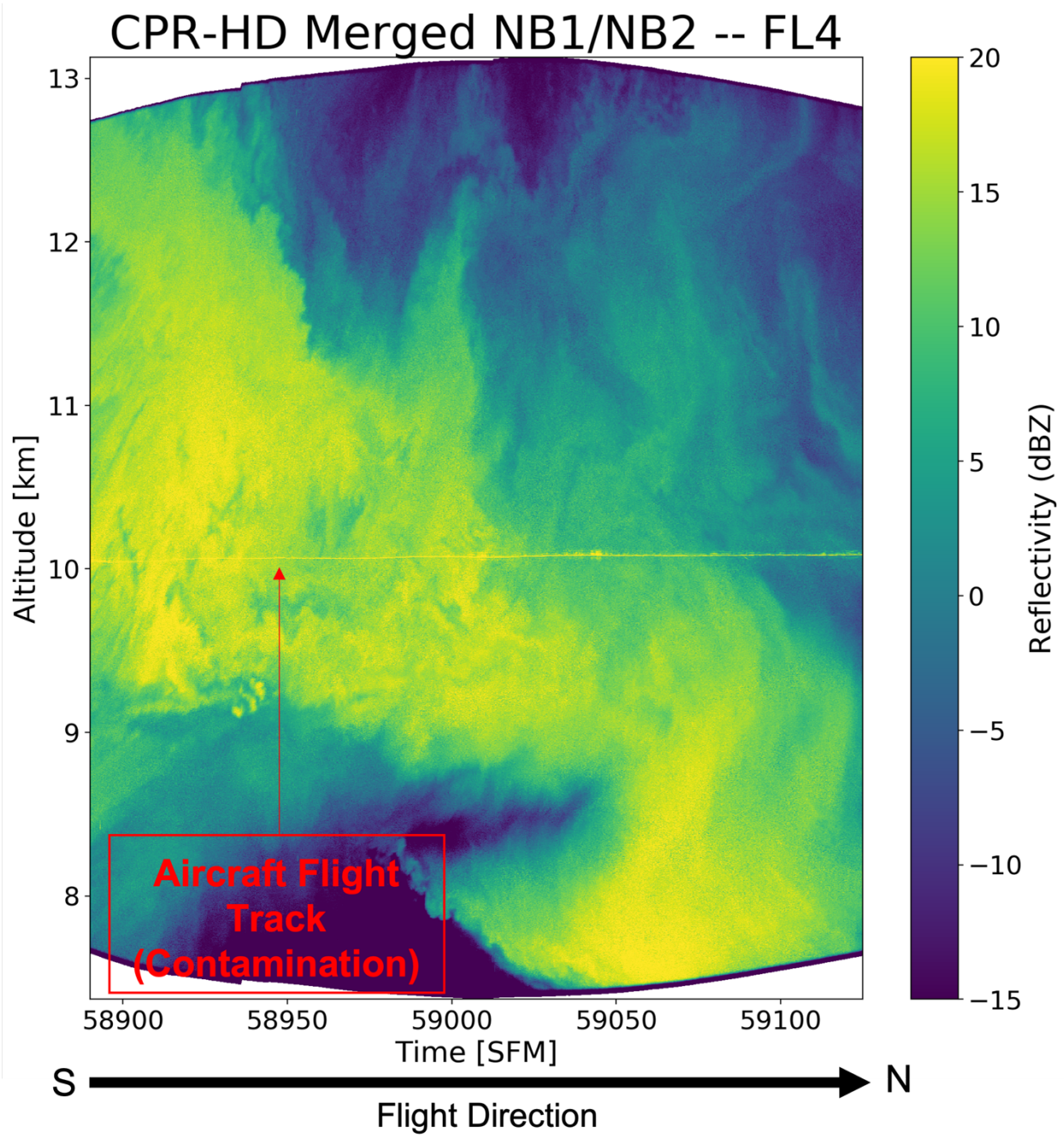
CPR-HD Merged NB1/NB2 -- FL4
Altitude [km]
13
12
11
10
9
8
58900
58950
59000
59050
59100
Time [SFM]
Aircraft Flight Track (Contamination)
S
N
Flight Direction
Reflectivity (dBZ)
20
15
10
5
0
−5
−10
−15

Figure 24. Graphic depicting the radar reflectivity factor (shading) from the two narrow band windows of the CPR-HD for a flight segment of FL4 (between 16:21:30 and 16:25:25 UTC). The 'stripe' of high reflectivity factor at approximately 10 km is the aircraft induced contamination. The black arrow indicated the aircraft direction of flight. Altitude of the beam at each range gate (y-axis) is derived using methods described in Gapp *et al.* 2019.

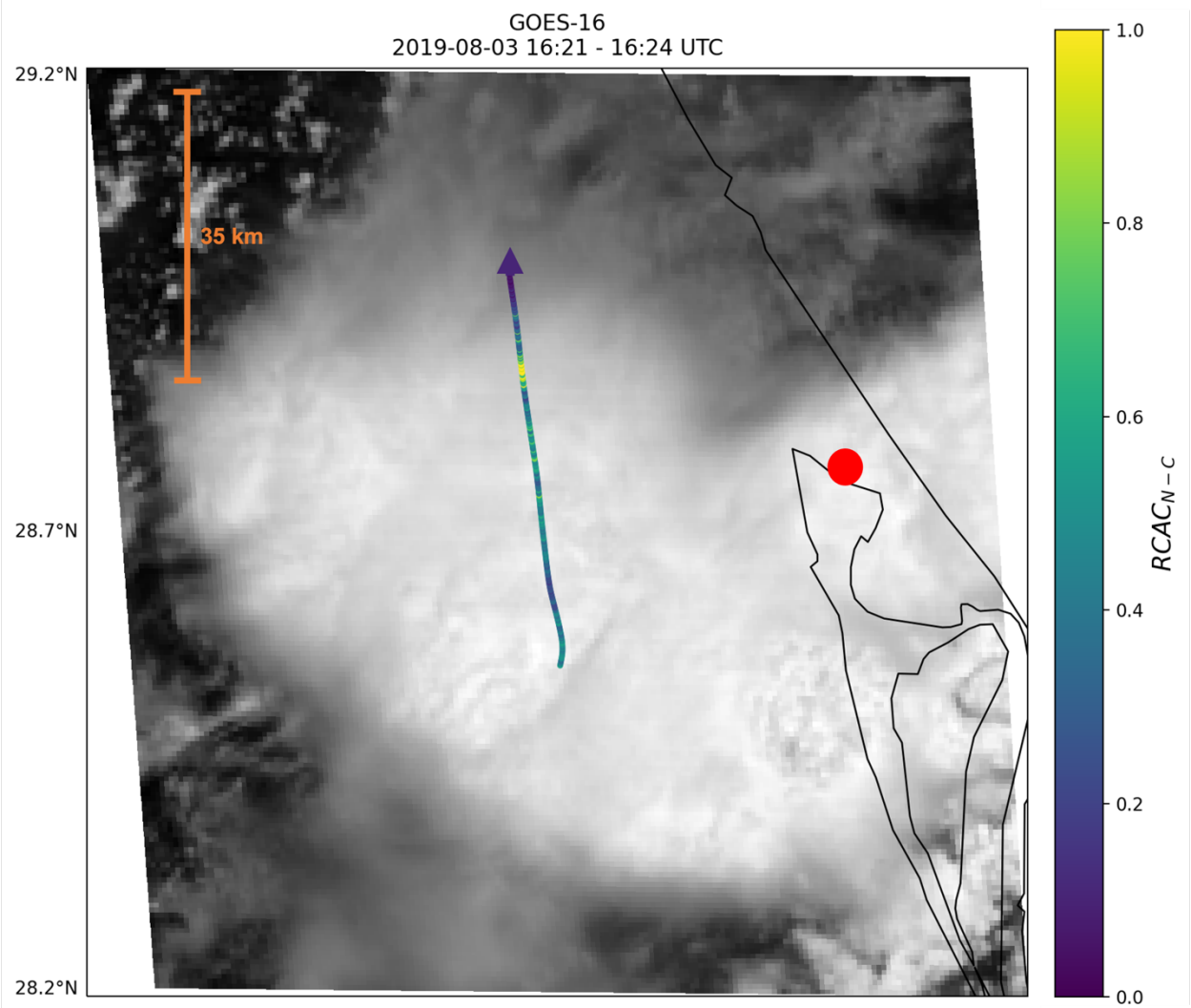

Figure 25. Visible (red, channel 2) satellite imagery from the Geostationary Operational Environmental Satellite (GOES-16) showing the cloud structures west of Cape Canaveral, Florida on 3 August 2019. Depicted satellite coordinate limits - Latitude: [28.2 °N; 29.2 °N]; Longitude: [-82.2 °W; -80 °W]. Overlaid is the aircraft track for FL4 that is colored based on values of $RCAC_{N-C}$. The red circle indicates the location of the CPR-HD radar.

Comparisons of the concurrent observations between the CPR-HD and the in-situ microphysical data for the 5.5-minute scanning period during FL4 is displayed in Figure 26. Both the chain and non-chain aggregate concentrations mainly decrease heading away from the TITAN

cell's core. On average, during the 5.5-minute scanning period, the $RCAC_{N-C}$ increases heading away from the core. The maximum in $RCAC_{N-C}$ (0.94) occurs at the very end of the scanning period at 16:25:25 UTC at approximately 71 km away from the core near the more diffuse, outer edge of the cirrus anvil region.

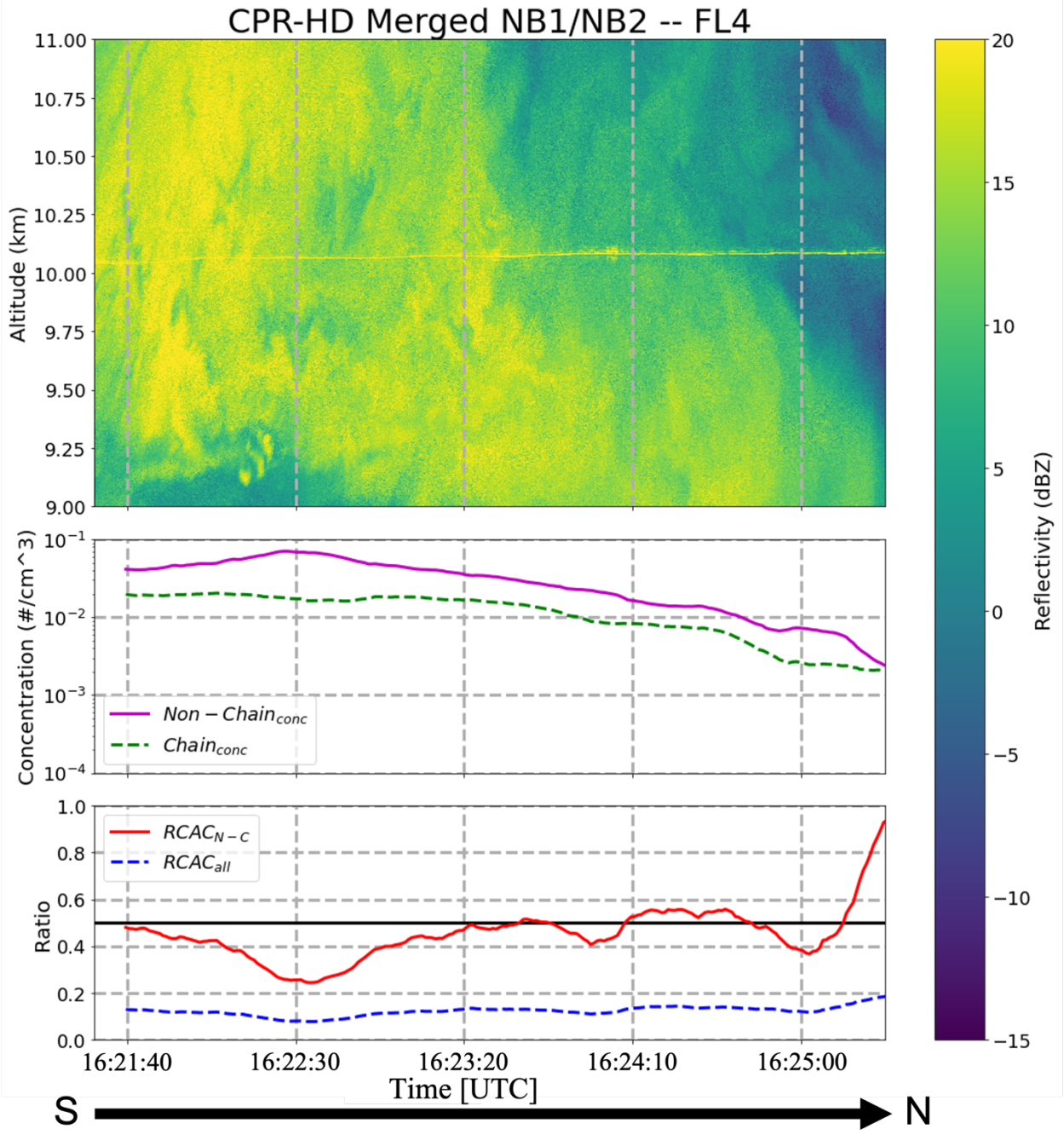

Figure 26. Plots showing the CPR-HD radar reflectivity (top), particle concentrations for both the non – chain (purple – solid) and chain aggregate (green – dashed) concentrations (middle), and the ratio of chains to non – chains ($RCAC_{N\text{-}C}$ [red – solid]) and the ratio of chains to the total particle concentration ($RCAC_{all}$ [blue – dotted; bottom]) for times between 16:21:30-16:25:25 UTC during FL4. The top radar plot is subset to between 9 and 11 km in the vertical. The black arrow is depicting the aircraft flight track and contamination as the CPR-HD was following the aircraft. The black solid line for the bottom plot indicates the 0.5 level where any value above 0.5 is considered high.

The chain aggregate and non-chain aggregate concentrations at the locations of the $RCAC_{N\text{-}C}$ maximums differ between FL1 and FL4. During FL1, the $RCAC_{N\text{-}C}$ maximum occurs when there is an increase in both the chain and non-chain aggregate concentrations. Between 15:56:40 and 15:57:19 UTC, the increase in the chain aggregate concentration is more rapid than the non-chain aggregate concentration allowing the two concentrations to converge; resulting in the $RCAC_{N\text{-}C}$ being close to 1. Conversely, during FL4, the $RCAC_{N\text{-}C}$ maximum occurs when there is a decrease in both the chain and non-chain aggregate concentrations. Between 16:25:00 and 16:25:25 UTC, the chain aggregate concentration decreases less rapidly than the non-chain aggregate concentration allowing the two concentrations to converge; resulting in the $RCAC_{N\text{-}C}$ being close to 1.

CHAPTER V

SUMMARY AND DISCUSSION

Chain aggregates in the convection-induced, cirrus anvil regions of Florida thunderstorms on the 3 August 2019 are complex. The PHIPS probe high-resolution, stereographic images show chain aggregates vary in size, orientation, number of particles, and particle habits. The imaged chain aggregates show various similarities to cloud chamber and previous airborne experiments. Similarities from the airborne experiments include the elongated structure of the chains, the individual crystal types associated, the small joint-like features connecting the individual particles, and the temperature/altitude region in the thunderstorm where the chain aggregates are located. Moreover, as in previous airborne experiments, majority of the chain aggregates are not rimed, which suggest that chain aggregates may form at higher altitudes within the thunderstorm where there are lower concentrations of super-cooled liquid water. The observed chain aggregates are similar to chain aggregates in cloud chamber experiments as both have elongated structure with individual crystals (plates and columns). The cloud chamber experiments indicate the maximum aggregation efficiency is at -8 °C with an electric field strength of 200 kV m^{-1} and particle concentrations much higher than what is typically observed in the real atmosphere (Saunders and Wahab, 1975). At the -8 °C level in typical Florida thunderstorms the relatively high concentrations of super-cooled liquid water would lead to riming of the aggregates. Rimed chain aggregates have been observed in continental convection at -8 °C (Stith *et al*. 2004). Rimed ice is present on few of the chain aggregates observed on the 3 August 2019 research flight (approximately 10% of the total number of chain aggregates). It is possible that higher

concentrations of rimed chain aggregates are present closer to the TITAN cell's core so other CapeEx19 flight days have to be analyzed to fully address riming of chain aggregates.

Cloud chamber experiments indicate electric fields play a crucial role in the chain aggregation process and that 60 kV m^{-1} is the minimum electric field to have an impact on aggregation. These high electric fields increase collisions and adhesion of ice particles (Saunders and Wahab, 1975). The electric field on 3 August 2019 first flight never reach 60 kV m^{-1}, having a maximum of 22 kV m^{-1} (Figure 17). Additionally, most of the flight had the electric field between 1.0 x 10^0 and 1.0 x 10^1 kV m^{-1}. Other airborne experiments that sampled in convection-induced, cirrus anvils and observed chain aggregates had electric field on the same order of magnitude (Dye *et al.* 2007). If the electric field does not need to be 60 kV m^{-1} at cold temperatures to enhance chain aggregates, it is possible that chain aggregation can occur within the cirrus anvil region.

14 percent of the PHIPS particle images are classified as chain aggregates throughout FL1-4 (Table 3). 83 percent of particles with a diameter greater than 495 μm (Table 5) are chain aggregates at a moderate-to-high confidence level during FL1-4. The CIP particle concentrations greater than 495 μm provides an assessment of the chain aggregate concentration. Regarding the particle concentrations observed during the 3 August 2019 first flight, the chain, non-chain, and total particle number concentrations decrease as the aircraft is further away from the TITAN cell's reflectivity centroid (except for FL1). The CPR-HD shows enhanced reflectivity in the regions where the highest concentrations of chain aggregates are found for FL1 and FL4 (Figure 23, Figure 26). For FL1-4, the distance from the TITAN cell's reflectivity centroid where the chain and non-chain aggregate concentrations converge varies. The relative chain aggregate concentration with respect to the non-chain aggregate concentration ($RCAC_{N-C}$) highlights the areas of convergence between the chain aggregate and non-chain aggregate concentrations. The maximums in the

$RCAC_{N-C}$ for all flight legs are greater than 0.8. The maximums in the $RCAC_{N-C}$ do not appear to be at the closest point to the TITAN cell's core, but rather tens of kilometers away (to the north northeast) from the core. The concurrent CPR-HD observations allow for a visual representation of where the high values in $RCAC_{N-C}$ are observed in the storm for FL1 and FL4. Interestingly, the peak in $RCAC_{N-C}$ for FL1 is not within a maximum reflectivity region but just on the outer edge of the cirrus anvil produced from the TITAN cell. After the peak in the $RCAC_{N-C}$, as the aircraft samples closer to the TITAN cell's reflectivity centroid, the trends in $RCAC_{N-C}$ decreases to the end of the flight leg but in regions of higher reflectivity (Figure 23).

Particle concentrations observed during FL2-4 are different to what is observed in FL1 where the ratio ($RCAC_{N-C}$) increases with increasing distance from the TITAN cell's core; where at the same time, the total particle number concentration and the concentration of chain aggregates decrease. This implies that more of the smaller particles are possibly sublimating and/or the smaller particles are aggregating into larger particles (greater than 495 μm) within the cirrus anvil. Combining the cloud chamber experiments, previous airborne experiments, and the 3 August 2019 observations, it is reasonable to assume that there is more than one location in which the chain aggregation process is occurring.

The reason why the chain aggregate concentration and the ratio ($RCAC_{N-C}$) decreases from approximately 50 to 20 km from the TITAN cell's core when entering the cirrus anvil produced from the TITAN cell during FL1 remains unknown. Although, it is theorized that the peak in $RCAC_{N-C}$ and the chain aggregate concentration occurs when the aircraft transects through a high concentration 'pocket' of chain aggregates originating from the overshooting-top produced by the TITAN cell. Gayet *et al.* (2012) observed high concentrations of chain aggregates in the overshooting-tops of convection which gives confidence that the 'pocket' of chains may have

originated from the overshooting-top associated with the TITAN cell. The downward reflectivity extent in the CPR-HD radar scan taken during FL1 (Figure 21) also adds confidence that these chain aggregates possibly once resided in the overshooting-top. The CPR-HD radar plots are not a vertical stare; however, it is inferred that the reflectivity is fairly similar directly above and below the aircraft compared to what is depicted in the CPR-HD plots based on the satellite imagery (Figure 6).

Conversely, evidence from the decrease in the non-chain and chain aggregate particle concentrations but the increase in the $RCAC_{N-C}$ further downstream in the cirrus anvil during FL2-4 possibly indicates that either the smaller particles are sublimating and/or the smaller particles are aggregating into larger particles. This provides evidence that chain aggregation may be on-going within the cirrus anvil region. Since the chain aggregates are larger than individual ice crystals, it would be expected that the CPR-HD reflectivity increases with respect to the increase in $RCAC_{N-C}$ for FL4. However, the radar reflectivity factor is dependent on the sixth power of the particles' diameter (D^6) and the number of particles (N_0) per unit volume (American Meteorological Society, 2022). Thus, it is reasonable to assume that the smaller concentrations (N_0) of chain aggregates at the end of FL4 is the reason why the reflectivity (dBZ) is relatively small in the locations where the $RCAC_{N-C}$ is high. Utilizing other radar parameters such as differential reflectivity (ZDR) would add further insight into the interpretation of the radar data, though, no other radar parameters are available for 3 August 2019.

A counter to the theory that chain aggregation is occurring in the cirrus anvil region is the fact that electric field observations do not surpass the electric field threshold (60 kV m^{-1}) as proposed by Saunders and Wahab (1975). However, the electric field threshold in order for chain aggregation to occur may be much less at these colder temperatures (< -30 °C) than previously

proposed based on the similar observations between this analysis, the analysis detailed in Dye and Willet (2007), and Dye and Bansemer (2019). If electric fields do not need to be as high at colder temperatures to aid in the formation of chain aggregates, it is possible that chain aggregation is continuous in the cirrus anvil and is being observed in the $RCAC_{N-C}$ for FL2-4.

CHAPTER VI

CONCLUSION

The North Dakota Citation II Research Aircraft obtained in-situ observations of convection-induced, cirrus anvils on 3 August 2019 near Cape Canaveral, Florida. Four flight legs are available at approximately 10 km AGL where the temperatures are between -29 and -34 °C. The PHIPS probe obtained 4,654 stereographic particle images with 668 (14.4%) are manually classified as chain aggregates. The observed chain aggregates show complex structures and contain individual particle elements from different temperature habits. The chain aggregates occur in varying concentrations (10^{-4}-10^{-2} # cm^{-3}) between 20 and 100 km from the TITAN cell's core reflectivity centroid. The highest concentrations of chain aggregates are nearest to the core (except for FL1) where the concentrations decrease away the core. Only approximately 10% of total amount of chain aggregates observed show some evidence of riming, which partially agrees with in-situ observations gathered by previous field campaigns. Therefore, either: (a) majority of the chain aggregates form in regions with low concentrations of super-cooled liquid water and/or, (b) rimed chains are formed in the mixed-phased region, but majority of them precipitate out of the cloud via downdrafts and do not occur in the cirrus cloud anvil region.

Electric field observations within the cirrus anvil during the 3 August 2019 flight did not reach the theorized 60 kV m^{-1} threshold magnitude in order to form chain aggregates (Saunders and Wahab, 1975). However, the 3 August 2019 electric field observations, and the other field observations from previous airborne campaigns (Dye and Willet, 2007, and Dye and Bansemer, 2019), indicate the electric field magnitudes may not need to be as high at these colder temperature in order to aid in the chain aggregation process within the cirrus anvil. Further lab experiments

testing the aggregation at colder temperatures, using lower electric fields, and with more realistic particle concentrations are needed to add confidence to this hypothesis.

FL1 occurred when the cirrus anvil produced from the TITAN cell is in its mature stage, but the induced cirrus anvil is in its early stage of development. Thus, the lack of observations due to the minimal residence time in the new cirrus anvil for FL1 inhibits conclusions that the chain aggregation process is occurring in the cirrus anvil. However, given the evidence from the in-situ and remote-sensed observations gathered on the latter half of FL1 (during and after the aircraft passes through the boundary between the old and new cirrus anvil [15:56:40 – 16:01:00 UTC]) indicates that a main source of chain aggregation is located above the mixed-phased region in the TITAN cell. The evidence of lightning in the TITAN cell indicates that the electric fields in the thunderstorm more than likely exceeded the necessary electric field threshold to aid in the chain aggregation process. It is theorized that the high concentration of chain aggregates and the high values in the $RCAC_{N-C}$ observed at approximately 53 km from the core (in the new cirrus anvil) originated somewhere within TITAN cell and/or the TITAN cell's overshooting top before precipitating out and intersecting with the aircraft. More in-situ and remote sensed data is needed in the TITAN cell and the overshooting top in order to back up the claim that a main source of chain aggregation is located above the mixed–phased region.

As the storm evolved, the new cirrus anvil produced from the TITAN cell expands allowing the later flight legs to outflow from over shooting tops. During FL2-4, $RCAC_{N-C}$ has a positive slope up to a certain distance from the TITAN cell's core reflectivity centroid while the chain aggregate, non-chain aggregate, and total particle concentrations decrease, which indication chain aggregation is possibly continuing within the cirrus anvil and/or the smaller particles are sublimating away faster than the chain aggregates. The turbulent nature of the reflectivity in the

CPR-HD data for FL4 suggests that mixing between particles is most likely occurring, which aid in the aggregation process (via collisions).

From the in-situ observations and the remote-sensed observations gathered during FL1, it is believed that the most optimal source for chain aggregation to occur is within the convective cell above the mixed phased region where there are high ice particle concentrations, low concentrations of super-cooled liquid water, and high electric field strengths. Regions in a convective cell that may fulfill these requirements are between the main lower-negative and upper-positive charge regions at temperature regions between -15 and -30 °C, and also in the overshooting-top between the upper-positive charge region and the negatively charged screening layer (at temperatures < -35 °C). The distinct lack of riming on the chains with particle elements typically formed in these temperature regimes supports this theory. Moreover, the fact that there are much higher concentrations of chain aggregates closer to the TITAN cell's core for all of the flight legs on 3 August 2019 adds support to this idea. It is likely that chain aggregates that are formed in, around, or just above the mixed phased region may contain rimed ice due to higher concentrations of super-cooled liquid water present. An explanation for why only a small number of rimed chain aggregates were observed (approximately 10% of the total number of chain aggregates) by the PHIPS during the 3 August 2019 flight could be simply due to the aircraft not flying low enough to sample higher concentrations of rimed chain aggregates. Moreover, another possible reason why only few rimed chain aggregates are observed could possibly be due to the low sampling rate of the PHIPS. Physically, the rimed chain aggregates could simply be precipitating out of the cloud (around the perimeter of the updraft) before being lofted higher in the storm. It is possible that the updraft in the TITAN cell did not have sufficient vertical velocities to loft these large, rimed, chains higher up towards the overshooting top before these rimed chain aggregates encounter downdrafts.

Nonetheless, due to the fact that there are no in-situ or remote measurements obtained within the core of the TITAN cell hinders the confidence of this theory that chain aggregates (and rimed chain aggregates) are formed within the convective cell.

In order to further aid in the understanding of where chain aggregation is occurring in thunderstorms, more concurrent microphysical (in-situ) and remote-sensed observations within a convective cell must be obtained at different altitudes. Stacked aircraft sampling at different altitudes with microphysical (imaging and non-imaging) probes and electric field mills within convection-induced, cirrus anvils, as well as within the main convective regions of thunderstorms may further aid in the understanding of the chain aggregation process. Furthermore, it would be ideal to perform this analysis for multiple flights on multiple days. More datasets from convection produced from all types of airmasses would be vital for further interpreting the chain aggregation process. It would be interesting to see if chain aggregates are found in winter storms since nor'easters and lake effect snowstorms are shown to be relatively convective and contain lightning (Williams, 2018).

Main issues that hinder the theory for where chain aggregation is occurring described in this paper is the fact that the Florida thunderstorms sampled were very unorganized. The initial storm was several hours old before the enhanced convection at 15:10:00 UTC allowing for cross-contamination of cloud particles. It would be in the researcher's best interest to avoid this by sampling isolated convection and their induced cirrus anvils in future airborne campaigns.

The work described in this paper only highlights one of the seven flights that made up the CapeEx19 field project in its entirety. It is the goal in the near future to apply this analysis to other flight-days to see if those observations agree with the analysis performed in this paper. In addition

to field experiments, it is the goal to perform experiments in cloud chambers to test the hypothesis that chain aggregation can occur in electric fields < 60 kV m^{-1} at temperatures colder than -30 °C.

REFERENCES

Abdelmonem, A., E. Järvinen, D. Duft, E. Hirst, S. Vogt, T. Leisner, and M. Schnaiter, 2016: PHIPS–HALO: the airborne Particle Habit Imaging and Polar Scattering probe – Part 1: Design and operation. *Atmos. Meas. Tech.*, **9**, 3131–3144, https://doi.org/10.5194/amt-9-3131-2016.

American Meteorological Society, 2022: Radar Reflectivity Factor. Glossary of Meteorology, https://glossary.ametsoc.org/wiki/Radar_reflectivity_factor.

Barnes Jr., A. A., 1982: The Sub-visible Cirrus Background. Air Force Geophysics Laboratory. Date Accessed: 04-15-2021. https://apps.dtic.mil/dtic/tr/fulltext/u2/a117389.pdf.

Bateman, M. G., M. F. Stewart, S. J. Podgorny, H. J. Christian, D. M. Mach, R. J. Blakeslee, J. C. Bailey, and D. Daskar, 2007: A Low-Noise, Microprocessor-Controlled, Internally Digitizing Rotating-Vane Electric Field Mill for Airborne Platforms. *J. Atmos. Oceanic Technol.*, **24**, 1245–1255, https://doi.org/10.1175/JTECH2039.1.

Baumgardner, D., H. Jonsson, W. Dawson, D. O'Connor, and R. Newton, 2001: The cloud, aerosol and precipitation spectrometer: a new instrument for cloud investigations. *Atmospheric Research*, **59–60**, 251–264, https://doi.org/10.1016/S0169-8095(01)00119-3.

Biagi, C. J., K. L. Cummins, K. E. Kehoe, and E. P. Krider, 2007: National Lightning Detection Network (NLDN) performance in southern Arizona, Texas, and Oklahoma in 2003–2004. *Journal of Geophysical Research: Atmospheres*, 112, https://doi.org/10.1029/2006JD007341.

Boccippio, D. J., K. L. Cummins, H. J. Christian, and S. J. Goodman, 2001: Combined Satellite- and Surface-Based Estimation of the Intracloud–Cloud-to-Ground Lightning Ratio over the Continental United States. *Monthly Weather Review*, **129**, 108–122, https://doi.org/10.1175/1520-0493(2001)129<0108:CSASBE>2.0.CO;2.

Christian, H. J., and Coauthors, 2003: Global frequency and distribution of lightning as observed from space by the Optical Transient Detector. *Journal of Geophysical Research: Atmospheres*, 108, ACL 4-1-ACL 4-15, https://doi.org/10.1029/2002JD002347.

Connolly, P. J., C. P. R. Saunders, M. W. Gallagher, K. N. Bower, M. J. Flynn, T. W. Choularton, J. Whiteway, and R. P. Lawson, 2005: Aircraft Observations of the Influence of Electric Fields on the Aggregation of Ice Crystals. *Quarterly Journal of the Royal Meteorological Society*, **131**, 1695–1712, https://doi.org/10.1256/qj.03.217.

Crowther, A. G. and C. P. R. Saunders, 1973: On the Aggregation and Fragmentation of Freely-Falling Ice Crystals in an Electric Field. *J. Met. Soc. Japan*, **51**, 490-493.

Cummins, K. L., M. J. Murphy, E. A. Bardo, W. L. Hiscox, R. B. Pyle, and A. E. Pifer, 1998: A Combined TOA/MDF Technology Upgrade of the U.S. National Lightning Detection Network. *Journal of Geophysical Research: Atmospheres*, **103**, 9035–9044, https://doi.org/10.1029/98JD00153.

Delene, D. J., 2011: Airborne Data Processing and Analysis Software Package, *Earth Science Informatics*, **4(1)**, 29-44, http://dx.doi.org/10.1007/s12145-010-0061-4, DOI: 10.1007/s12145-010-0061-4.

Delene, D. J., K. Hibert, M. Poellot, and N. Bracklin, 2019: The North Dakota Citation Research Aircraft Measurement Platform. 2019 SAE International Conference on Icing of Aircraft, Engines, and Structures.

Dye, J. E., and A. Bansemer, 2019: Electrification in Mesoscale Updrafts of Deep Stratiform and Anvil Clouds in Florida. *Journal of Geophysical Research: Atmospheres*, **124**, 1021–1049, https://doi.org/10.1029/2018JD029130.

Dye, J. E., and Coauthors, 2007: Electric fields, cloud microphysics, and reflectivity in anvils of Florida thunderstorms. *Journal of Geophysical Research: Atmospheres*, 112, https://doi.org/10.1029/2006JD007550.

Dye, J. E., and J. C. Willett, 2007: Observed Enhancement of Reflectivity and the Electric Field in Long-Lived Florida Anvils. *Monthly Weather Review*, **135**, 3362–3380, https://doi.org/10.1175/MWR3484.1.

Gapp, N. J., 2019: Comparison of Concurrent Radar and Aircraft Measurements in Cirrus Clouds. M.S. thesis, Dept. of Atmospheric Sciences, University of North Dakota, 54 pp.

Garrett, T. J., and Coauthors, 2005: Evolution of a Florida Cirrus Anvil. *Journal of the Atmospheric Sciences*, **62**, 2352–2372, https://doi.org/10.1175/JAS3495.1.

Gayet, J.-F., and Coauthors, 2012: On the observation of unusual high concentration of small chain-like aggregate ice crystals and large ice water contents near the top of a deep convective cloud during the CIRCLE-2 experiment. *Atmospheric Chemistry and Physics*, **12**, 727–744, https://doi.org/10.5194/acp-12-727-2012.

Jensen, E., D. Starr, and O. B. Toon, 2004: Mission investigates tropical cirrus clouds. Eos, *Transactions American Geophysical Union*, **85**, 45–50, https://doi.org/10.1029/2004EO050002.

Korolev, A. V., J. W. Strapp, G. A. Isaac, and A. N. Nevzorov, 1998: The Nevzorov Airborne Hot-Wire LWC–TWC Probe: Principle of Operation and Performance Characteristics. *Journal of Atmospheric and Oceanic Technology*, **15**, 1495–1510, https://doi.org/10.1175/1520-0426(1998)015<1495:TNAHWL>2.0.CO;2.

Latham, J., 1969: Experimental studies of the effect of electric fields on the growth of cloud particles. *Quarterly Journal of the Royal Meteorological Society*, **95**, 349– 361, https://doi.org/10.1002/qj.49709540408.

Latham, J., and C. P.R. Saunders, 1964: Aggregation of Ice Crystals in Strong Electric Fields, *Nature*, **204**, 1293 – 1294.

Latham, J., and C. P. R. Saunders, 1970: Experimental measurements of the collection efficiencies of ice crystals in electric fields. *Quarterly Journal of the Royal Meteorological Society*, **96**, 257–265, https://doi.org/10.1002/qj.49709640808.

Lawson, R. P., B. A. Baker, and B. L. Pilson, 2003: In Situ Measurements of Microphysical Properties of Mid-latitude and Anvil Cirrus. Date Accessed: 04-25-2021. http://www.specinc.com/sites/default/files/pdfs/Cirrus_Anvil_paper_Rev2_.pdf

Lin, T. C., and N. A. Thyson, 1977: Ice-crystal/shock-layer interaction in hypersonic flight. *AIAA Journal*, **15**, 1511–1514, https://doi.org/10.2514/3.7446.

Liou, K. N., 1973: Transfer of Solar Irradiance through Cirrus Cloud Layers., *J. Geophys. Res.*, **78**, 1409–1418.

LROSE, 2021: LROSE – Lidar Radar Open Software Environment. Accessed 10 June 2020, https://www.lrose.net.

Mach, D. M., and W. J. Koshak, 2007: General Matrix Inversion Technique for the Calibration of Electric Field Sensor Arrays on Aircraft Platforms. *Journal of Atmospheric and Oceanic Technology*, **24**, 1576–1587, https://doi.org/10.1175/JTECH2080.1.

Mailyan, B. G., and Coauthors, 2018: Characteristics of Radio Emissions Associated With Terrestrial Gamma-Ray Flashes. *J. Geophys. Res. Space Physics*, **123**, 5933–5948, https://doi.org/10.1029/2018JA025450.

Matsui, T., J.-D. Chern, W.-K. Tao, S. Lang, M. Satoh, T. Hashino, and T. Kubota, 2016: On the Land–Ocean Contrast of Tropical Convection and Microphysics Statistics Derived from TRMM Satellite Signals and Global Storm-Resolving Models. *Journal of Hydrometeorology*, **17**, 1425–1445, https://doi.org/10.1175/JHM-D-15-0111.1.

Meng, H.C. and K.C. Ludema, 1995: Wear models and predictive equations: their form and content, *WEAR*, **181-183**, 443-457.

NCAR, 2021a: MDV Format Interface Control Document (ICD). Accessed 10 June 2020, https://www.github.com/NCAR/lrose-titan/blob/master/docsa/pdf/MDV_format_ICD.pdf.

NCAR, 2021b: TITAN. Accessed 10 June 2020, https://www.github.com/NCAR/lrose-titan.

O'Shea, S. J., J. Crosier, J. Dorsey, W. Schledewitz, I. Crawford, S. Borrmann, R. Cotton, and A. Bansemer, 2019: Revisiting particle sizing using grayscale optical array probes evaluation using laboratory experiments and synthetic data. *Atmos. Meas. Tech. Discuss.*, 1–29, https://doi.org/10.5194/amt-2018-435.

Probstein, R. F.; Fassio, F. Dusty Hypersonic Flows. *AIAA J.* **1970**, *8* (4), 772–779. https://doi.org/10.2514/3.5755.

Rakov, V. A., 2016, General picture, *Fundamentals of Lightning*, Cambridge University Press, 52-65.

Saunders, C. P. R., and N. M. A. Wahab, 1975: The Influence of Electric Fields on the Aggregation of Ice Crystals. *Journal of the Meteorological Society of Japan*, **53**, 121–126, https://doi.org/10.2151/jmsj1965.53.2_121

Schmidt, J. M., and Coauthors, 2019: Radar Detection of Individual Raindrops. *Bulletin of the American Meteorological Society*, **100**, 2433–2450, https://doi.org/10.1175/BAMS-D-18-0130.1.

Schnaiter, M., E. Järvinen, A. Abdelmonem, and T. Leisner, 2018: PHIPS-HALO: the airborne particle habit imaging and polar scattering probe – Part 2: Characterization and first results. *Atmos. Meas. Tech.*, **11**, 341–357, https://doi.org/10.5194/amt-11-341-2018.

Skofronick-Jackson, G., and Coauthors, 2015: Global Precipitation Measurement Cold Season Precipitation Experiment (GCPEX): For Measurement's Sake, Let It Snow. *Bulletin of the American Meteorological Society*, **96**, 1719–1741, https://doi.org/10.1175/BAMS-D-13-00262.1.

Smith, P. L., D. J. Musil, A. G. Detwiler, and R. Ramachandran, 1999: Observations of Mixed-Phase Precipitation within a CaPE Thunderstorm. *Journal of Applied Meteorology and Climatology*, **38**, 145–155, https://doi.org/10.1175/1520-0450(1999)038<0145:OOMPPW>2.0.CO;2.

Stith, J. L., J. E. Dye, A. Bansemer, A. J. Heymsfield, C. A. Grainger, W. A. Petersen, and R. Cifelli, 2002: Microphysical Observations of Tropical Clouds. *J. Appl. Meteor.*, **41**, 97–117, https://doi.org/10.1175/1520-0450(2002)041<0097:MOOTC>2.0.CO;2.

Stith, J. L., J. A. Haggerty, A. Heymsfield, and C. A. Grainger, 2004: Microphysical Characteristics of Tropical Updrafts in Clean Conditions. *Journal of Applied Meteorology and Climatology*, **43**, 779–794, https://doi.org/10.1175/2104.1.

Stith, J. L., and Coauthors, 2014: Ice particles in the upper anvil regions of midlatitude continental thunderstorms: the case for frozen-drop aggregates. *Atmos. Chem. Phys.*, **14**, 1973–1985, https://doi.org/10.5194/acp-14-1973-2014.

Thomas, R. J., 2004: Accuracy of the Lightning Mapping Array. *J. Geophys. Res.*, **109**, D14207, https://doi.org/10.1029/2004JD004549.

Um, J., and Coauthors, 2018: Microphysical characteristics of frozen droplet aggregates from deep convective clouds. *Atmospheric Chemistry and Physics*, **18**, 16915–16930, https://doi.org/10.5194/acp-18-16915-2018.

Waldman, G. D.; Reinecke, W. G. Particle Trajectories, Heating, and Breakup in Hypersonic Shock Layers. *AIAA J.* **1971**, *9* (6), 1040–1048. https://doi.org/10.2514/3.6328.

Whiteway, J., and Coauthors, 2004: Anatomy of cirrus clouds: Results from the Emerald airborne campaigns. *Geophysical Research Letters*, **31**, https://doi.org/10.1029/2004GL021201.

Williams, E., 2018: Lightning Activity in Winter Storms: A Meteorological and Cloud Microphysical Perspective, *IEEJ Transactions on Power and Energy*, **138**, 5, 363 – 373, https://doi.org/10.1541/ieejpes.138.364.

APPENDIX A: CHAIN AGGREGATES AND SUPERSONIC FLIGHT

When hypersonic vehicles traverse a cloud in the Earth's atmospheric (mainly during re-entry), the vehicles will encounter raindrops and/or ice crystals. Due to the high-speed nature of these vehicles, cloud particles may cause serious damage to the heatshield (nose cone). The problem regarding the likelihood of ice crystal interactions with hypersonic vehicles during flight is illustrated in Figure 27. This problem has been known since at least the late 1970's where Lin and Thyson (1977) investigated the dynamics of ice crystals in the shock layer. There has been a focus into the sub-visible cirrus, dust, and aerosol interactions with hypersonic nose cones (Probstein and Fassio 1970; Waldman and Reineche 1971; Barnes 1982), though, there is a lack of current research regarding large ice crystal aggregates (such as chain-like aggregates) and their interaction with hypersonic nose cones. It is reasonable to assume that these chain aggregates may have a larger effect on the nosecone erosion due to chain aggregates having larger mass then individual ice particles.

As a quick assessment to see how impactful chain aggregates might be to a hypersonic vehicle nose cone we can assume a circular intercontinental ballistic missile (ICBM) nose cone has a diameter of 3 m and an area of approximately 7 m^2 and traverses through a 5 km thick cirrus cloud; where in the region where the ICBM transverses through contains 10,000 chain aggregates per m^3. This gives an estimate of 350,000,000 possible impacts with chain aggregates.

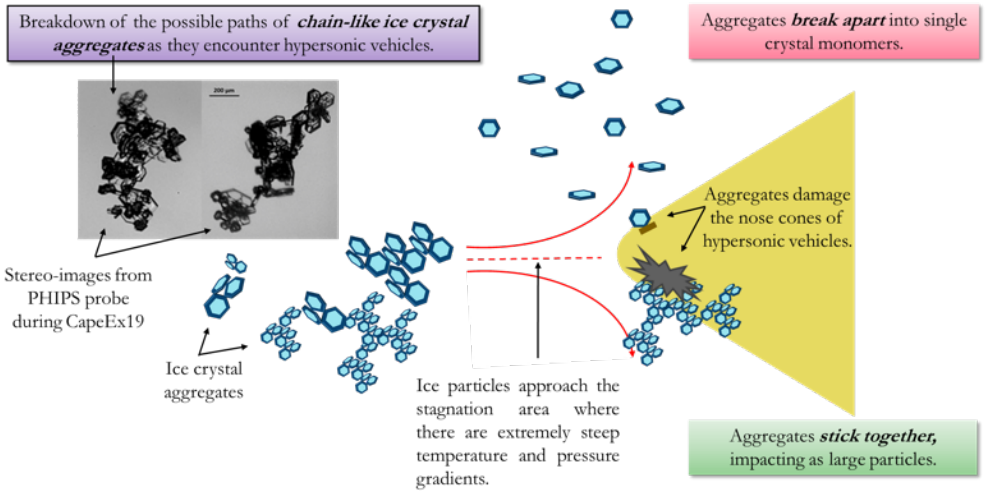

Figure 27. Illustration of ice aggregates impacting a vehicles nose cone. The ice aggregates' damage potential to hypersonic vehicles can be significantly different if they break apart into individual ice crystals or stay together across the harsh thermochemical changes through a shock wave. This image is obtained from Hallie Chelmo from the University of North Dakota's Mechanical Engineering Department.

APPENDIX B: PARTICLE CLASSIFICATION

The PHIPS particle classification software contains a graphical user interface (GUI) written in MATLAB and is depicted in Figure 3 and was developed by scientists (Emma Järvinen and Fritz Waitz) at the Karlsruhe Institute of Technology (KIT). The classification GUI allows for manual classification of particles that were specifically imaged by the PHIPS probe. All that is needed for the software to operate are two folders; one containing the camera 1 (C1) PHIPS particle images and the other containing the camera 2 (C2) PHIPS particle images. The C1 and C2 PHIPS images can be read and displayed in the two image windows. Multiple particle attributes and particle habits can then be selected by the classifier. A confidence level selector is also depicted at the bottom-middle of Figure 3. This confidence selector is used in defining the chain aggregates described in this paper.

Manually classifying a large dataset of particle images can take extended periods of time. This classification GUI allows the user to save and then reload the dataset wherever the user left off. The output file produced from this software is in a comma-separated values (CSV) file format. This software is available upon request.

APPENDIX C: IMAGED CHAIN AGGREGATES DURING FL1-4

Some of the chain aggregates observed during the flight legs by the PHIPS (with an attributed particle diameter measurement; Figure 28).

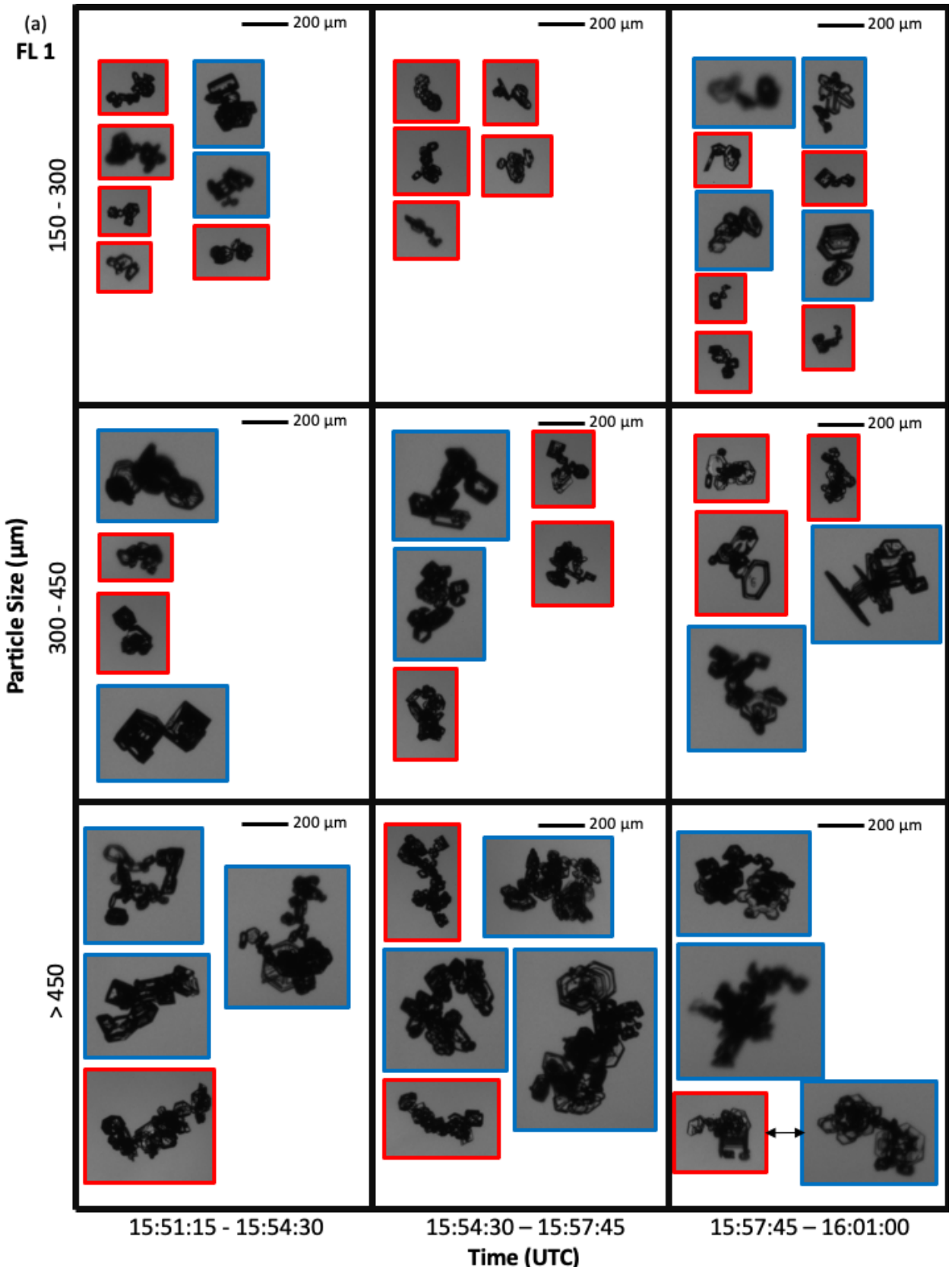
(a)
FL 1
200 µm
150 - 300
300 - 450
> 450
Particle Size (µm)
15:51:15 - 15:54:30
15:54:30 – 15:57:45
15:57:45 – 16:01:00
Time (UTC)

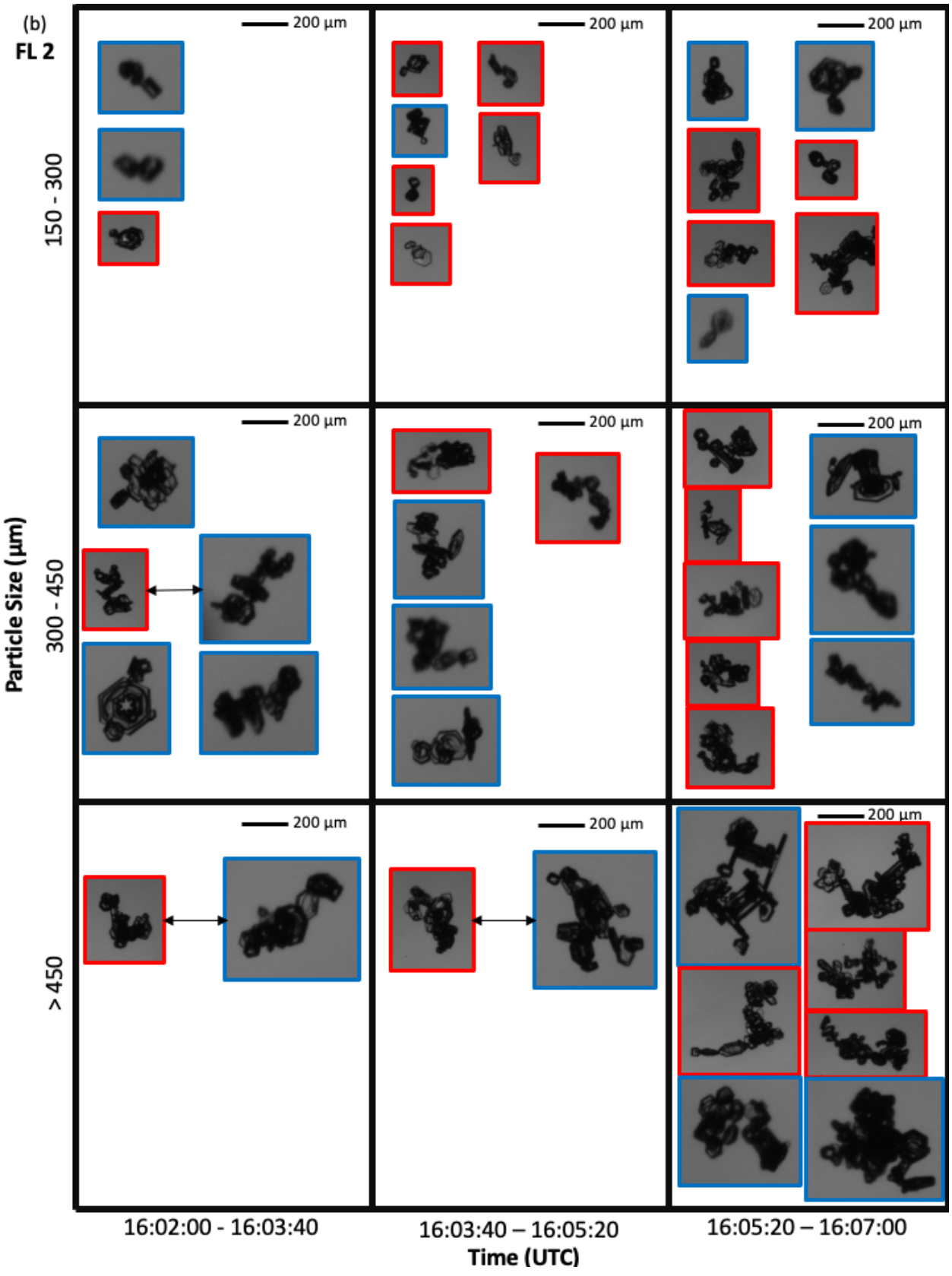
(b)
FL 2
200 µm
150 - 300
300 - 450
> 450
Particle Size (µm)
16:02:00 - 16:03:40
16:03:40 – 16:05:20
16:05:20 – 16:07:00
Time (UTC)

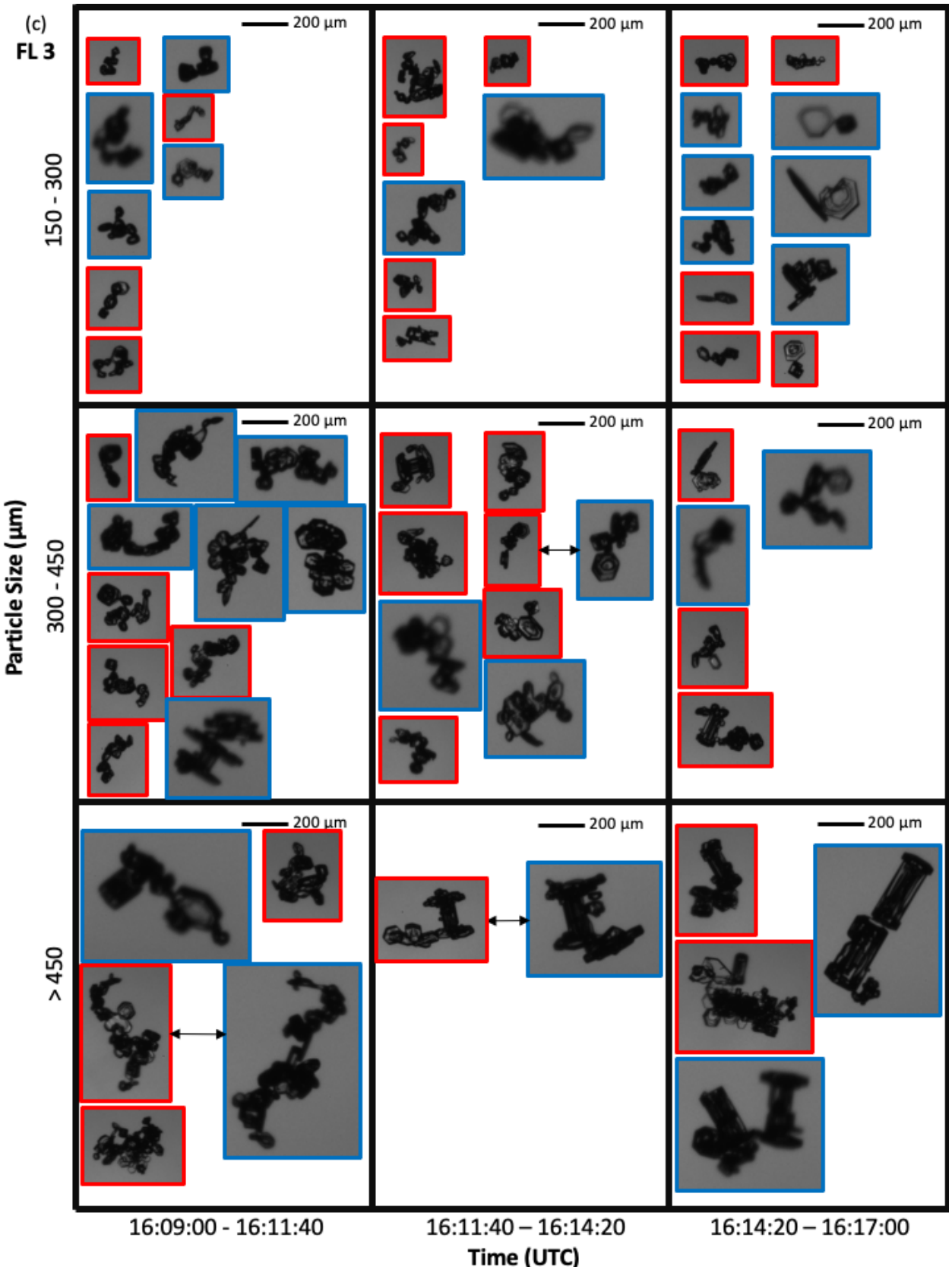
(c)
FL 3
Particle Size (µm)
150 - 300
300 - 450
> 450
200 µm
16:09:00 - 16:11:40
16:11:40 – 16:14:20
16:14:20 – 16:17:00
Time (UTC)

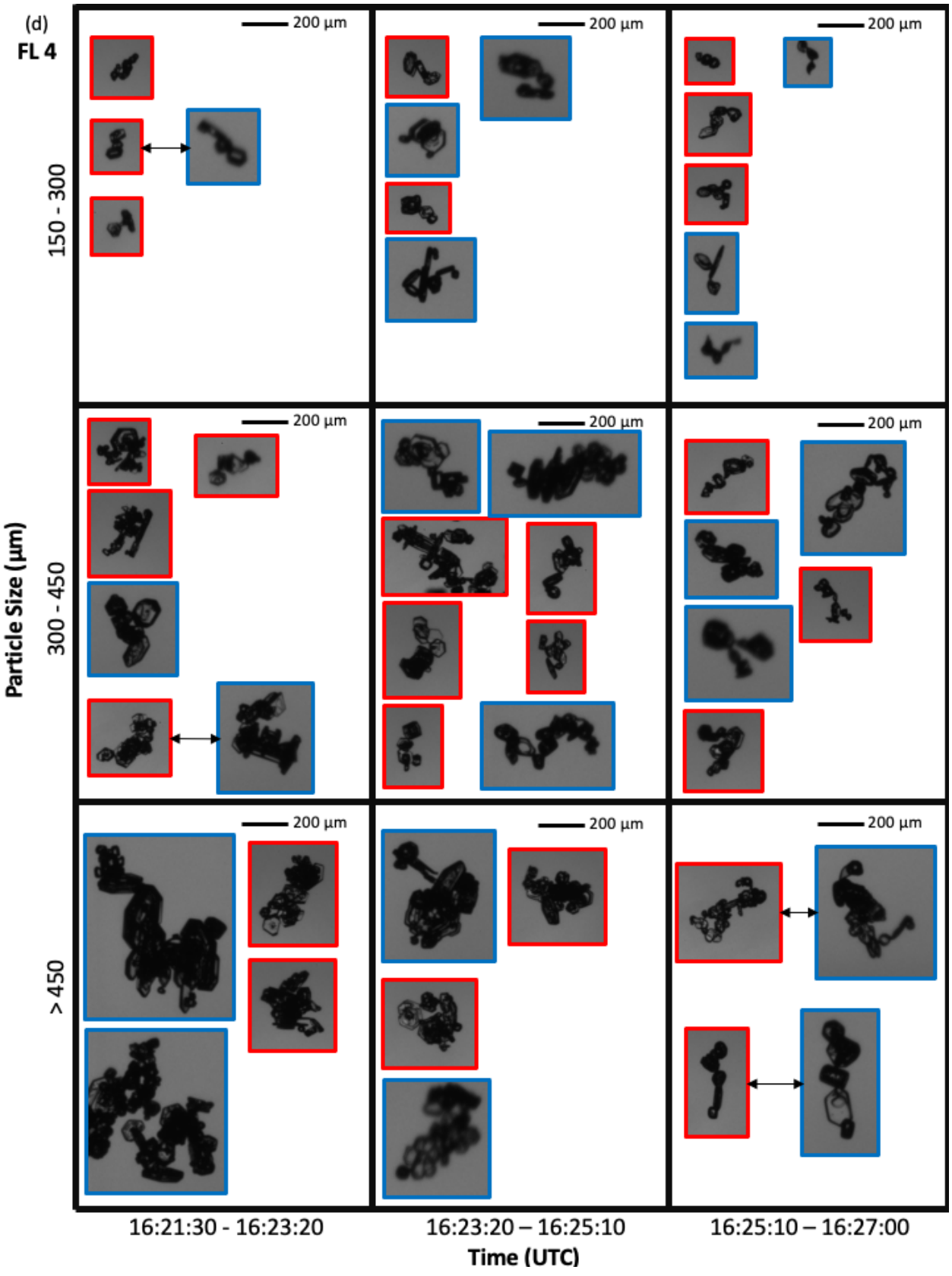
(d)
FL 4
200 µm
150 - 300
300 - 450
> 450
Particle Size (µm)
16:21:30 - 16:23:20
16:23:20 – 16:25:10
16:25:10 – 16:27:00
Time (UTC)

Figure 28. Particle Habit Imaging and Polar Scattering (PHIPS) probe images taken during the CapeEx19 field campaign on 3 August 2019. Images with a red and blue outline correspond to the PHIPS camera – 1 (C1) and camera – 2 (C2) respectively. The black arrows connecting two images represents the same imaged particle from two view angles, 120 degrees apart. The chain aggregates shown in (a) – (d) vary between confidence 1 – 3.

APPENDIX D: KMLB RADAR LIMITATIONS

It was the goal to utilize the LROSE-TITAN software capabilities to display cross-sections of the TITAN cell and its produced cirrus anvil during the flight legs. This would provide a vertical profile of the convective cell and its induced cirrus anvil where the aircraft sampled. However, several limitations of the KMLB radar make it difficult to correlate the in – situ microphysical observations to the radar data.

A main issue with correlating the in-situ microphysical observations to the radar data is the fact that the KMLB radar volume scans take approximately 5 minutes to complete one full cycle. Since the duration of flight legs are between 5 and 11 minutes long, only 1 or 2 KMLB radar volume scans can be utilized for the comparison per flight leg. The KMLB radar data is a 'snapshot' of a 5-minute time frame where the in-situ aircraft data is continuous. Moreover, the cirrus anvil is constantly evolving within the 5-minute volume scan and the KMLB radar cannot observe or measure this small-scale cloud evolution. Thus, the difference in temporal resolution from the KMLB radar and the aircraft observations makes it extremely difficult for comparisons between the two.

In addition to the inadequate temporal resolution of the KMLB radar, the radar also has inadequate spatial resolution that decreases with distance from the radar site. This is observed while creating cross-sections of the storm where the aircraft sampled (Figure 29). The KMLB could not register the cloud particles when the aircraft was approximately between 90 and 120 km from the radar's location sampling at 10 km AGL. Evidence from the aircraft TWC data (Figure 10) from the aircraft show we were in cloud at 15:51:15 UTC (roughly 115 km north northwest KMLB).

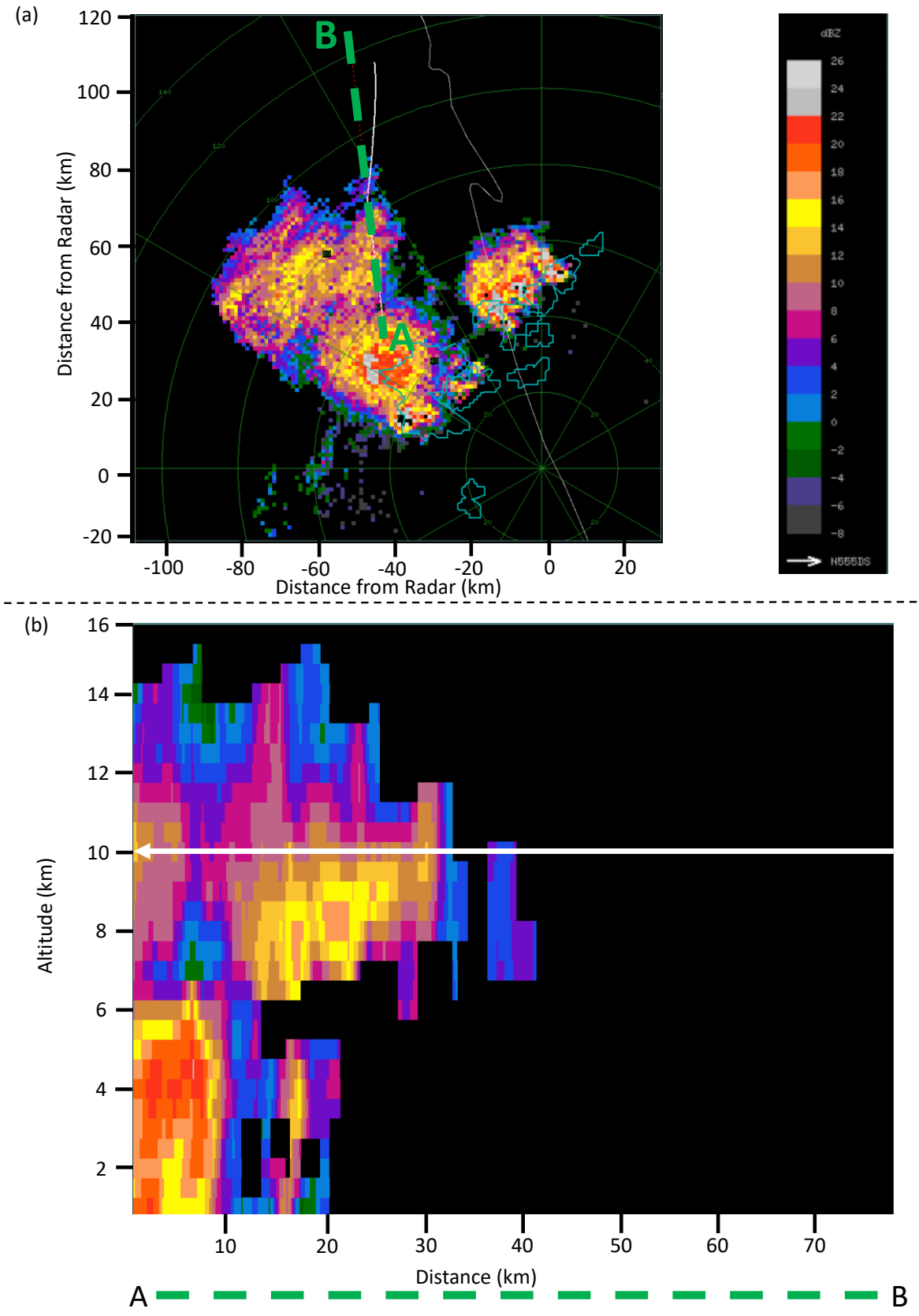
(a)
B
A
Distance from Radar (km)
Distance from Radar (km)
120
100
80
60
40
20
0
-20
-100
-80
-60
-40
-20
0
20
dBZ
26
24
22
20
18
16
14
12
10
8
6
4
2
0
-2
-4
-6
-8
N556DS
(b)
Altitude (km)
16
14
12
10
8
6
4
2
10
20
30
40
50
60
70
Distance (km)
A
B

Figure 29. Plot where panel (a) shows a plan-view radar reflectivity (dBZ) 10 km CAPPI from the KMLB radar volume scan that ended at 16:02:01 UTC. The overlaid thin blue lines indicate the various convective storm cores (utilizing a threshold of 35 dBZ) using TITAN cell tracking. The overlaid thin white (solid) line indicates the flight track for FL1 (between 15:51:15 and 16:01:00 UTC). The green (dotted) line indicates where the cross-section is performed (from A to B). Panel (b) shows the cross-section as indicated in panel (a). The white (solid) line indicates the flight altitude and direction.